# Interannual variability in the Australian carbon cycle over 2015-2019, based on assimilation of OCO-2 satellite data

Yohanna Villalobos[1,2,5], Peter J. Rayner[1,2,3], Jeremy D. Silver[1,4], Steven Thomas[1], Vanessa Haverd[5,†], Jürgen Knauer[9,5], Zoë M. Loh[6], Nicholas M. Deutscher[7], David W.T. Griffith[7], and David F. Pollard[8]

[1]School of Geography, Earth and Atmospheric Sciences, University of Melbourne, Australia
[2]ARC Centre of Excellence for Climate Extremes, Sydney, Australia
[3]Climate & Energy College, University of Melbourne, Melbourne, Australia
[4]School of Mathematics and Statistics, University of Melbourne, Melbourne, Australia
[5]CSIRO Oceans and Atmosphere, Canberra, 2601, Australia
[6]CSIRO Oceans and Atmosphere, Aspendale, Victoria 3195, Australia
[7]Centre for Atmospheric Chemistry, School of Chemistry, University of Wollongong, Wollongong, NSW, 2522, Australia.
[8]National Institute of Water and Atmospheric Research Ltd (NIWA), Lauder, New Zealand.
[9]Hawkesbury Institute for the Environment, Western Sydney University, Penrith, NSW 2751, Australia
[†]Deceased, 19 January 2021.

**Correspondence:** Yohanna Villalobos (yohanna.villaloboscortes@csiro.au)

**Abstract.**

In this study, we employ a regional inverse modelling approach to estimate monthly carbon fluxes over the Australian continent for 2015–2019 using the assimilation of the total column-averaged mole fractions of carbon dioxide from the Orbiting Carbon Observatory-2 (OCO-2, version 9). Subsequently, we study the carbon cycle variations and relate their fluctuations to anomalies in vegetation productivity and climate drivers. Our five-year regional carbon flux inversion suggests that Australia was a carbon sink averaging -0.46 $\pm$ 0.08 PgC yr$^{-1}$ (excluding fossil fuel emissions), largely influenced by a strong carbon uptake (-1.04 PgC yr$^{-1}$) recorded in 2016. Australia's semi-arid ecosystems, such as sparsely vegetated regions (in central Australia) and savanna (in northern Australia), were the main contributors to the carbon uptake in 2016. These regions showed relatively high vegetation productivity, high rainfall and low temperature in 2016. In contrast to the large carbon sink found in 2016, the large carbon outgassing recorded in 2019 coincides with an unprecedented deficit of rainfall and higher than average temperature across Australia. Comparison of the posterior column average $CO_2$ concentration against the Total Carbon Column Observing Networks (TCCON) and in situ measurements offers limited insight into the fluxes assimilated with OCO-2. However, the lack of these monitoring stations across Australia, mainly over ecosystems such as the savanna and areas with sparse vegetation, impedes us from providing strong conclusions. To a certain extent, we found that the flux anomalies across Australia are consistent with the ensemble mean of the OCO-2 Multi-model Intercomparison Project (MIP) and FLUXCOM (2015-2018), which also estimates an anomalous carbon sink for Australia in 2016 of -1.09 and -0.42 PgC yr$^{-1}$ respectively. More accurate estimates of OCO-2 retrievals, with the addition of ocean glint data into our system, and a better understanding of the error in the atmospheric transport modelling will yield further insights into the difference in magnitude of our carbon flux estimates.

# 1 Introduction

On average, each year, the global terrestrial biosphere absorbs about one-quarter of total global fossil-fuel $CO_2$ emissions that human activities add to the atmosphere (Friedlingstein et al., 2020). Carbon uptake by the terrestrial biosphere plays an important role in the Earth's carbon cycle and in future climate projections, since they can slow down the rise in atmospheric $CO_2$ concentrations. Due to uncertainties in quantifying carbon fluxes by terrestrial biosphere models (Sitch et al., 2013, 2015), scientists are unsure whether the growth rate of emissions in the atmosphere is going to increase or decrease in the future. In particular the contributions of semi-arid regional ecosystems such as Australia are uncertain and subject to high variability (Trudinger et al., 2016). Understanding which are the main drivers behind carbon flux variability in semi-arid ecosystems is crucial not only for understanding the global carbon cycle but also for predicting future trends in atmospheric $CO_2$ concentration and consequently the future of climate change.

Australia's contribution to inter-annual global carbon cycle variability has been a topic of interest to the carbon-cycle research community due to an unusually large land carbon sink anomaly of about -0.70 PgC yr$^{-1}$ (relative to the 2003–2012) recorded in 2011, which alone accounted for 57% of the global terrestrial carbon uptake anomaly in this period. Poulter et al. (2014) suggests that the reason for this large carbon uptake in Australia was due to an increase of vegetation cover as a result of increased precipitation in 2011, one of the wettest years on record for Australia. Another study performed by Trudinger et al. (2016) found similar results to Poulter et al. (2014); they estimated a carbon uptake anomaly of -0.40 to -0.61 PgC yr$^{-1}$ (relative to the 1982–2013). Global atmospheric inversions based on atmospheric $CO_2$ concentrations also support this unexpected large sink over Australia. A study carried out by Detmers et al. (2015) based on the assimilation of the Greenhouse Gases Observing Satellite (GOSAT) retrievals found that the carbon sink anomaly in Australia in 2011 was about -0.23 PgC yr$^{-1}$ (relative to the period June 2009–June 2013). All these studies agree that the main driver behind the carbon sink anomaly in 2011 was an increase in the gross primary productivity (GPP) arising from an increase in rainfall which coincides with La Niña event that occurred from 2010 to 2011. Haverd et al. (2016) suggested that the carbon sink anomaly recorded in 2011 was 90% attributable to a higher than expected carbon uptake by semi-arid ecosystems such as savanna and sparsely vegetated regions, mostly driven by a positive response of these ecoregions to precipitation anomalies.

Ma et al. (2016) suggested that the size of the 2011 carbon sink anomaly in Australia was abruptly reduced in 2012, and was nearly eliminated in 2013 (0.08 PgC yr$^{-1}$) due to a decrease in rainfall across Australia. In this study, the authors show that Australia's semi-arid ecosystems' productivity is strongly influenced by drivers such as rainfall and temperature. A recent continental-scale inverse modelling study, utilising OCO-2 satellite data, suggests that Australia was a sink of $CO_2$ of -0.41 $\pm$ 0.08 PgC yr$^{-1}$ for 2015 (Villalobos et al., 2021). In this study, the authors indicate that the stronger carbon sink estimated in 2015 was primarily driven by an increase in productivity over the savanna and sparsely vegetated regions. In this study, the authors also mentioned that periods with a stronger carbon uptake were likely related to increased rainfall in Australian semi-arid ecosystems.

The current study builds upon the work of Villalobos et al. (2021), which only performed an inversion for 2015 and focused on the total mean of carbon flux for that period. In this study, we assimilate the total column average retrieval from NASA's

Orbiting Carbon Observatory$-2$ (OCO-2) to study the interannual variability of the Australia carbon fluxes for the period 2015–2019. An interesting question is whether the large carbon sink estimated in 2015 over semi-arid ecosystems will follow the same patterns after this year or whether such patterns will become stronger or weaker due to changes in precipitation and temperature. Our paper is organized as follows: Sect. 2 describes the methodology and data we used to perform the inversion, which also includes a description of the climate drivers and auxiliary data. Section. 3 presents the results of our five-year inversion, which includes the analysis of the inversion performance and the study of the prior and posterior Australian carbon fluxes, along with an assessment of the GPP carbon flux estimate derived from the CABLE model. In this section, we also assess the robustness of the inversion (against independent data) and provide the analysis of inter-annual variability of rainfall, temperature and the Enhanced Vegetation Index (EVI) over semi-arid ecosystems across Australia. Section. 4 discusses how well our assimilated OCO-2 carbon fluxes align with other global products: MIP OCO-2 global inversions and FLUXCOM, and give some directions for future work. Finally, in Sect. 3, we summarize the results of this study.

## 2  Method and data

We follow the same four-dimensional variational data assimilation approach used to estimate the Australia carbon fluxes described in Villalobos et al. (2021). In this section we will give a brief description of the system and the data used in the inversion. Further details can be found in Villalobos et al. (2020, 2021).

### 2.1  Inversion set-up

Our regional inversion system optimizes monthly-mean gridded-based surface carbon emissions $x$ using a four-dimensional variational data assimilation method, which was configured to use the Community Multi-scale Air Quality Model (CMAQ) (version, v5.3) and its adjoint (version 4.5.1; Hakami et al., 2007). Each year of the five-year period was run independently, with a spin-up of one month for each year. Our system optimizes $CO_2$ surface fluxes by finding the minimum of the cost function $J(x)$ shown in Eq. 1. Notation in this study follows Rayner et al. (2019).

$$J(x) = \frac{1}{2} \left[ (x - x^b)^T \mathbf{B}^{-1} (x - x^b) \right] + \frac{1}{2} \left[ (\mathbf{H}(x) - y)^T \mathbf{R}^{-1} (\mathbf{H}(x) - y) \right] \tag{1}$$

This cost function measures the mismatch between the CMAQ forward model simulation $\mathbf{H}$ and OCO-2 satellite observations $y$ and the deviation of the control vector $x$ from its background (also termed prior) estimate $x^b$. In our case, the control vector $x$ (vector of unknowns) consists not only of the gridded $CO_2$ surface fluxes, but also incorporates initial and boundary conditions (BCs). These two latter variables were incorporated into the control vector to reduce any potential biases related to the boundary inflow that could affect our system (detail of how we treat the boundary and initial conditions in our system can be found in Sect. 2.2 in Villalobos et al., 2020, 2021), and brief description of this treatment is found in Section 2.2. $\mathbf{R}$ represents the observational error covariance matrix, which was defined as a diagonal matrix (full description of this covariance matrix is found in Sect.2.3 in Villalobos et al., 2020) and a brief explanation of how was constructed is found in Sect. 2.4. $\mathbf{B}$

is the associated error covariance matrix of $\boldsymbol{x_b}$, boundary and initial concentrations, and includes off-diagonal terms. In these off-diagonal values, we only include spatial and non-temporal correlations of the prior fluxes (details of the structure of the prior error covariance matrix is found in Section 2.4 in Villalobos et al., 2020), and summary of its description is found in Sect 2.3.

The minimization procedure involves iterative calculations of $J(\boldsymbol{x})$ and its gradient $\nabla_{\mathbf{x}}J(\mathbf{x})$, using the CMAQ forward model $\mathbf{H}$ and its adjoint $\mathbf{H^T}$, as is shown in Eq. 2.

$$\nabla_x J = \mathbf{B}^{-1}(\boldsymbol{x} - \boldsymbol{x}^b) + \mathbf{H}^T(\mathbf{R}^{-1}\left[\mathbf{H}(\boldsymbol{x}) - \boldsymbol{y})\right]) \tag{2}$$

The algorithm that our inversion system uses to minimize the $J(\boldsymbol{x})$ is the Limited-Memory Broyden-Fletcher-Goldfarb-Shanno (L-BFGS-B) (Byrd et al., 1995), implemented in the `scipy` python module. The L-BFGS-B algorithm iteratively adjusts $\boldsymbol{x}$ until $J(\boldsymbol{x})$ reaches a minimum. We reached a reasonable convergence for each year run after iteration 25. The ratio between the cost function and the number of observations was close to the theoretical expected value (see details Sect. 3.1). Posterior uncertainties in this study were assumed to be the same as Villalobos et al. (2020, Sect. 2.4). However, we increase their value by a factor of 1.2 to satisfy the theoretical assumption in the variational optimization (p.211, Tarantola, 1987).

## 2.2 Initial and boundary conditions

To avoid the effect of initial conditions (ICs) and boundary conditions (BCs) on our OCO-2 assimilated carbon fluxes, we optimized them within the control vector $\boldsymbol{x}$. Each lateral boundary (south, east, north, and west) of our regional WRF-CMAQ domain was split into two regions. Lateral BCs at lower layer of the atmosphere were taken from $\sigma = 1$ to $\sigma = 0.96$, which correspond (on average) to a pressure of 972.5 hPa, while the upper boundary layer were solved from 972.5 up to 50 hPa. Each lateral BCs was solved at a monthly scale. Boundary and initial concentration were taken from CAMS global $CO_2$ atmospheric inversion product data (version v19r1) (Chevallier, 2019). BCs uncertainties were assumed as the standard deviation ($1\sigma$ uncertainty) in the perimeter of each region of the boundaries, and uncertainties for the initial condition were set at 1% (approximately 4 ppm). An diagram of the WRF-CMAQ domain is illustrated in Fig. 1.
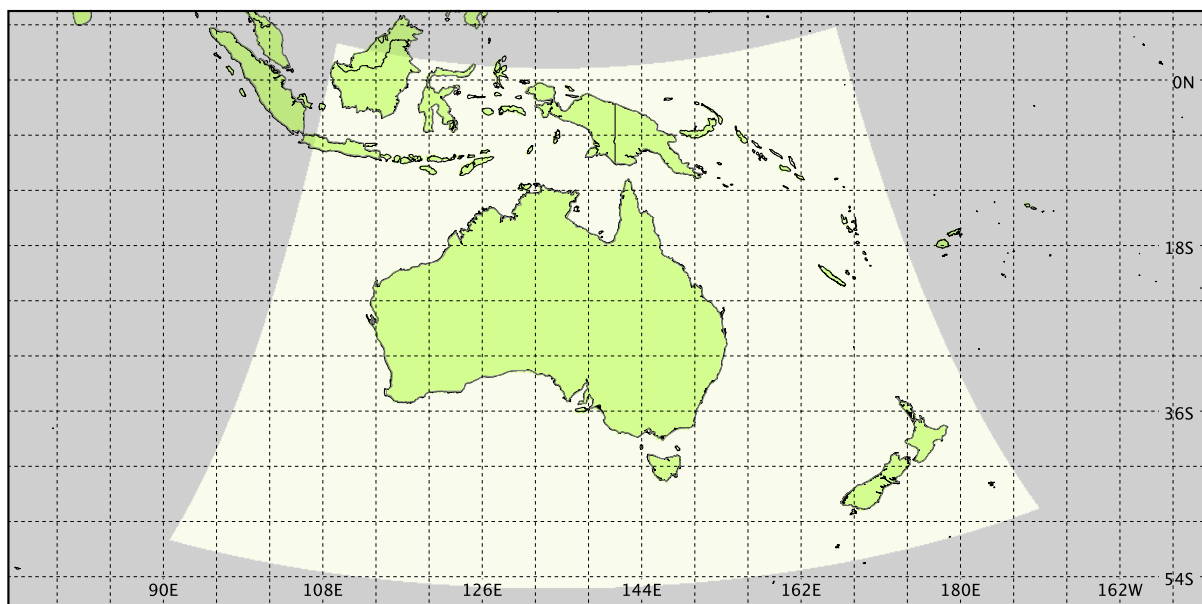
**Figure 1.** Horizontal WRF-CMAQ modelling domain (shown in lighter colours) based on the Lambert conformal projection.

## 2.3 Transport model and prior fluxes

The CMAQ model was used to simulate atmospheric transport and dispersion. These simulations, which were run off-line from the meteorological model, were conducted without atmospheric chemistry. The meteorological data used as input for the CMAQ model were taken from the Weather Research and Forecasting (WRF) model (version V4.1.1) (Skamarock et al., 2008). We run the CMAQ model at hourly resolution at a grid-cell scale of 81 km. The model has 32 vertical levels using the terrain-following $\sigma$ vertical coordinate system. Details of the parameterizations are listed in Villalobos et al. (2021, Sect. 2.4, Table 1). We run WRF at a spatial resolution of 81 km on a single domain (i.e., non-nested). WRF initial conditions were taken from the ERA-Interim global atmospheric reanalysis (Dee et al., 2011), which has a resolution of approximately 80 km on 60 vertical levels from the surface up to 0.1 hPa. Sea surface temperatures were obtained from the National Centers for Environmental Prediction/Marine Modeling and Analysis Branch (NCEP/MMAB). The WRF model was run with a spin-up period of 12 hours.

The prior flux estimates used in our inversion consisted of four datasets: land biosphere fluxes, fossil-fuel, fires and ocean fluxes. Biosphere carbon fluxes were simulated by the Community Atmosphere-Biosphere Land Exchange model (CABLE) set-up in BIOS3 environment (hereafter referred to as CABLE BIOS3) (Haverd et al., 2018). The CABLE land surface model consists of a biophysical core, a biogeochemical module including a nitrogen and phosphorous cycle (Wang et al., 2010), the Populations-Order-Physiology (POP) module for woody demography and disturbance-mediated landscape heterogeneity (Haverd et al., 2013b), and a module for land use and land management (POPLUC; Haverd et al., 2018). However, the functionality of POPLUC was not considered in BIOS runs, and the land-use change was held to be static at year 2000. CABLE can

be run on global or regional scales. For our regional study case, CABLE was run at a regional scale (resolution 0.25 degree),
and it was forced with Australian regional drivers and observations (BIOS3 set-up). Biosphere fluxes from CABLE (∼NBP)
include gross primary productivity (GPP), net ecosystem respiration (autotrophic and heterotrophic respiration). However, they
do not include carbon losses from fires disturbances, harvest, erosion, and export of carbon in river flow. We used averages of
3-hourly NBP estimates as input for CMAQ (further details of how we constructed NBP can be found in Sect.2.3 Villalobos
et al., 2021). The prior error covariance matrix of the terrestrial biosphere flux from CABLE was assumed to be an approxima-
tion of the net primary productivity (NPP) following the approach of Chevallier et al. (2010) with a ceiling of 3 gC $m^{-2}$ $d^{-1}$.
We assumed that these uncertainties were spatially correlated with length-scale 500 km over land following Basu et al. (2013).
Within our inversion system, no temporal correlations were considered.

Fossil fuel emissions used here were based on two different inventory data sets: the Open-source Data Inventory for An-
thropogenic $CO_2$ (ODIAC) (version 2019) (Oda et al., 2018) and the Emissions Database for Global Atmospheric Research
(EDGAR) (Crippa et al., 2020). We added some missing sectors from the EDGAR inventory to ODIAC (such as aviation climb-
ing and descent, aviation cruise, and aviation landing and take-off datasets). ODIAC is a global gridded product distributed at
$0.1° \times 0.1°$ spatial resolution over land, which uses power plant profiles (emissions intensity and geographical location) and
satellite-observed nighttime lights. We used ODIAC monthly fluxes and incorporated a diurnal scale factor to estimate diurnal
$CO_2$ emission variability (Nassar et al., 2013). Given that the ODIAC product only covers the period from 2015 to 2018, we
repeated the data from 2018 in 2019 but increased the value in each grid cell by 1.7%, which represents the mean annual growth
rate of these emissions from 1970 to 2018. EDGAR is also gridded at $0.1° \times 0.1°$ with monthly temporal resolution. There is
no EDGAR gridded product for 2016–2019, so we repeated the 2015 product to cover the other years. We increased EDGAR
aviation emissions by 2.5%, which represents the mean growth rate in this emissions sector from 2016 to 2019. Fossil fuel
prior uncertainties were assigned to be 0.44 times the value of the monthly fossil fuel estimates described above (see details in
Sect. 2.3. in Villalobos et al., 2021). Errors in fossil fuel emissions were assumed to be uncorrelated.

Ocean flux estimates were selected from CAMS global data (version v19r1) (Chevallier, 2019). Ocean prior uncertainties
were assumed to be 0.2gC $m^{-2}$ $d^{-1}$ and uniform across the ocean, as in Chevallier et al. (2010). Similar to correlations for
biosphere prior uncertainties, uncertainties of ocean fluxes were assumed to be correlated in space with length-scale 1000 km.
Fire prior emissions were selected from the Global Fire Emission Database (GFED), version 4.1s, which includes emissions
from small fires. Fire emissions uncertainties were assumed to be 20% of the GFED emissions and correlated in space with
length-scale 500 km, but not in time. The combination of all prior fluxes was regridded to the spatial resolution of the CMAQ
model.

## 2.4  OCO-2 observations and their uncertainties

Our regional inversion assimilates satellite observations derived from NASA's Orbiting Carbon Observatory-2 (OCO-2; El-
dering, 2018). The OCO-2 satellite instrument carries a single instrument that incorporates three-channel imaging grating
spectrometers developed to measure reflected sunlight by the Earth's surface in three spectral bands: two $CO_2$ spectral bands
in the shortwave infrared (SWIR) at 1.6 and 2.1 μm and one in the near-infrared (NIR) ar 0.76 μm ($O_2$ A-band). From these

radiance spectra is possible to calculate the column-averaged dry-air mixing ratio of carbon dioxide. OCO-2 employs three different sampling strategies to collect data: nadir, glint and target mode. Nadir observations provide useful information over land because the satellite points straight down at the surface of the Earth (surface solar zenith angle is less than $85°$). In glint mode the instrument points to the bright glint spot on Earth where solar radiation is directly reflected off the Earth's surface (local solar zenith angle is less than $75°$). In Target mode, the instrument points towards a specific location on the ground. Target mode is use for validation, where the performance of the instrument is validated against ground-based observations from the Total Carbon Column Observation Network (TCCON) (Wunch et al., 2011).

In this study, the regional inversion was performed using the combination of both land (nadir and glint) (LNLG) OCO-2 observations (version 9). We used the combination of both datasets because it has been demonstrated by Miller and Michalak (2020) that combining both modes provides a stronger and better constraint of $CO_2$ fluxes at regional scales. Also, both datasets present negligible bias (O'Dell et al., 2018). We did not incorporate ocean glint measurements in our inversion, because ocean observations still have undetermined biases (O'Dell et al., 2018), which might impact the Australian carbon flux estimates.

OCO-2 LNLG dataset were selected from December 2014 to December 2019. We considered OCO-2 data since December 2014 because we run CMAQ with a spin up of one extra-month. As an example, Fig. E1 in the Appendix show the spatial pattern of OCO-2 soundings (LNLG) that fall in our CMAQ domain for 2015. In these Figures, we can see that OCO-2 data provides a very good coverage over the Australian region. Such spatial coverage offers good potential to help constrain regional biosphere $CO_2$ fluxes.

Given that the OCO-2 spatial resolution ($1.29$ km $\times$ $2.25$ km) is higher than the CMAQ model grid cell ($81 \times 81$ km), the OCO-2 data were averaged to the CMAQ model grid-level following a two-step process described in (Sect 2.3, Villalobos et al., 2021). The first step involves averaging all OCO-2 soundings across 1-second intervals, while the second step involves averaging these 1-second averages into the CMAQ vertical column (approximately 11-seconds averages). The algorithm to estimate the uncertainties across 1-second averages follows Crowell et al. (2019). Here, we considered three different forms of uncertainty calculation. First, we assumed that uncertainties that fall within 1-second span were perfectly correlated in time and space (uncertainties defined as $\sigma_s$). Second, given that the average of OCO-2 uncertainties ($\sigma_s$) is relatively lower than the real OCO-2 uncertainties (mainly because they only consider the errors from measurement noise, and not systematic errors), we also used the spread (standard deviation) of the OCO-2 retrievals in the 1-second average (uncertainties defined as $\sigma_r$). Third, we also considered a baseline uncertainty (defined as $\sigma_b$) for cases where the number of OCO-2 soundings was not enough to compute a realistic spread. Our baseline uncertainties were assumed to be 0.8 ppm over land and 0.5 ppm over ocean. Finally, we selected the maximum value between these three uncertainties ($\sigma_s$, $\sigma_r$, and $\sigma_b$). For each grid-cell, we also added (in quadrature) to this term 0.5 ppm as the contribution of the CMAQ model uncertainty (defined as $\sigma_m$). We also increase the final observation uncertainty by a factor of 1.2 to satisfy the theoretical assumptions of the inversion (Villalobos et al., 2021). We interpolated the retrieval OCO-2 profile to the CMAQ model vertical profile as described in (Sect. 2.6., Villalobos et al., 2020). Note that we only selected OCO-2 retrievals with quality flag "0" and bias-corrected data, as described by Kiel et al. (2019).

### 2.5 Validation data

#### 2.5.1 TCCON

For validation of our inversion, we compared our posterior column averaged concentration simulated by CMAQ against the TCCON sites located in Australia and New Zealand (Fig 2). TCCON is a network of ground-based Fourier Transform Spectrometers (FTS) recording direct solar spectra in the NIR/SWIR spectral region (Wunch et al., 2011). From these spectra, accurate and precise total column amounts of $CO_2$ and other trace gases are retrieved. In our study domain, there are three TCCON stations (Darwin, Wollongong and Lauder). The Darwin and Wollongong sites are located within Australia, while the Lauder site is located in New Zealand. The Darwin and Wollongong sites are operated by the Centre for Atmospheric Chemistry at the University of Wollongong, Australia (Griffith et al., 2017a, b). The Lauder site is operated by New Zealand's National Institute of Water and Atmospheric Research (NIWA) (Sherlock et al., 2017; Pollard et al., 2019). As is shown in Fig 2, the Lauder monitoring station is located on the South Island of New Zealand at 2 km north from the town of Lauder. It is sheltered from the prevailing wind direction by the Southern Alps, which increases the number of days with clear skies and results in an air mass that is largely unmodified by regional anthropogenic sources (Pollard et al., 2017). From mid-2015, the Darwin site has been located about 9 km east of Darwin city, approximately 4.5 km south-east of its previous location (Deutscher et al., 2010). The Wollongong site is a coastal site close to populated areas and industry to the north, and native forest and less dense population to the south and west (Deutscher et al., 2014). At each site, TCCON data were selected within one hour windows and averaged to be consistent with temporal resolution of the output of the CMAQ simulations. Each TCCON retrieval is provided with an averaging kernel and a prior profile, which were interpolated to the CMAQ vertical profiles. After the interpolation, we applied the averaging kernel (following Eq.15 Connor et al., 2008) to compute the TCCON CMAQ simulated $CO_2$ concentrations. The residual between CMAQ and TCCON was constructed based on monthly mean concentrations, which were calculated by taking local time averages (10:00 – 14:00 LT), where the solar radiation intensity is most stable (Kawasaki et al., 2012).

#### 2.5.2 Ground-based in-situ measurements

We also compared our posterior concentrations against four ground-based in-situ monitoring sites: Cape Grim, Gunn Point, Burncluith and Ironbark, whose geographic locations are shown in Fig. 2. These monitoring sites form part of the Global Atmosphere Watch (GAW) Programme of the World Meteorological Organisation (WMO), and they are operated by CSIRO's Climate Science Centre located in Aspendale, Australia. We used hourly data from these monitoring sites, but the monthly mean averaged data shown in Section 3.4.2 were calculated using local time averages (12:00–05:00 LT, Australian local time, local referred to the monitoring site locations).

Atmospheric $CO_2$ concentration measurements at the Gunn Point, Ironbark and Burncluith sites are made continuously at high frequency (∼0.3 Hz) using Picarro cavity ring-down spectrometers. Instruments located at the Gunn Point and Ironbark sites use the Picarro model (G2301), while the Burncluith site uses a model G2401. All the inlets are placed at the height of 10 m. Descriptions of the Ironbark, Gunn Point and Burncluith installations can be found in Etheridge et al. (2016). Cape Grim also

225 operates a Picarro G2301 analyser; however, the inlet is positioned at 70 m. The instrument precision for these spectrometers is better than 0.1 ppm (Etheridge et al., 2014) and all measurements are calibrated to the World Meteorological Organization (WMO) X2007 $CO_2$ mole fraction scale (Zhao and Tans, 2006), ensuring comparability between all measurements used. We note that we used "baseline" and "non-baseline" data from Cape Grim. Baseline data is selected when winds blow straight off the Southern Ocean and have not been in recent contact with land. In this study, we used both datasets because our inversion 230 only uses OCO-2 soundings located over land.
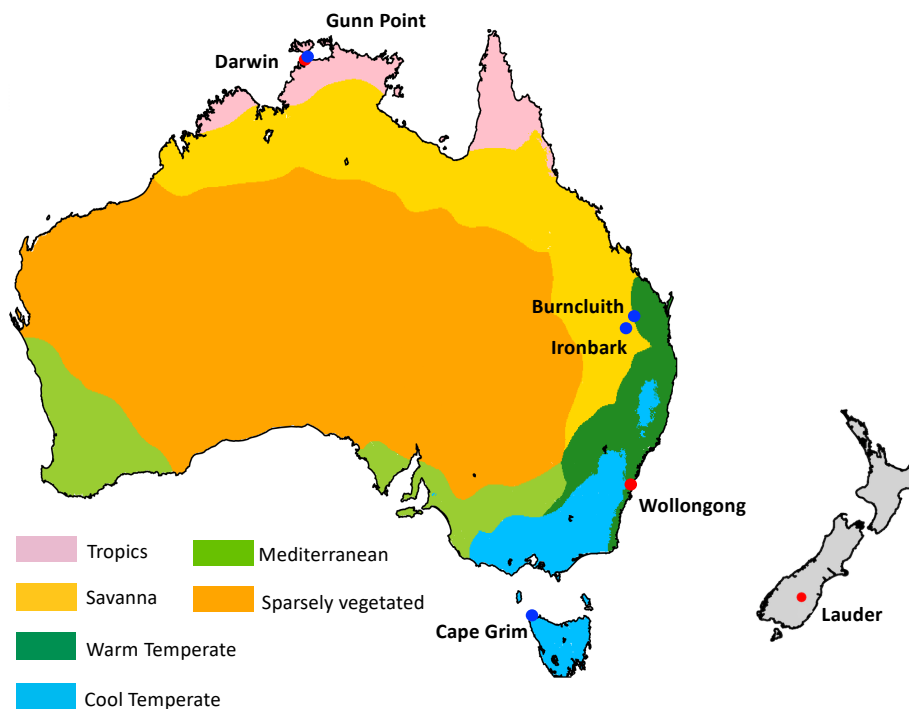
**Figure 2.** Location of the Total Carbon Column Observing Network (TCCON) sites across Australia and New Zealand (red points) and in-situ sites (blue points). This map also shows a classification of six bioclimatic regions for Australia.

## 2.6   Australian bioclimatic classification

To understand which ecosystems contributed the most to the Australian inter-annual carbon flux variability between 2015–2019, we divided the continent into six bioclimatic classes: tropical, savanna, warm temperate, cool temperate, Mediterranean and sparsely vegetated (Fig. 2). We used the same six bioclimatic regions at a 0.05° spatial resolution as in Haverd et al. 235 (2013a). The classes were regridded over our CMAQ grid ($81 \times 81$ km) resolution.

## 2.7   Climate data

In order to analyse the impact of climatic drivers on Australian terrestrial carbon cycle variability, we investigated the anomalies of rainfall and temperature across Australia for the period 2015-2019. Rainfall data were selected from the Australian Water

Availability Project (AWAP), Bureau of Meteorology (BOM) (Jones et al., 2009) for the period 2015 to 2019. AWAP is a gridded product at 0.05° resolution. It is generated by spline interpolation of in situ rainfall observations. We also used air temperature data at 2 m above the land surface from ERA5, the fifth generation of European Centre for Medium-Range Weather Forecasts (ECMWF) atmospheric reanalyses. The dataset selected from ERA5 was monthly and it was gridded at 0.25 degrees spatial resolution. We constructed 3-month running means of rainfall anomalies and air temperature anomalies relative to a mean across 2015-2019. These anomalies were calculated by subtracting their long-term mean (2015–2019) for each month from the raw time series and constructing the 3-month running mean on the resultant time series. We regridded the rainfall anomalies onto the grid of the CMAQ model in order to simplify the comparison with the estimated terrestrial carbon uptake from the flux inversions.

## 2.8 Enhanced vegetation index (EVI) as an indicator of the vegetation greenness

Plant photosynthesis and respiration are two fundamental physiological processes in the carbon cycle. Physiological and structural changes in vegetation modulate the exchange of $CO_2$ between the land and atmosphere. In order to understand what physiological factors drive the inter-annual variability of our posterior fluxes, we studied the anomalies of the enhanced vegetation index (EVI). EVI provides information on vegetation state, and we used it to characterize changes in Australian vegetation greenness and activity (e.g photosynthesis) from 2015 to 2019. The EVI product was derived from the Moderate-Resolution Imaging Spectroradiometer (MODIS) MOD13C1 version 6 data product, which flies on board Terra, a NASA earth-observing satellite (Didan, 2014). The MODIS EVI is a gridded product, which has a temporal resolution of 16 days composite and 0.05-degree spatial resolution. The EVI ranges from -0.2 to +1, where values less than 0 indicate a lack of green vegetation or arid areas. We calculate the 3-month running mean of EVI anomalies in Australia relative to the long-term mean from 2015-2019 and subtract the mean seasonal cycle. These monthly EVI MODIS products were also regridded into the CMAQ domain to calculate the temporal correlation between prior and posterior flux anomalies.

## 2.9 Gross Primary Productivity (GPP)

To understand the difference between posterior and prior fluxes, we compared the climatological seasonal cycle of the gross primary productivity (GPP) from the CABLE BIOS3 model against the remote-sensing based DIFFUSE model (Donohue et al., 2014), and the latest MODIS terra GPP product (MOD17A2H version 6) (Running et al., 2015) for the period 2015–2019. We also calculated 3-month running mean GPP anomalies for these three datasets.

The DIFFUSE GPP estimates are taken to be the product of the fraction of photosynthetically active radiation (PAR) absorbed by vegetation and the light-use efficiency. These datasets have a temporal resolution of 16-days at 250 m resolution. Similar to the DIFFUSE estimates, the MODIS GPP product is based on a light-use efficiency approach and provides a cumulative 8-day composite product gridded at 500 m. For comparison, the CABLE BIOS3, DIFFUSE and MODIS GPP products were averaged to a monthly resolution and regridded over the CMAQ domain.

## 2.10 Global Atmospheric Inversions

We compared our Australian assimilated fluxes against nine independent global atmospheric inversions: AMES, PCTM, CAMS, CMS-Flux, CSU, CT, OU, TM5−4DVAR, UT (Sect. 4). These global inversions are part of the OCO-2 Model Intercomparison Project (MIP) (Crowell et al., 2019; Peiro et al., 2021). In this study, we used the OCO-2 MIP flux version found in Peiro et al. (2021). In Peiro et al. (2021), the global inversions were performed using the assimilation OCO-2 (version 9, bias-corrected) from 2015-2018. A summary of these nine global inversions is given in Table 1, and a complete description of them and their input fields can be found in Peiro et al. (2021, Appendix A: model information). We can see in Table 1 that all global inversions were run using different inverse systems and were configured at different spatial resolutions with different atmospheric transport models and prior fluxes. Some global inversion methods use a four-dimensional variational (4D-Var) approach, while others utilize the technique known as ensemble Kalman filter (EnKF) or Bayesian synthesis.

**Table 1.** Summary of the configuration of the MIP OCO-2 (version 9) design.

| Acronym | Transport Model | Meteorological fields | Grid spacing (degree) | Prior Land Biosphere | Prior Fire | Inverse System |
|---|---|---|---|---|---|---|
| AMES | GEOS-Chem | MERRA-2 | $4° \times 5°$ | CASA-GFED4.1s | GFED4.1s | 4D-Var |
| Baker | PCTM | MERRA-2 | $6.7° \times 6.7°$ | CASA-GFED3 | GFEDv3 | 4D-Var |
| CAMS | LMDz | ERA-Interim | $1.9° \times 3.75°$ | CMEMS | GFEDv4 | Variational |
| CMS-Flux | GEOS-Chem | GEOS-FP | $4° \times 5°$ | CARDAMOM | GFED4.1s | 4D-Var |
| CSU | GEOS-Chem | MERRA-2 | $1° \times 1°$ | SIB4 | GFED4 | Bayesian synthesis |
| CT | TM5 | ERA-Interim | $3° \times 2°$ $1° \times 1°$ | CT2019 CASA GFED4.1s | CT2019 CASA-GFED4.1s | EnKF |
| OU | TM5 | ERA-Interim | $4° \times 6°$ | CASA-GFED3 | GFEDv3 | 4D-Var |
| TM5-4DVAR | TM5 | ERA-Interim | $2° \times 3°$ | SIB-CASA | GFEDv4 | 4D-Var |
| UT | GEOS-Chem | GEOS-FP | $4° \times 5°$ | BEPS | GFEDv5 | 4D-Var |

## 2.11 FLUXCOM carbon fluxes

We also compared our assimilated fluxes against the FLUXCOM net ecosystem exchange (NEE) ensemble mean product. The FLUXCOM dataset is created using machine learning approaches, which combine data from FLUXNET eddy covariance towers (at site level observation) with satellite remote sensing, and meteorological data to estimate carbon fluxes such as NEE and along with their uncertainties (Jung et al., 2020; Tramontana et al., 2016). For this study, we downloaded the products at a monthly temporal resolution from the data portal of the Max Planck Institute for Biogeochemistry (https://www.bgc-jena.mpg.de).

## 3 Results

### 3.1 Inversion performance

In our inversion system, the L-BFGS algorithm iteratively adjusts the control vector until the cost function reaches an optimal solution. In Bayesian inverse problems we require that the observational residuals (simulated − observed) and increments (posterior − background) are consistent with the assumed probability density functions (PDFs). This implies that the cost function should be approximately half the number of observations (Tarantola, 1987, p.211). Table 2 shows the analysis of convergence for our five-year inversion. In this table, we can see that for each year, the ratio between final cost function $J(\boldsymbol{x})$ and observation was about 0.5, indicating that our system is self-consistent.

**Table 2.** Convergence diagnostics of the inversion system using OCO-2 satellite data.

| Year | $J_0(\boldsymbol{x})$ | $\nabla_x J_0$ | $J_f(\boldsymbol{x})$ | $\nabla_x J_f$ | N observations | Theoretical $J(\boldsymbol{x})$ | Ratio ($J_f(\boldsymbol{x})$ and N) |
|------|------|------|------|------|------|------|------|
| 2015 | 5653.15 | 5177.65 | 4403.01 | 394.17 | 8766 | 4383 | 0.50 |
| 2016 | 5561.51 | 5371.69 | 4380.64 | 853.07 | 8946 | 4473 | 0.49 |
| 2017 | 4485.17 | 4794.40 | 3477.63 | 335.92 | 7514 | 3757 | 0.46 |
| 2018 | 5118.29 | 3825.28 | 4112.01 | 365.46 | 9679 | 4839 | 0.42 |
| 2019 | 5582.00 | 2719.85 | 4443.32 | 387.14 | 10373 | 5186 | 0.43 |

Fig. 3 shows the monthly bias, and root-mean-square error (RMSE) between the prior and posterior column integrated concentrations simulated by CMAQ against the OCO-2 observations. In this figure, we can see that, in general, the inversion reduces prior biases significantly to values close to zero. As an indication of the overall inversion performance, the Australian mean prior bias for 2015 – 2019 was reduced from 0.23 to 0.06 ppm, and the RMSE was reduced from 0.90 to 0.76 ppm (Appendix A, Fig. A1).

While we see that inversion reduces the prior biases significantly, relative small positive systematical posterior biases remain (0.05 ppm). These systematic positive posterior biases across Australia may likely be driven by sampling and residual retrieval biases in the OCO-2 data. Some studies suggest that the existing OCO-2 cloud screening algorithm (Taylor et al., 2016) has difficulty identifying sub-field of view, and that unresolved clouds introduce a bias in the retrieved column of $CO_2$ concentration.

We note the data gap in August and September was caused by a satellite outage. In November 2017, we saw the prior concentration underestimates the observations significantly, with biases of about -0.56 ppm and RMSE 1.29 ppm. High prior biases in this month were found along the east coast of Australia, suggesting that the CABLE model might likely be underestimating the carbon outgassing in this area and, therefore, the prior retrieval column $CO_2$ concentration. The reduction of the prior biases in this month was about 90% (-0.06 ppm with an RMSE of 0.94).
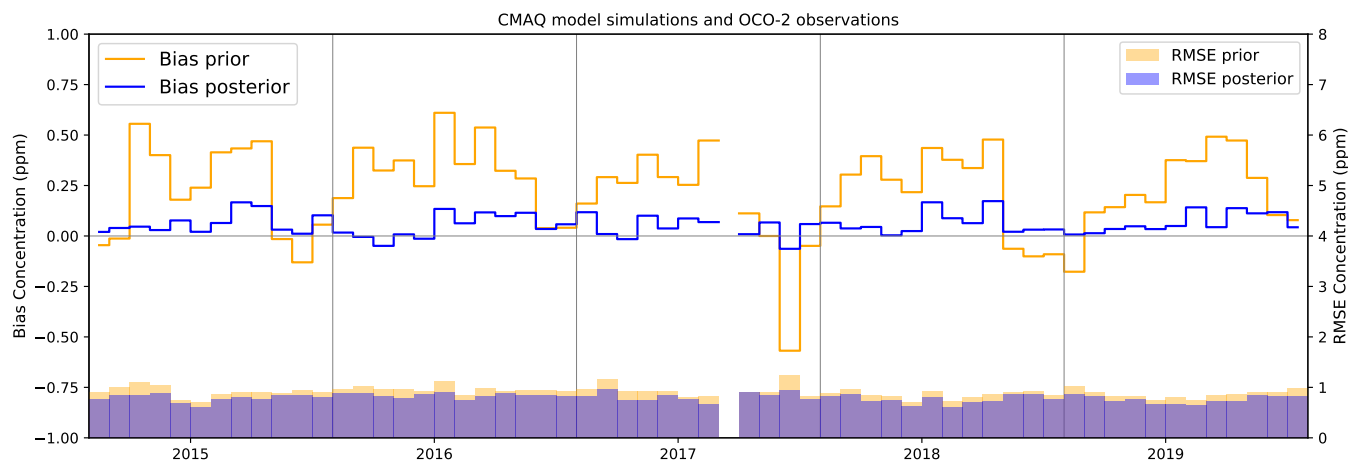
**Figure 3.** Bias and root mean square error (RMSE) between OCO-2 and the prior and posterior concentrations simulated by CMAQ model. Blue and orange lines represent prior posterior concentration biases, and orange and blue lines represent the RMSE.

### 3.2 Seasonal cycle and spatial distribution of the Australian prior and posterior carbon fluxes

Before assessing the interannual variability of the fluxes derived by the assimilation of OCO-2 observations, we first examine the monthly, seasonal, and annual means between the prior and posterior fluxes. This step is relevant to evaluate later how well the posterior column-average concentrations simulated by the CMAQ model fit with independent data. Assessing the robustness of our inversion with independent data will allows us to better explain the posterior flux anomalies derived by our inversion.

Figure 4a shows the long term mean of the prior and posterior carbon fluxes aggregated across Australia for the period 2015 – 2019, and Figs. 4b and c show the annual, and seasonal cycle of these estimates. Posterior flux uncertainties from 2016 to 2019 were assumed to be the same as those calculated for 2015, which were estimated by five different observing system simulation OSSE experiments (see more details in Villalobos et al., 2021).

Our five year inversion suggests that Australia was a carbon sink of -0.46 $\pm$ 0.09 PgC yr$^{-1}$ compared to the prior flux estimate, which was 0.11 $\pm$ 0.17 PgC yr$^{-1}$ (Fig. 4a). Here, the prior flux estimate (fluxes derived by the CABLE model) represents the current knowledge of the Australian carbon budget. Due to the size of the uncertainties in the prior estimate, it cannot be concluded with high confidence whether Australia was a sink or source of $CO_2$ for the period 2015 – 2019. The annual posterior fluxes also suggest that Australia's terrestrial biosphere is able to absorb more carbon from the atmosphere than the CABLE model estimate (Fig. 4b). We also see that 2016 was the year that contributed most to the long term mean sink estimated by the OCO-2 inversion.

In terms of seasonal cycle, we can see that the posterior flux estimates show a stronger seasonality compared to the prior flux estimate (Fig. 4c). Over the five years from 2015 to 2019, we see that OCO-2 sees a strong seasonal biospheric carbon uptake each year between June and September (winter and early spring in Australia), and a stronger carbon source from November to December (late spring and early summer in Australia). As we showed in Fig. 3, the stronger carbon uptake seen in winter

and early spring occurs because the prior column average concentration simulated by CMAQ model overestimate OCO-2 observations in this period.
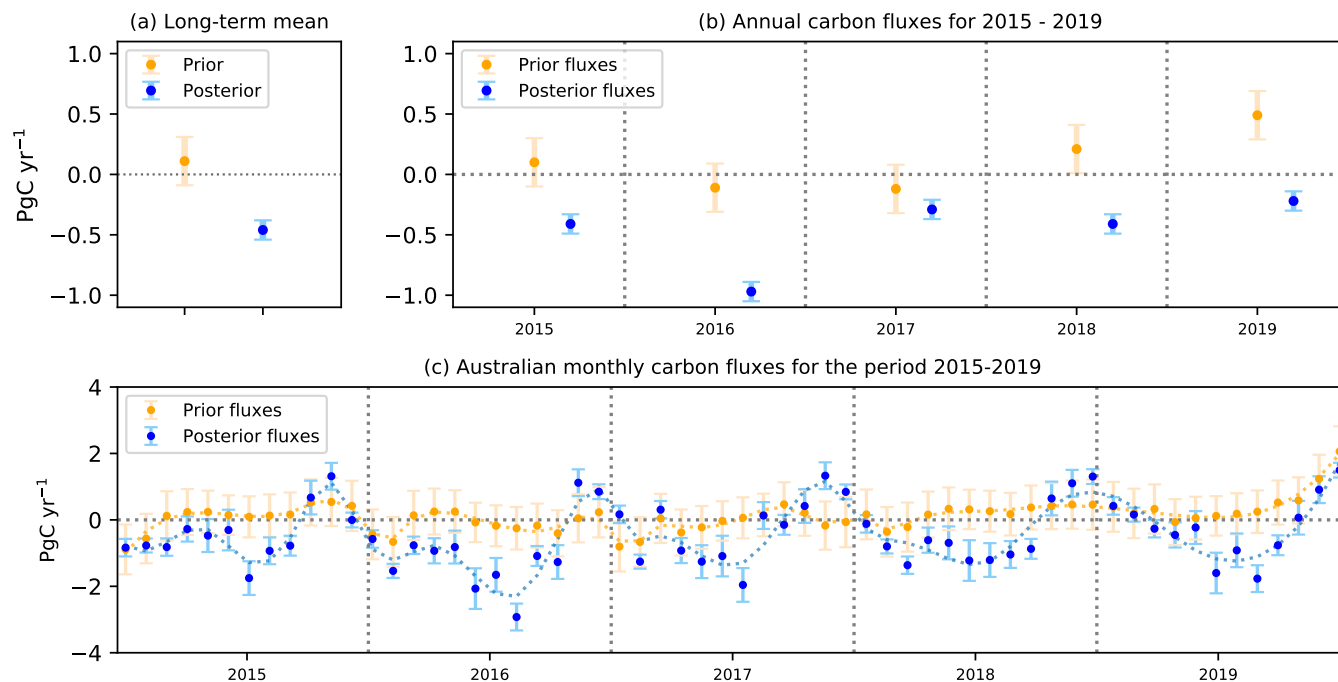
**Figure 4.** (a) Long-term mean carbon flux, (b) annual mean carbon flux, and (c) monthly mean prior (orange dots) and posterior carbon flux (blue dots) and their uncertainties in PgC yr$^{-1}$ over Australia for the period 2015–2019. Uncertainties on the prior and posterior fluxes are indicated by bars. The dashed orange and blue line represents a smooth line for the prior and posterior fluxes, respectively. Within these estimates we only included the terrestrial part of the Australian carbon cycle, including fires but not fossil fuel emissions.

To identify which regions the OCO-2 satellite sees a stronger carbon uptake in Australia, we plotted the annual map difference between the posterior and the prior fluxes (Fig. 5). We can see in Fig. 5a that the majority of the posterior long-term mean flux for the period 2015 to 2019 is distributed in one half of the continent (in the northeast, central and southern regions of the continent). However, we note that this was not the case for the coastal region in these areas, where we observe that OCO-2 recorded a stronger carbon release compared to the prior estimate.

The substantial difference between the prior and posterior flux in 2015 and 2016 comes from the northern and southeast of Australia (excluding coastal areas in the southeast of the continent). We will show later in Section 3.5 that the stronger carbon uptake recorded by the inversion (relative to the prior) in these two years was driven by an increase in vegetation productivity due to a rise in rainfall and low temperature across these regions. Despite the fact that 2016 was one of the strongest El Niño events on record in the Pacific Ocean, the rain over Australia was above average for most of the continent. The annual climate report from the Bureau of Meteorology for 2016 indicates that the annual rainfall over Australia was 17 per cent above the 1961–1990 average. In 2017, prior and posterior differences were seen in the northern, central and east coastal areas of

345  Australia. Rainfall in 2017 was below average for much of eastern Australia and along the west coast of Australia. For 2019, OCO-2 recorded a stronger carbon release in western and central Australia. These results are not unexpected because 2019 was an exceptional year (the hottest and driest year on record in Australia), where the mean temperature was 1.52 °C above the 1961–1990 average (Annual climate statement, Bureau of Meteorology, 2019). We also noticed a large carbon uptake (relative to prior) in the southeast corner of Australia recorded in 2019 (Fig. 5f).
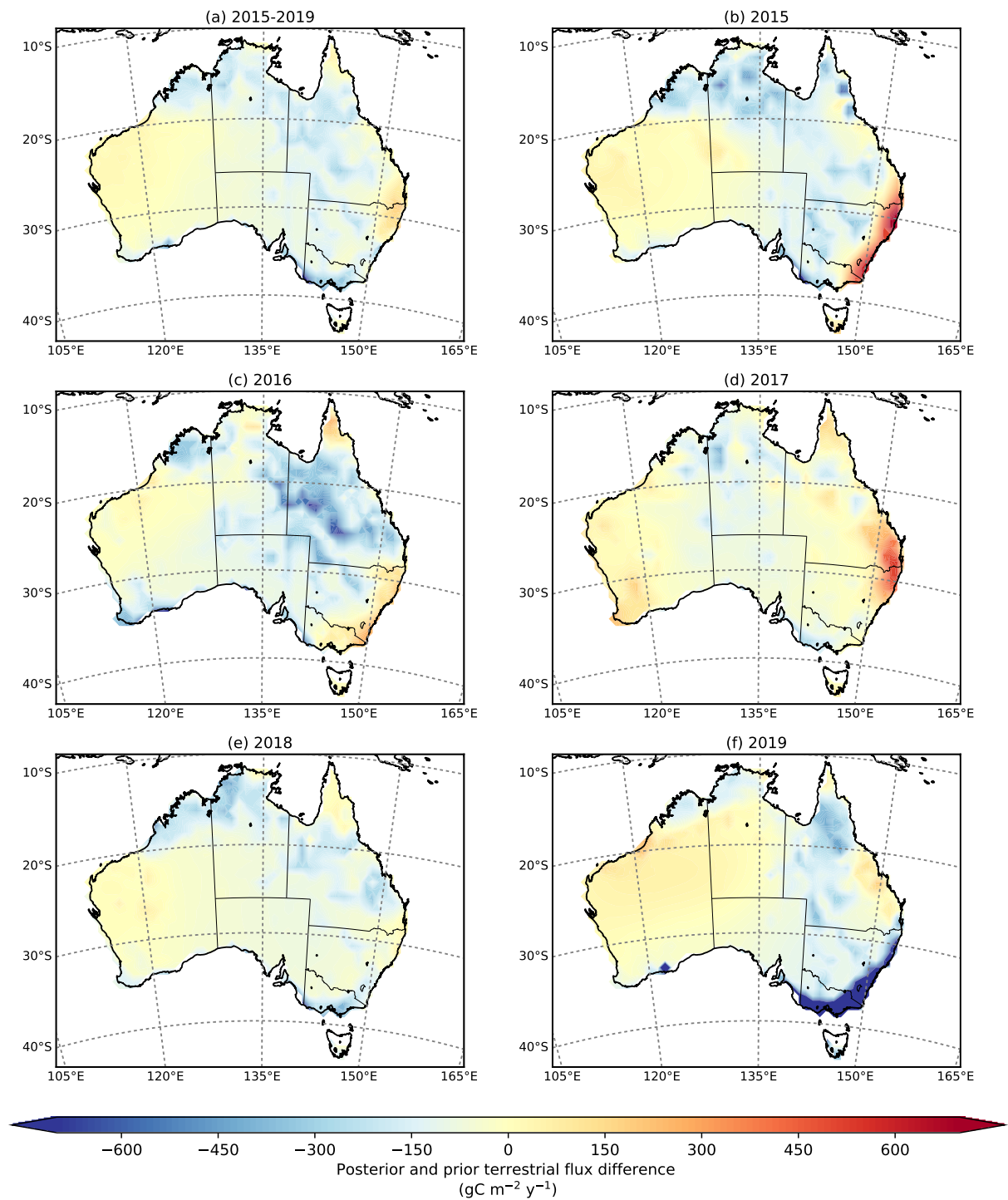
**Figure 5.** Annual spatial pattern of the differences between posterior and prior carbon fluxes for 2015-2019 (gC m$^{-2}$ yr$^{-1}$).

## 3.3 Climatological seasonal cycle of the prior and posterior carbon fluxes aggregated by bioclimatic regions

To further examine what might potentially be the cause of the difference between posterior and prior fluxes described above, we compared the climatological seasonal cycle (Fig. 6) against the climatological seasonal cycle of the gross primary productivity (GPP) fluxes derived from CABLE BIOS3, MODIS and the DIFFUSE model (Appendix C, Fig. C1). We made this comparison by aggregating the fluxes over six bio-climatic regions.

It is evident that the largest difference between prior and posterior flux estimates is over savanna (Fig. 6b) and sparsely vegetated (Fig. 6d) ecosystems. Over the savanna region, the most notable difference is seen from June to September. The absolute difference in this period is about 0.4 to 0.5 PgC yr$^{-1}$. According to MODIS and DIFFUSE GPP estimates, the stronger posterior sink observed in this period may be due to an underestimation of GPP simulated by the CABLE BIOS3 model (Fig. C1b). The GPP estimated by MODIS from June to September was about 0.90 PgC yr$^{-1}$ compared to CABLE BIOS3, which was 0.59 PgC yr$^{-1}$. DIFFUSE GPP estimates were around 0.68 PgC yr$^{-1}$.

Over the sparsely vegetated region, the seasonal discrepancy between the prior and posterior flux is more evident than for savanna. The seasonality of the posterior flux is stronger (relative to the prior estimate) from April to September. In this ecosystem, the largest absolute difference between the prior and posterior fluxes is seen from June to August (0.5 PgC yr$^{-1}$). In July, for example, the inversion shifts the prior flux from -0.05 $\pm$ 0.09 PgC yr$^{-1}$ to -0.56 $\pm$ 0.06 PgC yr$^{-1}$. Again, we can see in Fig. 6d that a possible reason of this shift may be associated with an underestimation of the GPP by CABLE BIOS3. It is evident that MODIS and DIFFUSE GPP have a stronger seasonality compare to CABLE BIOS3 GPP. For example, from June to August, the CABLE BIOS-3 GPP was about 0.4 PgC yr$^{-1}$ compared to DIFFUSE and MODIS, which were 0.9 and 1.3 PgC yr$^{-1}$ respectively. We did not find a seasonal correlation between the prior fluxes and MODIS and DIFFUSE GPP fluxes (see Appendix G, Table G1), but we did find a positive correlation between the posterior fluxes and the GPP estimated by MODIS and DIFFUSE (R = 0.44 and R = 0.45 respectively).

Regarding the tropics, warm temperate, cool temperate, and Mediterranean ecosystems, the seasonal correlation MODIS or DIFFUSE GPP estimates were stronger for the prior than for the posterior fluxes (Appendix G, Table G1). A stronger correlation between the prior flux and MODIS and DIFFUSE might be attributable to the fact that the assimilated coastal fluxes might be somehow less constraint by the inversion in these ecosystems, mainly because they are mostly influenced by ocean fluxes where the uncertainties have less freedom to be modified by the inversion.
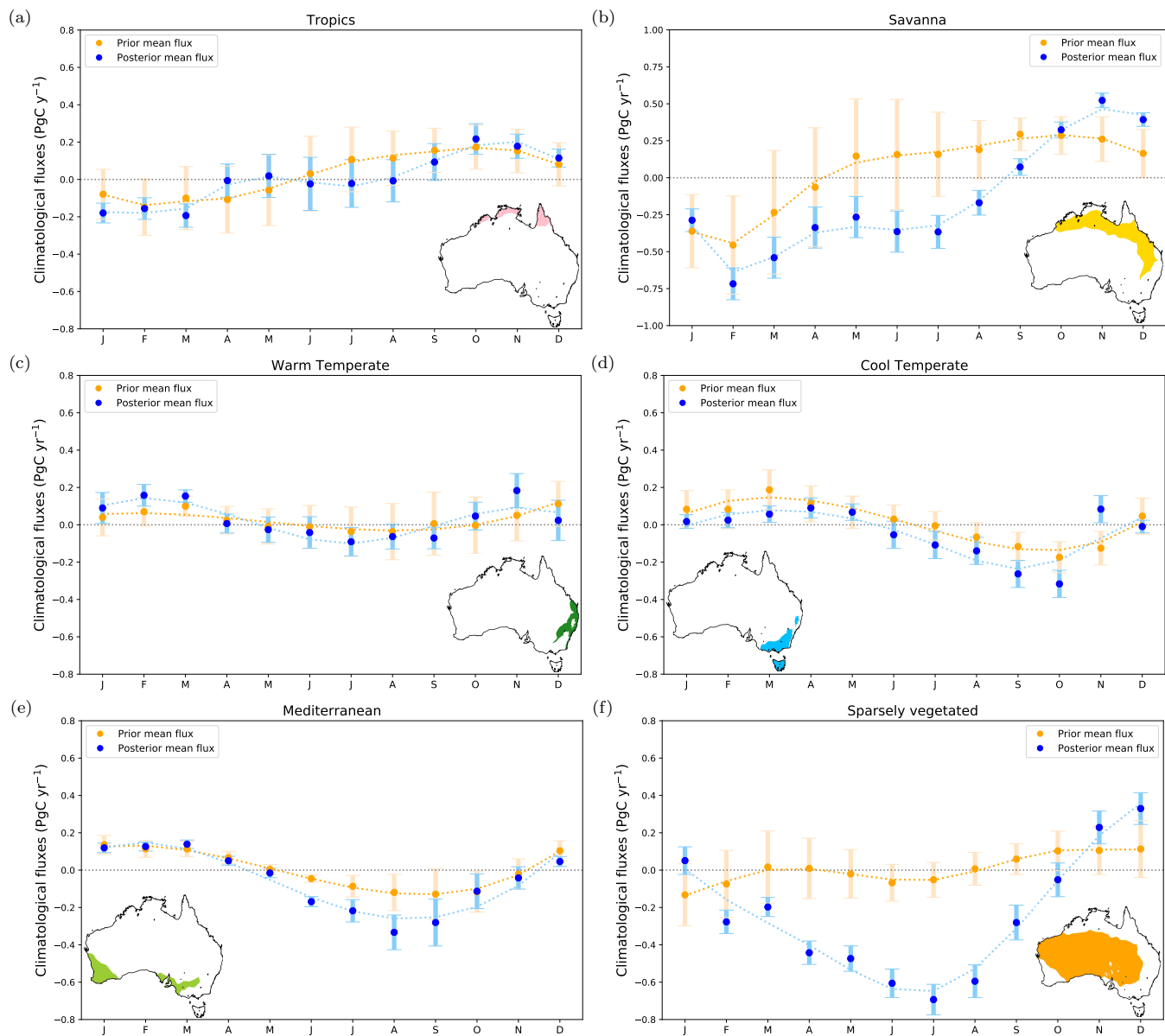
**Figure 6.** Climatological seasonal cycle of prior (orange points) and posterior (blue points) terrestrial carbon fluxes (2015–2019). The dashed orange and blue line represents a smooth line for the prior and posterior fluxes, respectively.

## 3.4  Evaluation of the inversion against independent data

To evaluate the accuracy of the posterior fluxes discussed in the previous section, we assess the fit between the posterior concentration $CO_2$ field (derived by running the CMAQ model with the fluxes assimilated by OCO-2) with independent $CO_2$

measurements: TCCON (Darwin, Wollongong, and Lauder) and in situ measurements (Gunn Point, Ironbark, Burncluith and Cape Grim).

### 3.4.1 Comparison with TCCON data

Figs. 7a, c and e show the time series of the monthly mean column-averaged $CO_2$ concentrations at TCCON sites (Darwin, Wollongong and Lauder) compared to the column-average concentration from prior and posterior simulated by CMAQ for 2015 – 2019. Figs. 7b, d and f show the bias and root mean square error (RMSE) from these averages. Monthly averages were computed using data selected between $10:00-14:00$ (Australia and New Zealand local time).

For all TCCON sites, we found that assimilating OCO-2 data only slightly reduced prior bias and the RMSE. At Darwin site (Fig. 7a), the fit between posterior column-average concentration and TCCON notoriusly degrade at the beginning of 2017, 2018 and 2019 (mainly February and March). High negative posterior biases (2 ppm) are may be related to the small number of OCO-2 soundings located around the site or local biases in the OCO-2 data (Peiro et al., 2021). The small number of OCO-2 observations around Darwin is due to the presence of cloud cover and aerosols. While in summer, Northern Australia experiences a wet season (November to April), which is highly impacted by monsoonal rains and storms. Winter, the dry season in this region, is affected by fires. Some studies (i.e. Taylor et al., 2016) suggest that some OCO-2 retrievals can be biased by clouds during the wet season and smoke aerosol plumes during the dry season, mainly because the OCO-2 cloud screening algorithms present some difficulty in identifying clouds near the surface. With regard to correlation analysis, we also found that the relationship between observations and the posterior simulations is improved in some periods (see Appendix F, Table F1).

Evaluation at the Wollongong site (Fig. 7c) also shows systematic differences with our posterior concentrations. From 2016 onwards, we see a persistent slight underestimation of the prior and posterior column average simulated by CMAQ. Similar to Darwin, the posterior estimates derived from the inversion do not help much to reduce the prior biases at this site. In general, we see the prior, and posterior biases remain almost the same (biases are less than 1 ppm), except in winter 2015, where biases are about 1.5 ppm. Considerable reduction of the prior biases are only seen in summer 2016/2017 (November and December), where the prior biases were reduce by 20 and 80%. As discussed in Villalobos et al. (2021), the improvement in bias is negligible when the wind blows from the ocean to this site or not many OCO-2 soundings were found around the monitoring location. Improvements in correlation at Wollongong site are shown in Appendix F, (Table F3).

Unlike Wollongong site, we see a persistent overestimation of both the prior and posterior estimates at TCCON Lauder (Fig. 7c). However, posterior biases are less than 1 ppm. Prior biases at the Lauder site were mainly reduced in winter and early spring. The reduction of the biases at this site was modest (about 10 to 25%). New Zealand is (relative to the Australian mainland) much smaller and narrower along the south-west to north-east direction, and thus strongly affected by oceanic airflow. The smaller size means relatively few OCO-2 soundings are retrieved over this area. Ocean fluxes that affect New Zealand have less freedom to be modified due to the small prior uncertainties assumed in the inversion. Analysis of the correlation is shown in Appendix F, Table F2.
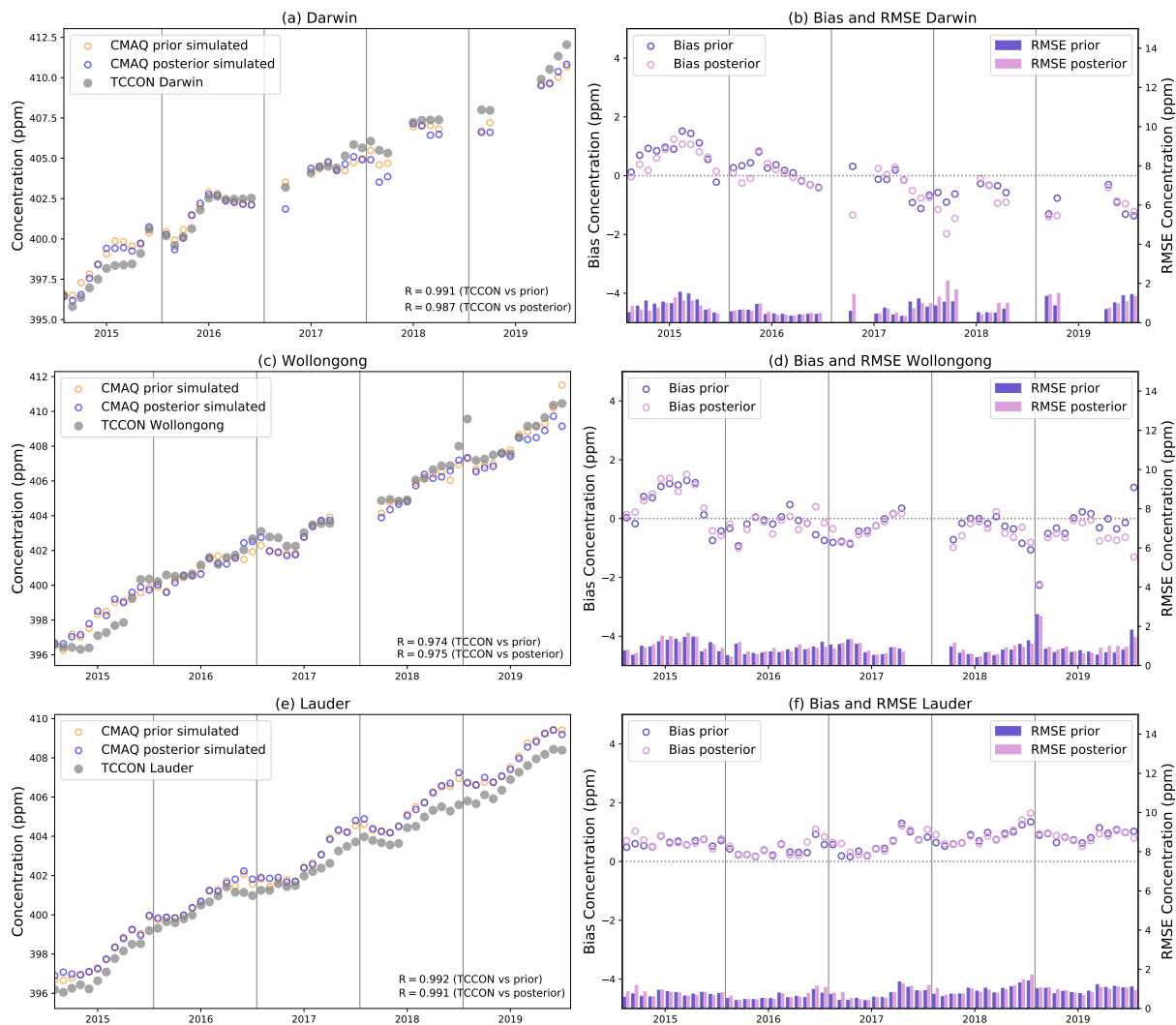
**Figure 7.** Comparison between the monthly mean column-averaged, bias and root mean square error (RMSE) at (a, b) Darwin, (c, d) Wollongong, and (e, f) Lauder TCCON sites and the CMAQ prior and posterior modeled $CO_2$ concentrations for 2015–2019. Orange and blue circles represent the prior and the posterior mean concentration, while the grey dots represents TCCON observations.

### 3.4.2 Comparison with ground-based in situ measurements

Figs. 8a, c and e show the comparison between ground-based in situ measurements (Gunn point, Burncluith, Ironbark and Cape Grim) and the prior and posterior simulated by the CMAQ model at the surface for 2015–2019, and Figs. 8b, d and f show the bias and root mean square error (RMSE) from these averages. Averages were computed using data selected between $12:00 -$
415    17:00 (Australia local time).

    We note that at Gunn Point site, in general, the posterior column-average concentrations underestimate the observations. The prior concentration indicates a better agreement, but biases are still significant. Some possible explanations for these

results might be related to the limited vertical resolution of these retrievals and, consequently, the relative inability of OCO-2 to constrain fluxes at the scale relevant to this site (total column measurements are less sensitive at the surface than in-situ sampling). Another possible explanation is that within our model, Gunn Point is a coastal site which is affected by prevailing offshore winds. If winds come from the ocean, our fluxes are less constrained by OCO-2 retrievals (see plot of wind directions Supplementary; Figs. S20 and S24 January −February).

The data for the Burncluith site spans July 2015 to May 2018 (Fig. 8b). At this site, posterior biases seem to vary seasonally. It is clear the posterior biases are larger (relative to the prior bias) in the winter season (June, July and August) compared to the summer season (e.g., January and February) and spring (e.g., September and October). In this period, the prior concentrations show a better agreement with the observations, with biases (range between 0.54 to -0.46 ppm) compared to the posterior biases (range between -2.79 to -3.57 ppm). Large negative posterior biases at this site could be related to errors in the transport of the CMAQ model (e.g., associated with parameterization scheme within the planetary boundary layer) or erroneous meteorological inputs from our WRF simulations (forcing errors). Transport errors in the vertical mixing near the surface associated with incorrect treatment of atmospheric turbulence can cause significant biases in simulated concentrations (Gerbig et al., 2008; Lauvaux et al., 2012). The atmospheric boundary layer mixing height is an important property in atmospheric modelling because it gives the volume of a column of air in which the fluxes contribute to the $CO_2$ concentration. In this study, it is difficult to quantify the likely error in the simulation of boundary layer height because the site lacks the relevant physical measurements. More discussion of these findings is found in Section 4. We also did not find much improvement in the correlations at this site (see Appendix G, Table G4).

Results for the Ironbark monitoring station are similar to Burncluith. These results were not unexpected given the stations' proximity (Fig. 2). For 2015 and 2016, validation against the Ironbark site also shows that the posterior mean concentrations were in good agreement with the observations for the summer and spring seasons. In February 2018, we see the posterior biases were about -11.4 (RMSE = 21.61). The difference between the posterior simulation and the observations may be related to a single event visible to the surface station but not seen by OCO-2. On February 7th, Ironbark registered a concentration of $CO_2$ of 459.87 ppm. It is possible that fires may have caused the high $CO_2$ concentration registered in this period (see information for February 2018 at NASA Fire Information for Resource Management System (FIRM, 2020). From April 18th to 20th, we also see a similar event that was not captured by the inversion, causing a posterior concentration bias of -6.44 ppm (RMSE = 9.82). During these 3 days, the concentrations registered at Burnlcluith were greater than 450 ppm.

Cape Grim is the only site with a complete time-series of observations during this period (Fig. 8d). Like Gunn Point, Cape Grim is a coastal site affected by strong westerly winds that blow from the ocean into Tasmania. We can see in Fig. 8d that there is an evident underestimation of our posterior fluxes from 2015 to 2019. However, there are some months in 2015, 2016 and 2017 that we see a significant reduction in the prior bias. In May 2015, for example, the reduction of the biases was 87%. For November 2016 to April 2017, the reduction of the biases was more noticeable. In April 2017, for example, we found a reduction of the biases of about 70%. Stable winds in the period might be associated with the improvement of the biases (see Supplementary; Fig. S37). In general, all the negative large posterior biases for all the months (2−5ppm approximately) are associated with the strong westerly and north-westerly winds that come from the ocean to Tasmania. As mentioned before,

Cape Grim is a coastal station whose aim is to record clean air that blows from the southern ocean, and it is not representative of Tasmania's air mass.

455    A poor fit between the posterior concentrations and surface sites raises doubts about the reliability of the OCO-2 assimilated fluxes estimated over warm temperate, tropics, and cool temperate ecosystems. Therefore, in the upcoming section, we assess the analysis of the variability of the posterior fluxes only over the savanna and sparsely ecosystems, where our posterior carbon fluxes derived by OCO-2 data are likely more trustworthy than fluxes assimilated over areas directly impacted by off-shore ocean fluxes.
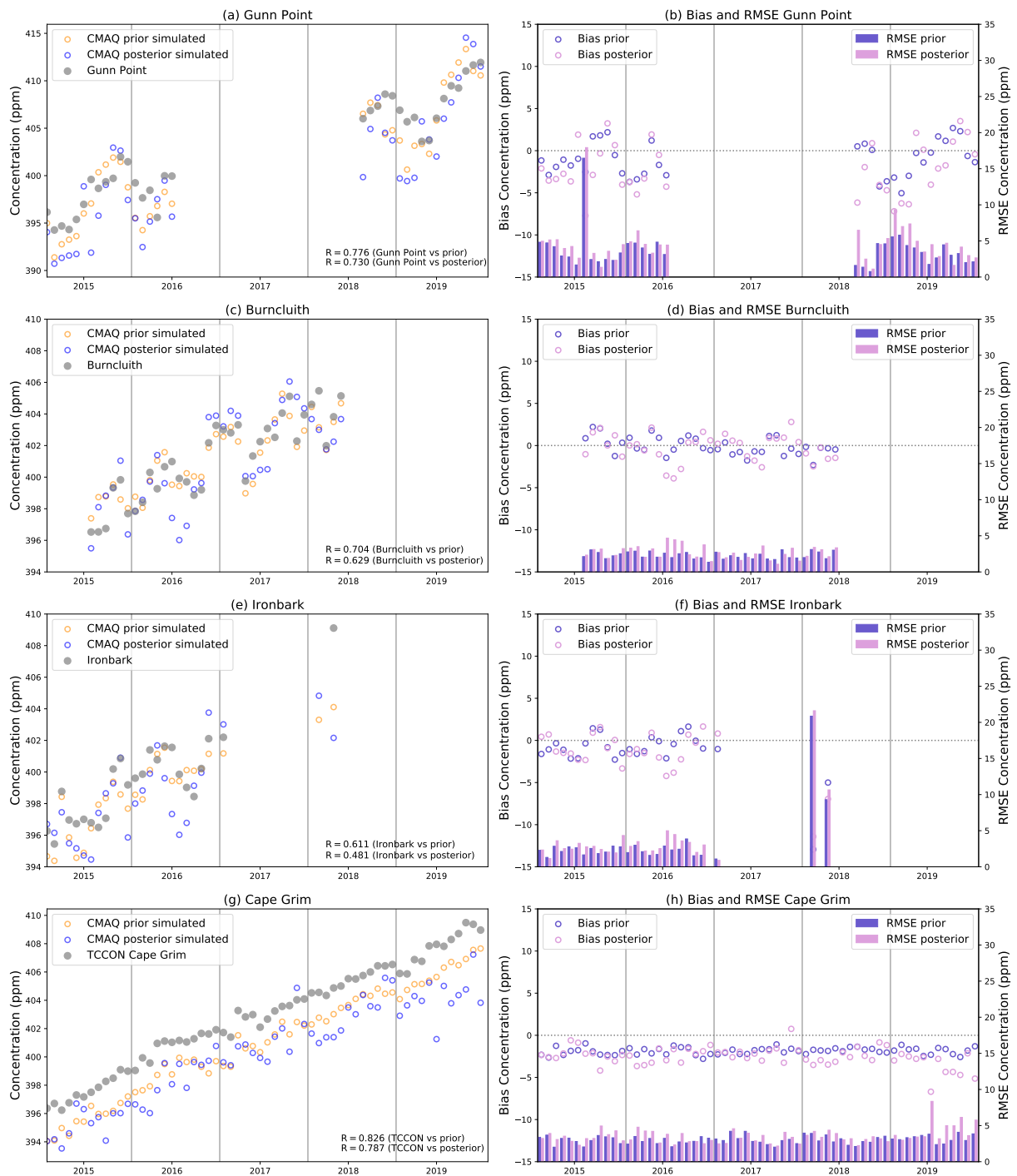
**Figure 8.** Comparison between monthly mean $CO_2$ concentrations (ground-based stations) at (a) Gunn point, (c) Burncluith, (e) Ironbark and (g) Cape Grim sites and the CMAQ prior and posterior modeled $CO_2$ concentrations for 2015–2019. Bias and root mean square error (RMSE) between model and observations are shown in panels b, d, f and h. purple and violet circles represent prior posterior concentration biases, and purple and bar represent the RMSE

## 3.5 Australia's carbon flux anomalies

Fig 9a, and b illustrate 3-month running mean of the prior, posterior flux anomalies and 3-month running means of EVI, rainfall and air temperature anomalies for the period 2015 to 2019 aggregated over sparsely vegetated and savanna ecosystems, and Fig. 10 shows the spatial distribution pattern of the annual anomalies of the posterior flux estimate in the period 2015 to 2019.

It is clear that the anomalous prior and posterior carbon land sink recorded over the sparsely vegetated ecosystem from August 2016 to April 2017 is likely due to a combination of a higher than average increase in land productivity (positive EVI anomalies), rainfall (positive rainfall anomalies) and a lower than average decrease in air temperature (negative temperature anomalies). It is also evident that the strong carbon release (positive carbon flux anomalies) recorded after April 2017 are due to a lower than average greenness of the vegetation (negative EVI anomalies), rainfall (negative rainfall anomalies), and an increase in the air temperature (positive temperature anomalies). In this ecoregion, we found that the temporal correlation between EVI anomalies and the carbon flux anomalies is in better agreement with the posterior (R= -0.5) than the prior anomalies (R= -0.32). Posterior and EVI correlation become even more stronger when we see them at each grid-point Fig. 11b (R = 0.5–0.9). Spatial averaging smooths grid point anomalies and so dilutes signals. The spatial distribution of correlations between rainfall anomalies (Fig. 11d), temperature anomalies (Fig. 11f) and posterior carbon anomalies also improved in some areas in this large ecosystem.

Similar to the sparsely vegetated findings, we also see a higher than average increase in land productivity (positive EVI anomalies), rainfall, and a decrease in air temperature recorded from August 2016 to April 2017 over the savanna ecosystem. But, unlike sparsely vegetated results, the carbon sink anomaly only coincides with the negative posterior carbon anomaly in 2016. In 2017, we see that the positive EVI, rainfall and negative anomalies recorded from January to April do not align with the larger than average posterior carbon release in this period. We believe that the few OCO-2 soundings found in this period limit the potential of our inversion to constrain the surface fluxes in the savanna ecosystem (see Supplementary, Fig.S2, panels a, b and c). We found similar results in September and November 2017. As mentioned in Section 3.1, there was a long data outage of 51 days from August to September 2017. In September, the number of OCO-2 observations in Australia was only 221, and most of the soundings were seen over sparsely vegetated (in central Australia) than the savanna ecosystem (see Supplementary, Fig.S2, panels h, i). In 2019, we also see that a lower than average land productivity, in combination with a deficit of rainfall and an increase in temperature, led to a stronger carbon release into the atmosphere. In this category, the temporal correlation between the posterior anomalies and EVI anomalies was moderate (R= -0.38) compared to the prior flux anomalies and EVI anomalies (R = -0.52). We note that the time series temporal correlation between EVI anomalies and posterior anomalies at grid-cell scale resolution (Fig. 11a) is slightly stronger for the prior than the posterior correlations (Fig. 11b). Similar results were found between the link of the rainfall and posterior flux anomalies, where the correlation tends to degrade compared to the prior. Spatial correlation between temperature anomalies and posterior correlation is more variable, and we see that in the north-west area of the continent, correlations for the posterior flux anomalies are stronger.

In general, the better agreement between posterior, climate and vegetation parameters over regions with sparse vegetation is because the CABLE model likely underestimates GPP anomalies. We found that the correlation between the posterior

anomalies and CABLE BIOS3, DIFFUSE and MODIS GPP anomalies was stronger than the one correlated with the prior. For example, the correlations between the prior and CABLE BIOS3 GPP anomalies were -0.46 compared to the posterior (R = -0.61). Correlations between the posterior anomalies and DIFFUSE and MODIS GPP were also stronger than the prior, which value was -0.5 compared to the prior (R = -0.3) (more details in Appendix D, Table D2). These findings are significant for Australia because they suggest that our OCO-2 inversion might likely be better at capturing the anomalies of this ecosystem (the largest ecosystem in Australia) compared to the biosphere land model.
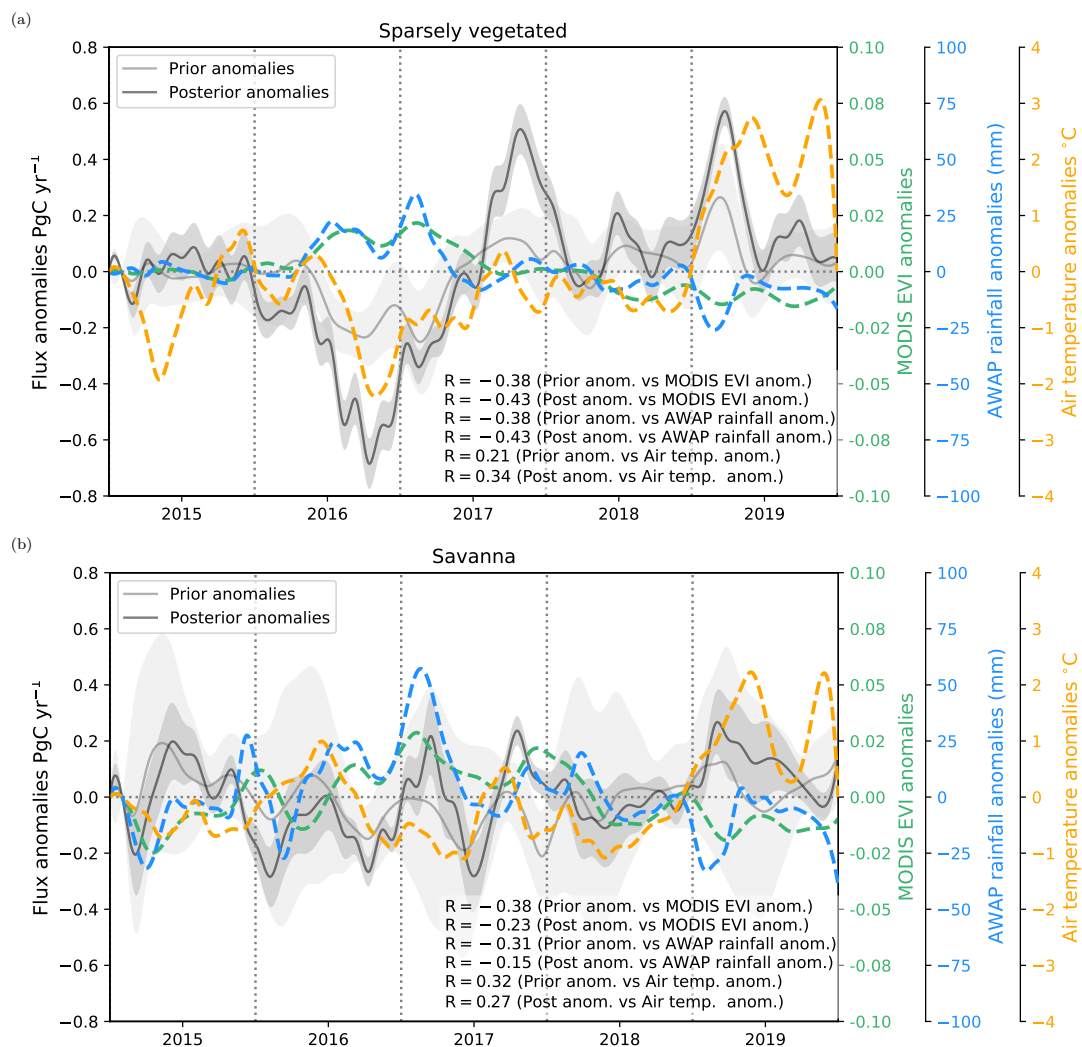
**Figure 9.** Time series of 3-month running mean posterior (black line) and prior (grey line) terrestrial carbon flux anomalies (PgC yr$^{-1}$) and 3-month running mean EVI anomalies (turquoise dashed line) between 2015 to 2019 aggregated by two agro-climate regions: (a) Sparsely vegetated and (b) Savanna ecosystem. Anomalies over Tropics, Warm temperate, Cool temperate, and Mediterranean ecosystems are shown in Appendix D, Fig. D1. The grey shaded area represents 1.0 standard deviation range around the mean for the prior and posterior flux uncertainty.
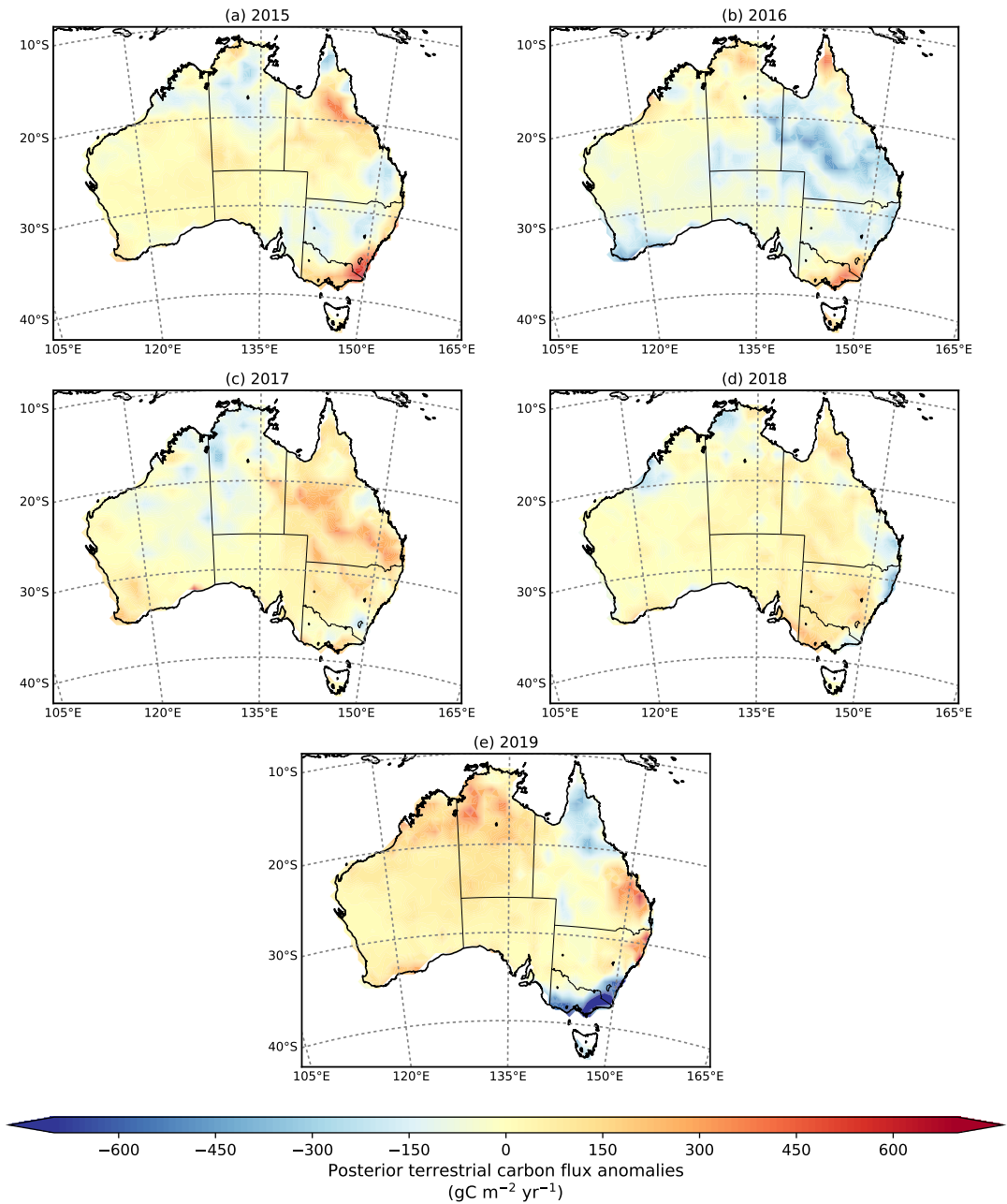
**Figure 10.** Spatial distribution maps of the annual posterior terrestrial carbon flux anomalies (gC m$^{-2}$ yr$^{-1}$) for 2015 to 2019 (panels a, b, c, d and e). Negatives anomalies correspond to a larger than average uptake of carbon by land ecosystem, whereas positives anomalies correspond to a larger than average release of carbon to the atmosphere from the land.
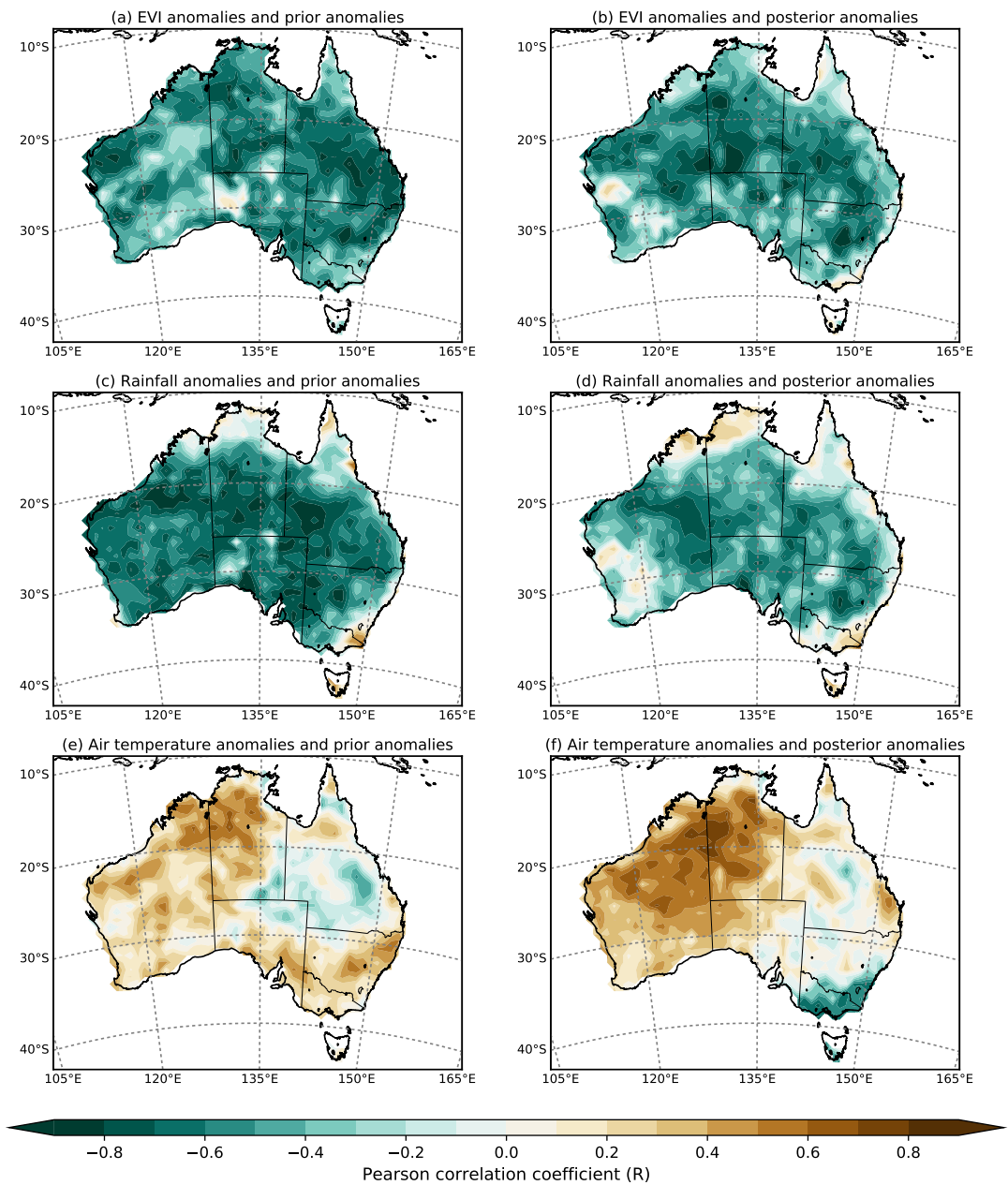
**Figure 11.** Spatial map of monthly temporal correlation between (a, b) EVI anomalies, prior anomalies and posterior anomalies. (c, d) rainfall anomalies, prior and posterior anomalies. (e, c) air temperature anomalies, prior and posterior anomalies for the period 2015–2019.

## 4 Discussion

In Sect 3.4, we saw that validating the posterior concentrations against the current Australian GHG monitoring system is challenging due to the small number of stations across the continent (approximately five). In addition, some of these sites, such as Cape Grim, provide no meaningful constraint on Australian fluxes and therefore leave the question of accuracy in the posterior carbon fluxes unanswered over the savanna and sparsely vegetated regions, where our inversion suggests a stronger carbon sink for the study period compared to the prior estimate made by the biosphere model.

To assess and discuss how well our monthly assimilated OCO-2 carbon fluxes align the current understanding of the Australian carbon cycle, we compare our results to other global products: MIP OCO-2 global inversions (AMES, PCTM, CAMS, CMS-Flux, CSU, CT, OU, TM5−4DVAR, UT), and FLUXCOM for 2015-2018 (Fig. 12). The annual MIP OCO-2 ensemble mean of carbon fluxes shown in Fig. 12 suggests that Australia was a carbon sink of -0.26 $\pm$ 0.22 for 2015–2018, similar to our posterior flux estimate (-0.52 $\pm$ 0.08 PgC yr$^{-1}$) considering the MIP ensemble spread of the nine models as representing the uncertainty. The annual FLUXCOM ensemble mean also suggests that Australia was a slight carbon sink of -0.06 $\pm$ 0.04. In terms of seasonality, we can observe in Fig. 12 that for several periods between 2015 and 2018, the monthly mean of our posterior carbon fluxes falls within the uncertainties of the OCO-2 MIP ensemble mean, except for some months in winter. For example, we notice that the large carbon sink estimated by our inversion (-2.92 $\pm$ 0.27 PgC yr$^{-1}$) in August 2016 does not fall within the ensemble monthly MIP mean of that period (-1.28 $\pm$ 0.78 PgC yr$^{-1}$). However, the carbon flux estimate derived by PCTM (-2.31 PgC yr$^{-1}$) and CSU (-2.66 PgC yr$^{-1}$) global models shows similar results to our flux estimate. These findings are also found throughout 2015, 2017 and 2018, where our posterior carbon flux estimates closely follow PCTM and CSU seasonal patterns. The seasonality of FLUXCOM agrees with our assimilated fluxes, mostly in summer but not in winter.

We also studied the carbon flux anomalies derived by the OCO-2 MIP, FLUXCOM and compared them with the prior and posterior flux anomalies (3-month running mean) that we have discussed throughout this study (Fig. 13). We see in Fig. 13 that all carbon flux estimates agree that 2016 was the period that Australia recorded the largest carbon uptake relative to the 2015-2018 mean. We saw throughout this study that 2016 was a year that Australia recorded above-average precipitation and low temperatures that certainly drove the increase in vegetation productivity across the country. Similar findings were found by Haverd et al. (2016) in 2011, which results suggest that the variations of carbon fluxes over Australia's semi-arid ecosystems have a direct physiological response of vegetation productivity to water availability fluctuations. Other regional studies made in Africa (e.g., Williams et al., 2008; Archibald et al., 2009; Merbold et al., 2009), also indicate that interannual carbon fluctuations of semi-arid ecosystems largely depend on water availability driven by variations in rainfall between years. Water availability is the most important factor that controls the vegetation productivity of ecosystems across most of Australia, such as grassland and shrub/desert (see Figure 2 in Churkina and Running, 1998).

In terms of the amplitude of carbon flux anomalies, we can see that the prior and the FLUXCOM anomalies exhibit a lower amplitude than the one derived by our inversion and the majority of the models in MIP. Australia FLUXCOM estimates are likely not a good representation of the carbon flux estimates in the continent, given the sparsity of the flux tower network. FLUXCOM carbon fluxes use machine learning methods to empirically upscale flux tower data. In Australia, the number of

OzFlux networks is small (approximately 30 towers), where most of the flux towers are located far away from semi-arid/arid ecosystems. This is relevant for Australia because semi-arid/arid ecosystems represent about 70% of the Australian land.

Related to MIP OCO-2 global inversions, we observe that during the year 2016, five global inversions (PCTM, CMS-Flux, CT, OU and UT) agreed with our findings and suggested October as the month of peak uptake. The ensemble mean of FLUXCOM also agrees with our results (-0.42 PgC yr$^{-1}$), however, the size of the uptake is half of our estimates (-1.12 PgC yr$^{-1}$). In terms of the peak of carbon release, there is no agreement between MIP, FLUXCOM, prior and posterior carbon estimates. We observe that almost all OCO-2 MIP inversions agree that the largest outgassing occurred in November 2015. Our inversion places the maximum outgassing in October 2017, while the FLUXCOM and the prior have the maximum outgassing period in October and July 2018, respectively.

The analysis of the inter-annual (peak-to-peak) variability shows that PCTM (3.05 PgC yr$^{-1}$) and CSU (2.46 PgC yr$^{-1}$) produce the largest amplitude of variability compared to our prior (0.70 PgC yr$^{-1}$) and posterior anomalies (1.89 PgC yr$^{-1}$). We also note that UO and AMES exhibit the lowest carbon amplitude of the variability, which values are 1.06 and 1.86 respectively. The disagreement between the global inversion and our study might also be driven by transport differences (Basu et al., 2018; Schuh et al., 2019).

The larger seasonal cycle amplitude of the anomalies suggested by our regional inversion and OCO-2 MIP compared to the flux anomalies derived by the CABLE model and FLUXCOM raises some questions. For example, why do Australia's semi-arid ecosystems capture more carbon dioxide (based on our OCO-2 inversion) than the process-based model estimate? Could it be possible that the larger posterior carbon uptake and its anomalies estimated by the inversion (relative to the prior and FLUXCOM) is because the CABLE model is not well calibrated against the insufficient number of eddy covariance flux towers across the continent? Could the remaining OCO-2 biases in version 9 and potential errors in the transport model be causing deviation from the true flux?. More work needs to be done to reconcile and disentangle what is being found by the inversions and the Australia CABLE model. In future work, we could run this regional inversion using the latest version of OCO-2 data (version 10) in combination with ocean glint data, for which recent verifications confirm reductions in both the bias and standard deviation compared to the TCCON data (OCO-2 Data Quality Statement, 2020). Another direction for future work would be to explore the impact of transport model errors on the resulting assimilated OCO-2 fluxes. Such assessment could be done by choosing, for example, different planetary boundary schemes within the CMAQ model. As mentioned in section 3.4.2, a misrepresentation of vertical mixing near the surface in atmospheric transport models leads to uncertainties in modelled $CO_2$ mixing ratios. Mixing within the planetary boundary layer influences the redistribution of the surface fluxes to the atmospheric column. Another way to evaluate the transport error of the model would be through a model inter-comparison. This approach is well-known in the global inversion TransCom group community (Law et al., 2008; Peylin et al., 2013; Basu et al., 2018), the recent model inter-comparison project (MIP) organized by the OCO-2 Science Team (Crowell et al., 2019; Peiro et al., 2021), and the recent European atmospheric transport inversion comparison (EUROCOM) project (Monteil et al., 2020).

Finally, we could say that previous inversion studies over Australia have been limited by the lack of in situ data. The OCO-2 data certainly allows a quantum leap in resolution, but this is still reasonably coarse, especially when one remembers that the

prior covariance structures we use impose smooth variations up to the correlation length of 500 km. Instruments with scanning

570 geometries which allow higher resolution observations, such as OCO-3 (Eldering et al., 2019) may improve significantly the available resolution of fluxes. This is particularly important when assessing the roles of drivers such as rainfall which may vary on smaller scales. We also note that continuing improvement in the OCO retrievals themselves should allow joint assimilation of land and ocean measurements, hopefully improving the visibility of coastal fluxes and improving comparison with coastal in situ measurements such as Cape grim and Gunn Point, as shown by Villalobos et al. (2021).
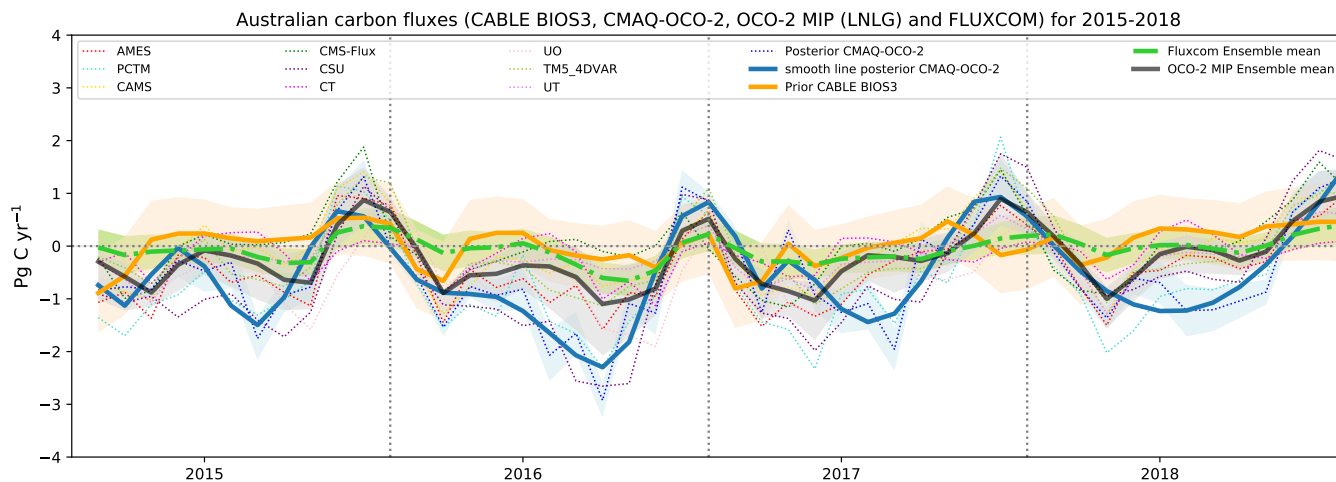
**Figure 12.** Comparison between monthly mean posterior (blue line), prior (orange line), FLUXCOM ensemble mean (green line), MIP OCO-2 ensemble (black line) carbon fluxes and the monthly carbon fluxes from the nine models that participate in OCO-2 MIP: AMES, PCTM, CAMS, CMS-Flux, CSU, CT, OU, TM5−4DVAR, UT (units: PgC yr$^{-1}$).
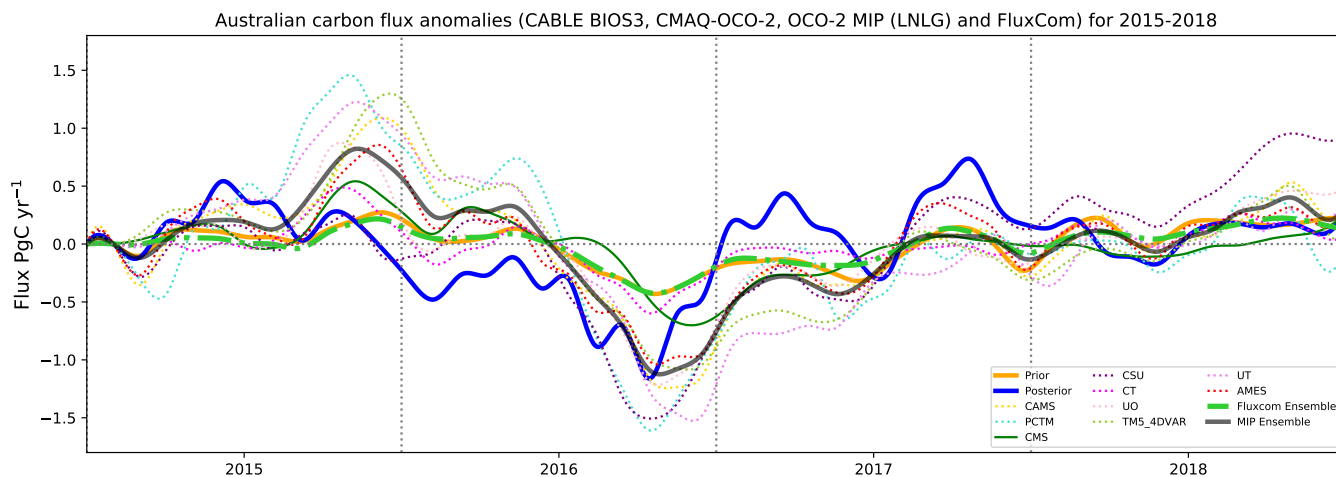
**Figure 13.** Comparison between 3-month running mean posterior (black line), prior (grey orange), FLUXCOM ensemble, OCO-2 MIP ensemble carbon flux anomalies and 3-month running mean anomalies of the nine models that participate in OCO-2 MIP.

**Table 3.** Summary of the peak-to-peak amplitude of 3-month running mean posterior (black line) and prior (grey line) terrestrial carbon flux anomalies and 3-month running mean anomalies of nine different global transport models (Units PgC yr$^{-1}$).

| Carbon flux estimates | Models | Maximun | Date | Minimun | Date | Amplitud |
|---|---|---|---|---|---|---|
| CMAQ-OCO-2 inversion | Posterior | 0.73 | 2017-10-31 | -1.16 | 2016-10-31 | 1.89 |
| BIOS-CABLE3 | Prior | 0.20 | 2018-07-31 | -0.50 | 2016-11-30 | 0.70 |
| MIP OCO-2 | AMES | 0.85 | 2015-12-31 | -1.01 | 2016-10-31 | 1.86 |
| | PCTM | 1.44 | 2015-11-30 | -1.61 | 2016-10-31 | 3.05 |
| | CAMS | 1.09 | 2015-12-31 | -1.23 | 2016-11-30 | 2.33 |
| | CMS-Flux | 0.54 | 2015-11-30 | -0.68 | 2016-12-31 | 1.23 |
| | CSU | 0.95 | 2018-10-31 | -1.51 | 2016-10-31 | 2.46 |
| | CT | 0.46 | 2015-11-30 | -0.60 | 2016-10-31 | 1.06 |
| | OU | 0.83 | 2015-11-30 | -0.60 | 2016-10-31 | 1.43 |
| | TM5-4DVAR | 1.28 | 2015-12-31 | -1.19 | 2016-11-30 | 2.47 |
| | UT | 1.23 | 2015-11-30 | -1.07 | 2016-12-31 | 2.30 |
| MIP OCO-2 | Ensemble | 0.82 | 2015-11-30 | -1.09 | 2016-10-31 | 1.91 |
| FluxCom | Ensemble | 0.22 | 2018-10-31 | -0.42 | 2016-10-31 | 0.64 |

# 5 Conclusions

We estimated monthly carbon fluxes over Australia for 2015 to 2019, based on the assimilation of the Orbiting Carbon Observatory-2 (OCO-2) satellite data (land nadir and glint data, version 9). We investigated the effect of vegetation productivity (EVI anomalies as proxy) and climate driver variations such as rainfall and air temperature on the Australian terrestrial carbon flux variability. The mean of our five-year inversion suggests that Australia was a carbon sink of -0.46 $\pm$ 0.08 PgC yr$^{-1}$ driven partly by large carbon uptake (-1.04 PgC yr$^{-1}$) recorded in 2016 over the savanna and sparsely vegetated ecosystems. We found that negative carbon flux anomalies recorded in this period over these ecosystems coincide with an increase in the vegetation greenness (positive EVI anomalies) driven by higher than average rainfall anomalies and lower than average air temperature anomalies. The 2017 sink over Australia also contributed to the 2015–2019 long term mean, but its contribution was not as significant as 2015 and 2016. Negative carbon flux anomalies recorded in 2017 also coincided with positive rainfall anomalies and temperatures below average in that period over areas with sparse vegetation. In 2018 we did not find significant terrestrial flux anomalies across Australia, and 2019 mainly was affected by positive carbon flux anomalies, which also were in line with a deficit of rainfall and positive temperature anomalies.

Regarding validation of our inversion with independent data, we found it challenging to validate our posterior column-averaged concentration with the current Australian monitoring sites. Despite the fact that for several periods between 2015-2019, the posterior concentration biases at the TCCON monitoring site were less than 1.0 ppm, OCO-2 data was not able to reduce prior biases significantly. We associate this slight or no improvement with the fact that these monitoring stations are strongly affected by ocean fluxes, where no OCO-2 data was considered. Similar findings were found for in-situ measurements at coastal sites such as Cape Grim and Gunn Point. Despite the weak comparison with independent monitoring data, the comparison to OCO-2 MIP global inversion for 2015-2018 and the FLUXCOM ensemble mean present similar results to our regional inversion, suggesting that the year 2016 was a period in which Australia acted as a strong carbon sink of $CO_2$.

## Appendix A: Histograms: CMAQ model and OCO-2 differences
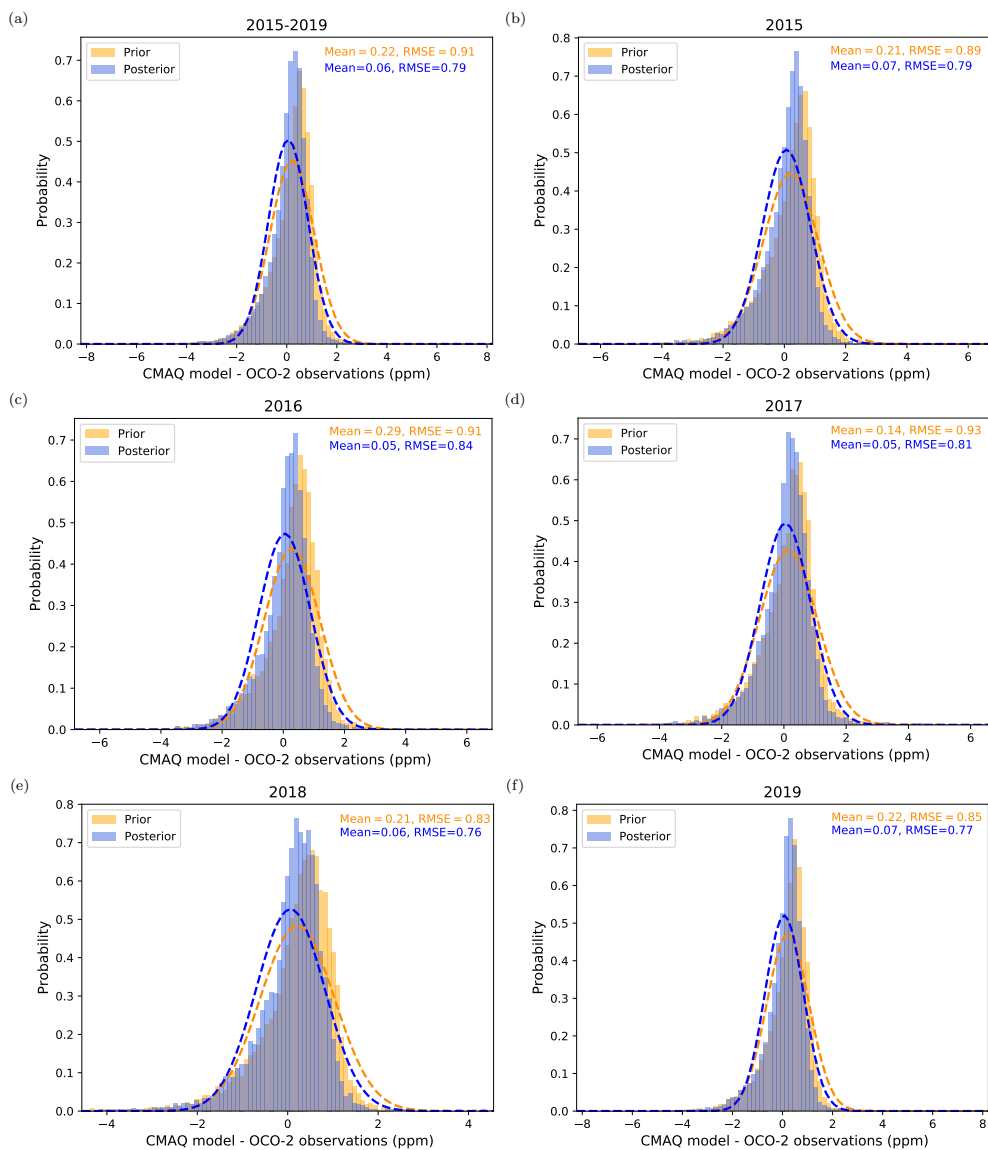
**Figure A1.** Probability density distribution of the difference between CMAQ column average $CO_2$ concentration and OCO-2 observations (Units: ppm). The orange histogram presents the prior CMAQ column average simulated minus OCO-2, whereas the blue histogram presents the posterior column average simulated minus the OCO-2. Mean differences and RMSE are indicated in the legend.
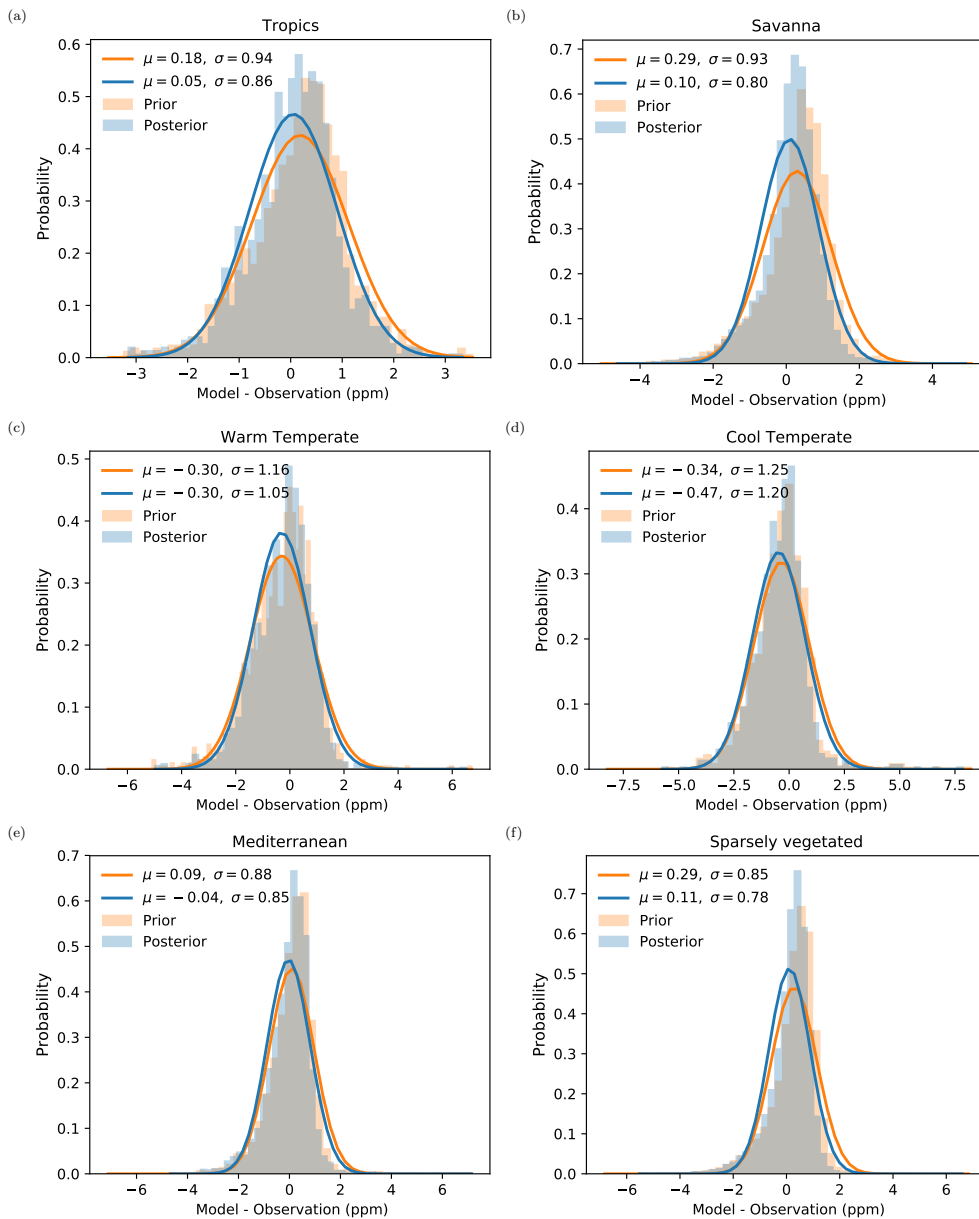
**Figure A2.** Probability density distribution of the difference between CMAQ column average $CO_2$ concentration and OCO-2 observations aggregated by six bioclimatic classifications (Units: ppm). The orange histogram presents the prior CMAQ column average simulated minus OCO-2, whereas the blue histogram presents the posterior column average simulated minus the OCO-2. Mean differences and RMSE are indicated in the legend.

# Appendix B: Spatial distribution of the prior and posterior annual mean (2015-2019)
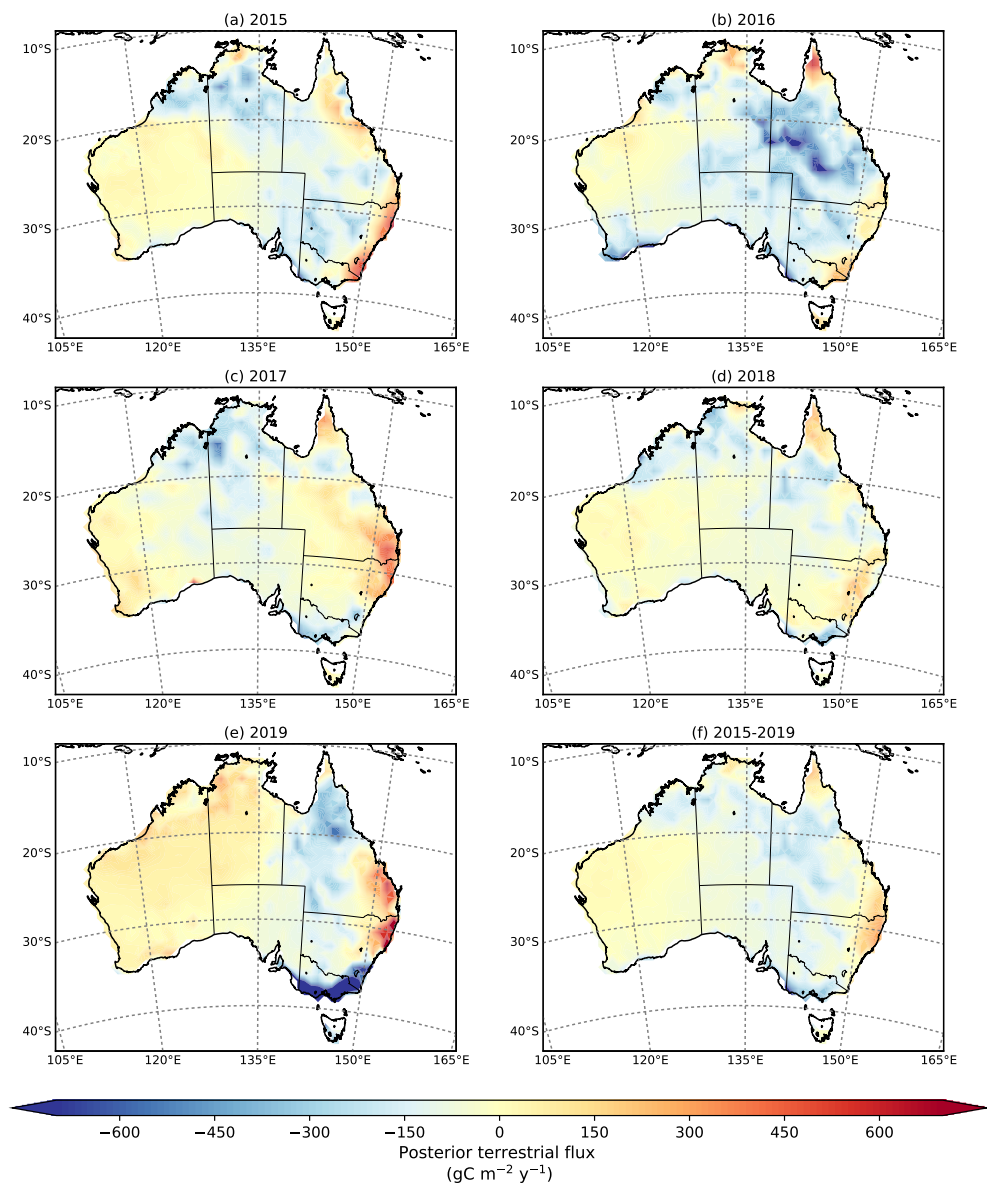
**Figure B1.** Posterior fluxes assimilated using LNLG OCO-2 satellite observations averaged for 2015 – 2019 (fossil fuel emissions are excluded).
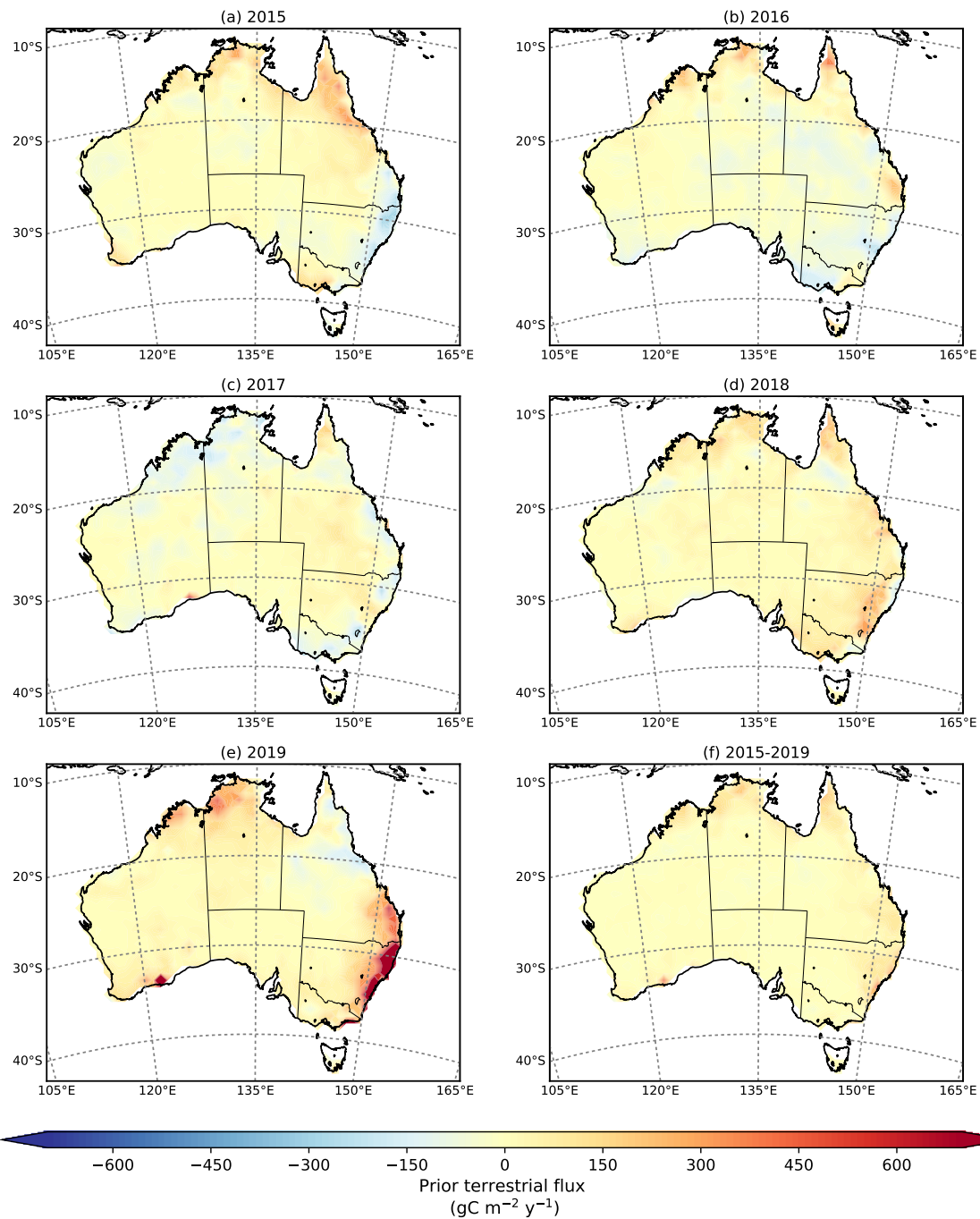
**Figure B2.** Prior fluxes derived by the CABLE model in the BIOS3 set-up in combination with fires emissions selected by GFED averaged for 2015–2019 (Fossil fuel emissions are excluded).

# Appendix C:  Climatological seasonal cycle and GPP anomalies (2015–2019)
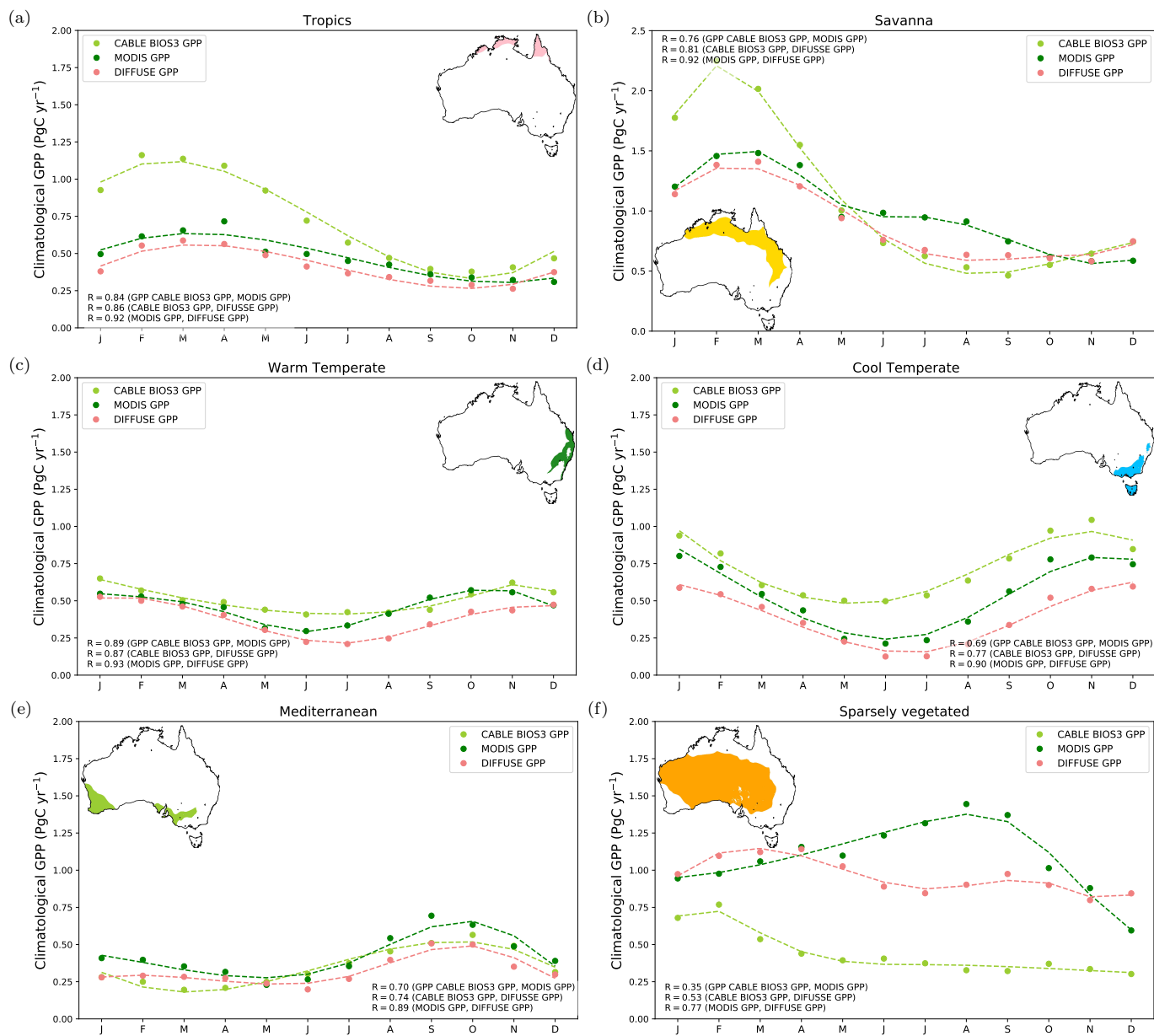
**Figure C1.** Climatological seasonal cycle of GPP (2015–2019) derived from CABLE BIOS3 model (yellow-green dashed line), MODIS (forest-green dashed line), and DIFFUSE model (lightcoral dashed line).
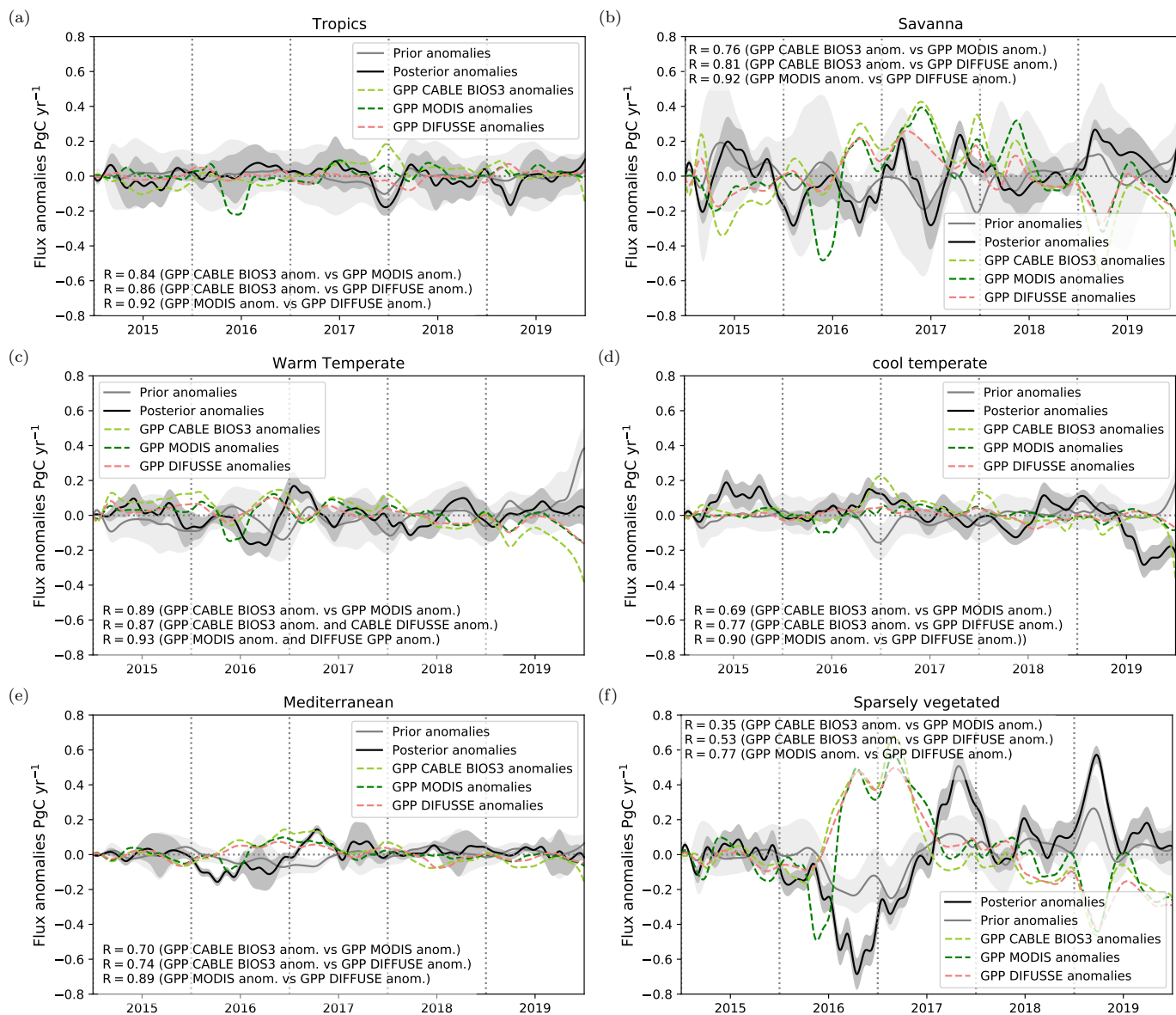
**Figure C2.** Time series of 3-running monthly mean GPP anomalies derived from CABLE BIOS3 model (yellow-green dashed line), MODIS (forest-green dashed line), and DIFFUSE model (orange dashed line) between 2015 and 2019.

## Appendix D: Carbon flux anomalies aggregated by bio-climatic regions
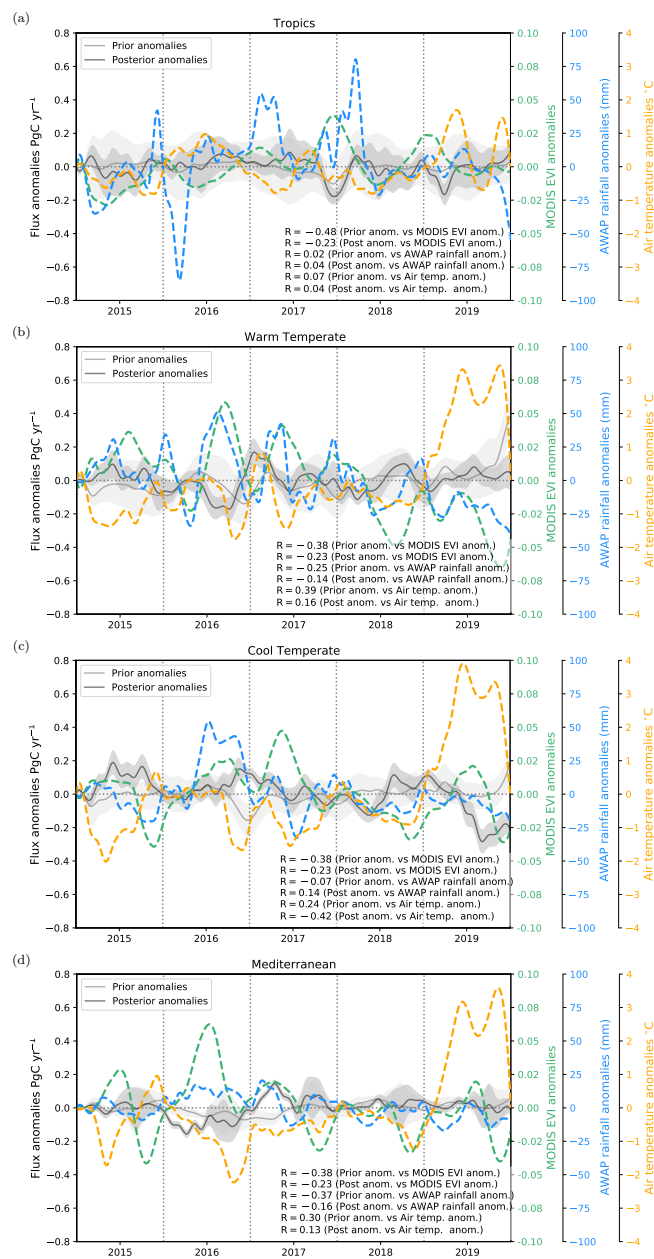
**Figure D1.** Time series of 3-month running mean posterior (black line) and prior (grey line) terrestrial $CO_2$ flux anomalies (PgC $yr^{-1}$) and 3-month running mean EVI anomalies (turquoise dashed line) between 2015 to 2019 aggregated by four agro-climate regions: (a) Tropics, (b) warm temperate, (c) Cool temperate, and (d) Mediterranean ecosystems. The grey shaded area represent 1.0 standard deviation range around the mean for the prior and posterior flux uncertainty.
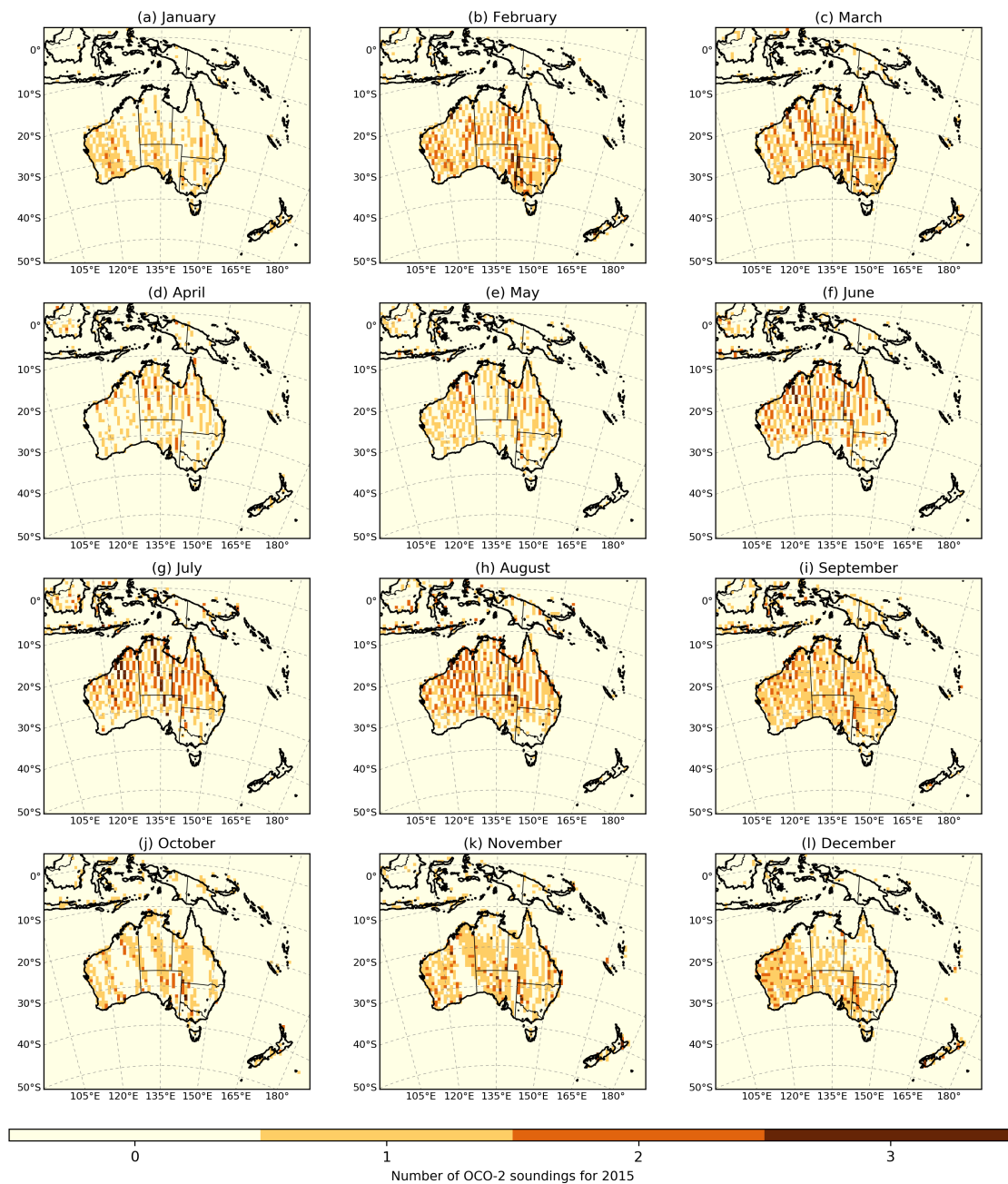
**Figure E1.** Spatial distribution of OCO-2 soundings (Land nadir and glint data) over the CMAQ domain for 2015.

# Appendix F: Analysis of the residual TCCON

**Table F1.** Analysis of the residual between CMAQ prior and posterior simulation and TCCON Darwin site for 2015–2019. Averaged bias (Bias), Root-mean-square error (RMSE) and Pearson's coefficient (R).

| | | Darwin | | | | | | | | | | | | | | | | | | | |
|---|---|---|---|---|---|---|---|---|---|---|---|---|---|---|---|---|---|---|---|---|---|
| months | Prior | | | Posterior | | | months | Prior | | | Posterior | | | months | Prior | | | Posterior | | |
| yyyy-mm | Bias | RMSE | R | Bias | RMSE | R | yyyy-mm | Bias | RMSE | R | Bias | RMSE | R | yyyy-mm | Bias | RMSE | R | Bias | RMSE | R |
| 2015-01 | 0.12 | 0.51 | 0.81 | -0.04 | 0.82 | 0.75 | 2017-01 | - | - | - | - | - | - | 2019-01 | - | - | - | - | - | - |
| 2015-02 | 0.69 | 0.85 | 0.78 | 0.38 | 0.63 | 0.78 | 2017-02 | - | - | - | - | - | - | 2019-02 | -1.31 | 1.34 | -0.49 | -1.40 | 1.43 | -0.61 |
| 2015-03 | 0.93 | 1.10 | 0.14 | 0.18 | 0.59 | 0.29 | 2017-03 | 0.32 | 0.58 | 0.60 | -1.34 | 1.45 | 0.59 | 2019-03 | -0.78 | 0.87 | 0.60 | -1.42 | 1.55 | 0.39 |
| 2015-04 | 0.85 | 0.94 | 0.38 | 0.60 | 0.74 | 0.42 | 2017-04 | - | - | - | - | - | - | 2019-04 | - | - | - | - | - | - |
| 2015-05 | 0.97 | 1.05 | 0.37 | 0.90 | 0.99 | 0.52 | 2017-05 | - | - | - | - | - | - | 2019-05 | - | - | - | - | - | - |
| 2015-06 | 0.90 | 0.97 | 0.21 | 1.24 | 1.27 | 0.23 | 2017-06 | -0.12 | 0.44 | -0.02 | 0.24 | 0.46 | 0.25 | 2019-06 | - | - | - | - | - | - |
| 2015-07 | 1.51 | 1.55 | -0.18 | 1.07 | 1.10 | 0.22 | 2017-07 | -0.13 | 0.74 | 0.07 | 0.04 | 0.69 | 0.16 | 2019-07 | - | - | - | - | - | - |
| 2015-08 | 1.44 | 1.46 | 0.34 | 1.06 | 1.10 | 0.35 | 2017-08 | 0.19 | 0.39 | 0.09 | 0.28 | 0.49 | 0.15 | 2019-08 | - | - | - | - | - | - |
| 2015-09 | 1.12 | 1.16 | 0.02 | 0.81 | 0.86 | 0.10 | 2017-09 | -0.15 | 0.32 | 0.14 | -0.16 | 0.31 | 0.13 | 2019-09 | -0.30 | 0.66 | 0.25 | -0.40 | 0.73 | 0.18 |
| 2015-10 | 0.55 | 0.63 | 0.53 | 0.63 | 0.69 | 0.62 | 2017-10 | -0.92 | 1.05 | 0.42 | -0.51 | 0.72 | 0.46 | 2019-10 | -0.91 | 1.01 | 0.72 | -0.87 | 0.95 | 0.78 |
| 2015-11 | -0.25 | 0.51 | 0.66 | 0.11 | 0.42 | 0.75 | 2017-11 | -1.12 | 1.21 | 0.06 | -0.76 | 0.99 | -0.20 | 2019-11 | -1.31 | 1.37 | 0.70 | -0.96 | 1.06 | 0.61 |
| 2015-12 | -0.34 | 0.48 | 0.18 | -0.02 | 0.31 | 0.26 | 2017-12 | -0.67 | 0.79 | 0.37 | -0.74 | 0.97 | 0.26 | 2019-12 | -1.37 | 1.43 | 0.35 | -1.22 | 1.32 | 0.26 |
| 2016-01 | 0.27 | 0.55 | 0.39 | 0.09 | 0.60 | 0.28 | 2018-01 | -0.57 | 0.85 | 0.08 | -1.15 | 1.30 | -0.08 | | | | | | | |
| 2016-02 | 0.34 | 0.63 | 0.34 | -0.25 | 0.66 | 0.29 | 2018-02 | -0.90 | 1.04 | 0.08 | -1.98 | 2.11 | -0.13 | | | | | | | |
| 2016-03 | 0.44 | 0.63 | 0.36 | -0.09 | 0.58 | 0.30 | 2018-03 | -0.62 | 1.06 | -0.65 | -1.46 | 1.67 | -0.59 | | | | | | | |
| 2016-04 | 0.80 | 0.93 | 0.34 | 0.86 | 0.95 | 0.48 | 2018-04 | - | - | - | - | - | - | | | | | | | |
| 2016-05 | 0.26 | 0.41 | 0.58 | 0.41 | 0.53 | 0.54 | 2018-05 | - | - | - | - | - | - | | | | | | | |
| 2016-06 | 0.37 | 0.45 | 0.16 | 0.21 | 0.38 | 0.18 | 2018-06 | -0.27 | 0.51 | -0.08 | -0.09 | 0.40 | 0.22 | | | | | | | |
| 2016-07 | 0.18 | 0.42 | 0.17 | 0.07 | 0.38 | 0.34 | 2018-07 | -0.34 | 0.52 | -0.16 | -0.34 | 0.48 | 0.04 | | | | | | | |
| 2016-08 | 0.09 | 0.33 | 0.04 | -0.07 | 0.33 | 0.27 | 2018-08 | -0.34 | 0.49 | 0.05 | -0.94 | 0.99 | 0.07 | | | | | | | |
| 2016-09 | -0.17 | 0.40 | 0.25 | -0.20 | 0.40 | 0.26 | 2018-09 | -0.57 | 0.69 | 0.09 | -0.90 | 0.99 | 0.09 | | | | | | | |
| 2016-10 | -0.31 | 0.42 | 0.01 | -0.30 | 0.47 | 0.27 | 2018-10 | - | - | - | - | - | - | | | | | | | |
| 2016-11 | -0.40 | 0.42 | 0.75 | -0.43 | 0.47 | 0.67 | 2018-11 | - | - | - | - | - | - | | | | | | | |
| 2016-12 | - | - | - | - | - | - | 2018-12 | - | - | - | - | - | - | | | | | | | |

**Table F2.** Analysis of the residual between CMAQ prior and posterior simulation and TCCON Lauder site for 2015–2019. Averaged bias (Bias), Root-mean-square error (RMSE) and Pearson's coefficient (R).

| | | | | | | | Lauder | | | | | | | | | | | | | | |
|---|---|---|---|---|---|---|---|---|---|---|---|---|---|---|---|---|---|---|---|---|---|
| Months | Prior | | | Posterior | | | Months | Prior | | | Posterior | | | Months | Prior | | | Posterior | | |
| yyyy-mm | Bias | RMSE | R | Bias | RMSE | R | yyyy-mm | Bias | RMSE | R | Bias | RMSE | R | yyyy-mm | Bias | RMSE | R | Bias | RMSE | R |
| 2015-01 | 0.48 | 0.58 | 0.31 | 0.71 | 0.85 | 0.06 | 2017-01 | 0.571 | 0.71 | 0.39 | 0.60 | 0.79 | 0.39 | 2019-01 | 0.89 | 1.01 | 0.53 | 1.10 | 1.38 | 0.55 |
| 2015-02 | 0.61 | 0.74 | 0.22 | 1.03 | 1.17 | 0.34 | 2017-02 | 0.187 | 0.41 | 0.24 | 0.65 | 1.03 | 0.07 | 2019-02 | 0.94 | 1.02 | 0.21 | 1.10 | 1.40 | 0.12 |
| 2015-03 | 0.54 | 0.62 | 0.51 | 0.73 | 0.84 | 0.53 | 2017-03 | 0.16 | 0.41 | 0.35 | 0.27 | 0.48 | 0.35 | 2019-03 | 0.64 | 0.75 | 0.53 | 0.95 | 1.25 | 0.69 |
| 2015-04 | 0.50 | 0.59 | 0.77 | 0.51 | 0.60 | 0.79 | 2017-04 | 0.35 | 0.52 | 0.22 | 0.20 | 0.32 | 0.21 | 2019-04 | 0.83 | 0.88 | 0.58 | 0.80 | 0.94 | 0.54 |
| 2015-05 | 0.82 | 0.89 | 0.30 | 0.83 | 0.90 | 0.23 | 2017-05 | 0.191 | 0.40 | 0.54 | 0.16 | 0.24 | 0.59 | 2019-05 | 0.73 | 0.81 | 0.65 | 0.62 | 0.75 | 0.67 |
| 2015-06 | 0.65 | 0.86 | 0.60 | 0.61 | 0.82 | 0.56 | 2017-06 | 0.44 | 0.58 | 0.77 | 0.32 | 0.46 | 0.76 | 2019-06 | 0.63 | 0.76 | 0.85 | 0.46 | 0.68 | 0.82 |
| 2015-07 | 0.69 | 0.82 | 0.79 | 0.64 | 0.79 | 0.76 | 2017-07 | 0.44 | 0.56 | 0.30 | 0.26 | 0.39 | 0.38 | 2019-07 | 0.81 | 0.88 | 0.73 | 0.65 | 0.80 | 0.69 |
| 2015-08 | 0.57 | 0.64 | 0.64 | 0.57 | 0.64 | 0.66 | 2017-08 | 0.71 | 0.81 | 0.64 | 0.63 | 0.87 | 0.63 | 2019-08 | 1.14 | 1.22 | 0.75 | 1.15 | 1.42 | 0.74 |
| 2015-09 | 0.71 | 0.73 | 0.83 | 0.63 | 0.67 | 0.83 | 2017-09 | 1.30 | 1.35 | 0.73 | 1.58 | 1.76 | 0.71 | 2019-09 | 0.96 | 1.07 | 0.60 | 0.97 | 1.24 | 0.63 |
| 2015-10 | 0.75 | 0.82 | 0.65 | 0.74 | 0.82 | 0.59 | 2017-10 | 1.01 | 1.08 | 0.72 | 1.28 | 1.51 | 0.76 | 2019-10 | 1.09 | 1.13 | 0.72 | 1.23 | 1.42 | 0.62 |
| 2015-11 | 0.52 | 0.72 | 0.36 | 0.43 | 0.65 | 0.37 | 2017-11 | 0.74 | 0.90 | 0.50 | 0.79 | 0.97 | 0.50 | 2019-11 | 0.99 | 1.06 | 0.79 | 1.09 | 1.33 | 0.78 |
| 2015-12 | 0.71 | 0.76 | 0.79 | 0.77 | 0.81 | 0.81 | 2017-12 | 0.83 | 0.91 | 0.63 | 1.37 | 1.65 | 0.67 | 2019-12 | 1.03 | 1.10 | 0.70 | 0.82 | 1.11 | 0.52 |
| 2016-01 | 0.43 | 0.51 | 0.81 | 0.40 | 0.51 | 0.78 | 2018-01 | 0.64 | 0.73 | 0.33 | 1.04 | 1.43 | 0.16 | | | | | | | |
| 2016-02 | 0.23 | 0.40 | 0.54 | 0.18 | 0.33 | 0.49 | 2018-02 | 0.52 | 0.61 | 0.62 | 0.46 | 0.62 | 0.63 | | | | | | | |
| 2016-03 | 0.24 | 0.45 | 0.57 | 0.23 | 0.32 | 0.53 | 2018-03 | 0.59 | 0.74 | 0.35 | 0.52 | 0.83 | 0.33 | | | | | | | |
| 2016-04 | 0.17 | 0.45 | 0.72 | 0.19 | 0.25 | 0.71 | 2018-04 | 0.63 | 0.74 | 0.44 | 0.53 | 0.71 | 0.42 | | | | | | | |
| 2016-05 | 0.39 | 0.54 | 0.61 | 0.29 | 0.46 | 0.55 | 2018-05 | 0.91 | 1.04 | 0.40 | 0.99 | 1.46 | 0.39 | | | | | | | |
| 2016-06 | 0.21 | 0.50 | 0.44 | 0.22 | 0.38 | 0.48 | 2018-06 | 0.70 | 0.89 | -0.42 | 0.68 | 0.98 | -0.44 | | | | | | | |
| 2016-07 | 0.59 | 0.78 | 0.74 | 0.58 | 0.82 | 0.74 | 2018-07 | 0.99 | 1.03 | 0.69 | 0.88 | 1.13 | 0.43 | | | | | | | |
| 2016-08 | 0.32 | 0.55 | 0.55 | 0.30 | 0.41 | 0.55 | 2018-08 | 0.75 | 0.79 | 0.77 | 0.60 | 0.72 | 0.78 | | | | | | | |
| 2016-09 | 0.31 | 0.62 | 0.11 | 0.34 | 0.62 | 0.16 | 2018-09 | 0.96 | 1.03 | 0.41 | 0.94 | 1.16 | 0.45 | | | | | | | |
| 2016-10 | 0.30 | 0.55 | 0.10 | 0.58 | 0.75 | 0.37 | 2018-10 | 1.011 | 1.11 | 0.48 | 1.34 | 1.58 | 0.55 | | | | | | | |
| 2016-11 | 0.93 | 0.97 | 0.68 | 1.30 | 1.47 | 0.66 | 2018-11 | 1.25 | 1.30 | 0.63 | 2.10 | 2.31 | 0.65 | | | | | | | |
| 2016-12 | 0.576 | 0.7823 | 0.22 | 1.16 | 1.78 | 0.16 | 2018-12 | 1.35 | 1.40 | 0.33 | 2.897 | 3.15 | 0.33 | | | | | | | |

**Table F3.** Analysis of the residual between CMAQ prior and posterior simulation and TCCON Wollongong site for 2015–2019. Averaged bias (Bias), Root-mean-square error (RMSE) and Pearson's coefficient (R).

| Wollongong | | | | | | | | | | | | | | | | | | | | |
|---|---|---|---|---|---|---|---|---|---|---|---|---|---|---|---|---|---|---|---|---|
| Months | Prior | | | Posterior | | | Months | Prior | | | Posterior | | | Months | Prior | | | Posterior | | |
| yyyy-mm | Bias | RMSE | R | Bias | RMSE | R | yyyy-mm | Bias | RMSE | R | Bias | RMSE | R | yyyy-mm | Bias | RMSE | R | Bias | RMSE | R |
| 2015-01 | -0.04 | 0.72 | 0.21 | 0.07 | 0.75 | 0.23 | 2017-01 | -0.76 | 0.99 | 0.25 | -0.35 | 0.84 | 0.16 | 2019-01 | -2.20 | 2.55 | 0.07 | -2.23 | 2.51 | 0.20 |
| 2015-02 | -0.21 | 0.56 | 0.48 | 0.16 | 0.63 | 0.51 | 2017-02 | -0.79 | 1.08 | 0.37 | -0.82 | 1.13 | 0.14 | 2019-02 | -0.47 | 0.84 | 0.28 | -0.65 | 0.93 | 0.32 |
| 2015-03 | 0.66 | 0.94 | 0.19 | 0.51 | 0.88 | 0.16 | 2017-03 | -0.83 | 1.26 | -0.07 | -0.82 | 1.32 | 0.01 | 2019-03 | -0.33 | 0.65 | 0.48 | -0.51 | 0.78 | 0.45 |
| 2015-04 | 0.72 | 0.96 | 0.07 | 0.82 | 1.06 | 0.15 | 2017-04 | -0.52 | 1.11 | 0.03 | -0.55 | 1.13 | -0.09 | 2019-04 | -0.50 | 0.83 | 0.16 | -0.65 | 0.95 | 0.16 |
| 2015-05 | 1.26 | 1.40 | 0.12 | 1.54 | 1.72 | 0.02 | 2017-05 | -0.42 | 0.66 | 0.31 | -0.50 | 0.74 | 0.26 | 2019-05 | 0.03 | 0.67 | 0.26 | -0.06 | 0.71 | 0.21 |
| 2015-06 | 1.41 | 1.53 | 0.68 | 1.61 | 1.72 | 0.68 | 2017-06 | -0.24 | 0.53 | 0.67 | -0.24 | 0.53 | 0.68 | 2019-06 | 0.20 | 0.75 | 0.17 | -0.14 | 0.60 | 0.40 |
| 2015-07 | 1.37 | 1.56 | 0.32 | 1.14 | 1.38 | 0.28 | 2017-07 | -0.01 | 0.55 | 0.42 | -0.11 | 0.59 | 0.37 | 2019-07 | 0.17 | 0.70 | 0.17 | -0.04 | 0.62 | 0.17 |
| 2015-08 | 1.42 | 1.57 | 0.25 | 1.61 | 1.76 | 0.28 | 2017-08 | 0.17 | 0.89 | -0.19 | 0.16 | 0.91 | -0.19 | 2019-08 | -0.29 | 0.52 | 0.82 | -0.77 | 0.87 | 0.79 |
| 2015-09 | 1.19 | 1.44 | 0.16 | 1.11 | 1.42 | 0.19 | 2017-09 | 0.31 | 0.86 | -0.06 | 0.17 | 0.68 | 0.12 | 2019-09 | -0.05 | 0.67 | -0.10 | -0.67 | 0.98 | -0.18 |
| 2015-10 | 0.07 | 0.72 | 0.03 | 0.29 | 0.83 | 0.00 | 2017-10 | - | - | - | - | - | - | 2019-10 | -0.36 | 0.64 | 0.38 | -0.74 | 0.97 | 0.22 |
| 2015-11 | -0.74 | 1.22 | -0.08 | -0.40 | 1.13 | -0.05 | 2017-11 | - | - | - | - | - | - | 2019-11 | -0.14 | 0.80 | 0.62 | -0.63 | 0.95 | 0.69 |
| 2015-12 | -0.45 | 0.69 | 0.14 | -0.60 | 0.85 | -0.03 | 2017-12 | - | - | - | - | - | - | 2019-12 | 0.99 | 1.77 | 0.67 | -1.31 | 1.44 | 0.69 |
| 2016-01 | -0.29 | 0.51 | 0.58 | -0.19 | 0.42 | 0.50 | 2018-01 | - | - | - | - | - | - | | | | | | | |
| 2016-02 | -0.93 | 1.09 | 0.24 | -1.00 | 1.18 | -0.13 | 2018-02 | - | - | - | - | - | - | | | | | | | |
| 2016-03 | -0.18 | 0.56 | 0.59 | -0.36 | 0.69 | 0.54 | 2018-03 | -0.72 | 0.94 | 0.47 | -0.98 | 1.15 | 0.30 | | | | | | | |
| 2016-04 | 0.10 | 0.69 | -0.20 | 0.07 | 0.57 | -0.19 | 2018-04 | -0.221 | 0.66 | 0.52 | -0.59 | 0.78 | 0.55 | | | | | | | |
| 2016-05 | -0.07 | 0.65 | 0.31 | -0.12 | 0.71 | 0.17 | 2018-05 | -0.011 | 0.59 | 0.20 | -0.17 | 0.58 | 0.11 | | | | | | | |
| 2016-06 | -0.21 | 0.71 | -0.13 | -0.52 | 0.87 | -0.16 | 2018-06 | -0.03 | 0.39 | 0.72 | -0.11 | 0.45 | 0.66 | | | | | | | |
| 2016-07 | 0.04 | 0.66 | 0.52 | -0.05 | 0.71 | 0.49 | 2018-07 | -0.15 | 0.65 | 0.21 | -0.33 | 0.68 | 0.19 | | | | | | | |
| 2016-08 | 0.48 | 0.80 | 0.17 | 0.07 | 0.70 | 0.22 | 2018-08 | 0.08 | 0.51 | 0.42 | 0.23 | 0.57 | 0.37 | | | | | | | |
| 2016-09 | -0.05 | 0.89 | 0.40 | -0.37 | 1.05 | 0.36 | 2018-09 | -0.25 | 0.78 | 0.13 | -0.49 | 0.91 | 0.03 | | | | | | | |
| 2016-10 | -0.14 | 0.78 | 0.17 | -0.16 | 0.86 | 0.16 | 2018-10 | -0.352 | 0.78 | -0.08 | -0.64 | 1.00 | -0.22 | | | | | | | |
| 2016-11 | -0.53 | 0.93 | 0.30 | 0.41 | 0.87 | 0.32 | 2018-11 | -0.808 | 1.05 | 0.64 | -0.29 | 0.93 | 0.52 | | | | | | | |
| 2016-12 | -0.77 | 1.1305 | 0.06 | -0.13 | 0.87 | 0.07 | 2018-12 | -1.10 | 1.31 | 0.66 | -0.81 | 1.10 | 0.75 | | | | | | | |

## Appendix G: Analysis of the residual in-situ data

**Table G1.** Analysis of the residual between CMAQ prior and posterior simulation and Cape Grim site for 2015–2019. Averaged bias (Bias), Root-mean-square error (RMSE) and Pearson's coefficient (R).

| | | | | | | | | | | | | | | | | | | | | | |
|---|---|---|---|---|---|---|---|---|---|---|---|---|---|---|---|---|---|---|---|---|---|
| | | | | | | | | | Cape Grim | | | | | | | | | | | | |
| months | | Prior | | | Posterior | | months | | Prior | | | Posterior | | months | | Prior | | | Posterior | | |
| yyyy-mm | Bias | RMSE | R | Bias | RMSE | R | yyyy-mm | Bias | RMSE | R | Bias | RMSE | R | yyyy-mm | Bias | RMSE | R | Bias | RMSE | R |
| 2015-01 | -2.31 | 3.38 | 0.28 | -2.33 | 3.22 | 0.28 | 2017-01 | -2.27 | 3.15 | 0.01 | -2.04 | 2.48 | 0.59 | 2019-01 | -1.81 | 3.15 | -0.11 | -2.99 | 3.65 | 0.07 |
| 2015-02 | -2.65 | 3.68 | 0.57 | -2.59 | 3.91 | 0.53 | 2017-02 | -2.08 | 2.93 | -0.11 | -1.99 | 2.53 | 0.40 | 2019-02 | -1.13 | 3.06 | -0.14 | -2.22 | 2.98 | 0.31 |
| 2015-03 | -1.25 | 2.02 | 0.53 | -2.70 | 3.07 | 0.29 | 2017-03 | -1.70 | 4.22 | 0.17 | -2.60 | 4.57 | 0.24 | 2019-03 | -1.67 | 3.33 | 0.37 | -2.51 | 3.22 | 0.60 |
| 2015-04 | -2.33 | 3.22 | 0.41 | -2.16 | 3.54 | 0.19 | 2017-04 | -2.23 | 3.21 | 0.58 | -1.95 | 3.25 | 0.45 | 2019-04 | -1.60 | 3.46 | -0.24 | -2.79 | 3.41 | 0.49 |
| 2015-05 | -1.85 | 3.27 | 0.36 | -0.60 | 2.82 | 0.46 | 2017-05 | -2.22 | 4.21 | 0.06 | -2.71 | 3.95 | 0.30 | 2019-05 | -2.46 | 3.64 | 0.22 | -2.60 | 3.46 | 0.46 |
| 2015-06 | -1.77 | 2.79 | 0.14 | -0.88 | 2.28 | 0.20 | 2017-06 | -1.77 | 2.81 | -0.01 | -2.17 | 2.88 | 0.21 | 2019-06 | -2.31 | 3.81 | -0.07 | -6.70 | 8.35 | -0.59 |
| 2015-07 | -0.96 | 2.05 | 0.10 | -2.18 | 3.20 | -0.03 | 2017-07 | -1.64 | 2.71 | -0.06 | -3.01 | 3.65 | 0.30 | 2019-07 | -1.50 | 2.37 | -0.15 | -2.80 | 3.18 | 0.30 |
| 2015-08 | -1.91 | 2.93 | -0.05 | -2.12 | 3.22 | 0.02 | 2017-08 | -1.66 | 2.37 | 0.09 | -1.82 | 2.46 | 0.01 | 2019-08 | -1.64 | 2.45 | -0.17 | -4.35 | 4.98 | 0.21 |
| 2015-09 | -2.29 | 3.63 | -0.02 | -4.18 | 4.94 | 0.16 | 2017-09 | -1.08 | 2.02 | -0.02 | -1.55 | 2.17 | 0.10 | 2019-09 | -2.23 | 2.95 | 0.19 | -4.35 | 4.97 | -0.31 |
| 2015-10 | -2.34 | 3.44 | 0.08 | -2.52 | 3.75 | 0.00 | 2017-10 | -2.03 | 2.93 | 0.03 | -3.26 | 4.07 | -0.14 | 2019-10 | -2.58 | 4.07 | 0.13 | -4.71 | 6.14 | -0.18 |
| 2015-11 | -2.35 | 3.32 | 0.34 | -3.07 | 4.28 | -0.06 | 2017-11 | -1.60 | 3.09 | 0.09 | 0.76 | 3.38 | 0.52 | 2019-11 | -1.81 | 2.94 | 0.52 | -2.14 | 3.61 | -0.05 |
| 2015-12 | -1.86 | 2.51 | 0.58 | -2.34 | 2.89 | 0.49 | 2017-12 | -1.88 | 2.51 | 0.07 | -1.77 | 2.44 | 0.38 | 2019-12 | -1.31 | 3.86 | -0.07 | -5.14 | 5.76 | 0.05 |
| 2016-01 | -1.53 | 2.44 | 0.60 | -2.40 | 3.01 | 0.55 | 2018-01 | -2.23 | 3.96 | 0.05 | -2.88 | 3.66 | 0.46 | | | | | | | |
| 2016-02 | -2.28 | 3.49 | 0.35 | -3.65 | 4.78 | 0.06 | 2018-02 | -1.72 | 3.92 | -0.08 | -3.52 | 4.20 | 0.48 | | | | | | | |
| 2016-03 | -1.64 | 2.79 | 0.43 | -3.54 | 4.25 | 0.19 | 2018-03 | -1.80 | 2.88 | 0.05 | -2.95 | 3.38 | 0.16 | | | | | | | |
| 2016-04 | -2.15 | 3.22 | 0.57 | -3.26 | 4.20 | 0.40 | 2018-04 | -1.85 | 3.71 | 0.05 | -3.48 | 4.36 | 0.20 | | | | | | | |
| 2016-05 | -1.62 | 2.51 | 0.68 | -1.56 | 2.60 | 0.61 | 2018-05 | -1.55 | 2.74 | 0.22 | -3.14 | 3.91 | 0.01 | | | | | | | |
| 2016-06 | -2.26 | 3.23 | 0.28 | -2.96 | 3.80 | 0.28 | 2018-06 | -1.89 | 3.18 | 0.07 | -2.03 | 3.04 | 0.27 | | | | | | | |
| 2016-07 | -1.22 | 2.07 | 0.52 | -1.64 | 2.32 | 0.55 | 2018-07 | -1.38 | 2.28 | -0.06 | -2.59 | 3.19 | 0.01 | | | | | | | |
| 2016-08 | -1.42 | 2.74 | 0.31 | -3.24 | 3.90 | 0.60 | 2018-08 | -1.35 | 2.11 | 0.05 | -1.37 | 2.23 | 0.29 | | | | | | | |
| 2016-09 | -1.43 | 2.61 | 0.24 | -1.60 | 2.77 | 0.22 | 2018-09 | -1.69 | 2.79 | -0.16 | -2.44 | 3.08 | 0.15 | | | | | | | |
| 2016-10 | -2.36 | 2.82 | 0.48 | -2.22 | 2.79 | 0.48 | 2018-10 | -1.61 | 2.70 | 0.13 | -2.94 | 3.46 | 0.31 | | | | | | | |
| 2016-11 | -2.79 | 3.47 | 0.03 | -1.89 | 2.50 | 0.56 | 2018-11 | -1.97 | 3.35 | 0.15 | -0.85 | 3.17 | 0.30 | | | | | | | |
| 2016-12 | -2.22 | 3.26 | 0.30 | -1.15 | 2.96 | 0.38 | 2018-12 | -2.05 | 3.53 | -0.20 | -1.17 | 2.78 | 0.36 | | | | | | | |

**Table G2.** Analysis of the residual between CMAQ prior and posterior simulation and Gunn Point site for 2015–2019. Averaged bias (Bias), Root-mean-square error (RMSE) and Pearson's coefficient (R).

| | | | | | | | Gunn Point | | | | | | | | | | | | | | | | | | | | |
|---|---|---|---|---|---|---|---|---|---|---|---|---|---|---|---|---|---|---|---|---|---|---|---|---|---|---|
| months | Prior | | | Posterior | | | months | Prior | | | Posterior | | | months | Prior | | | Posterior | | |
| yyyy-mm | Bias | RMSE | R | Bias | RMSE | R | yyyy-mm | Bias | RMSE | R | Bias | RMSE | R | yyyy-mm | Bias | RMSE | R | Bias | RMSE | R |
| 2015-01 | -1.16 | 4.83 | 0.37 | -2.11 | 4.87 | 0.26 | 2017-01 | - | - | - | - | - | - | 2019-01 | -3.19 | 5.56 | -0.20 | -7.19 | 9.22 | -0.07 |
| 2015-02 | -2.88 | 4.73 | 0.41 | -3.55 | 4.07 | 0.47 | 2017-02 | - | - | - | - | - | - | 2019-02 | -5.04 | 5.80 | 0.24 | -6.25 | 7.12 | 0.28 |
| 2015-03 | -1.93 | 4.21 | -0.06 | -3.36 | 4.84 | -0.06 | 2017-03 | - | - | - | - | - | - | 2019-03 | -2.99 | 4.37 | 0.37 | -6.36 | 7.13 | 0.30 |
| 2015-04 | -1.07 | 2.92 | 0.33 | -2.74 | 3.44 | 0.28 | 2017-04 | - | - | - | - | - | - | 2019-04 | -0.27 | 4.03 | 0.27 | 2.12 | 5.48 | 0.29 |
| 2015-05 | -1.76 | 2.78 | 0.35 | -3.65 | 3.38 | 0.53 | 2017-05 | - | - | - | - | - | - | 2019-05 | -1.40 | 3.42 | 0.45 | 0.11 | 4.24 | 0.60 |
| 2015-06 | -0.96 | 1.68 | 0.29 | 1.90 | 4.07 | 0.31 | 2017-06 | - | - | - | - | - | - | 2019-06 | -0.23 | 1.75 | 0.45 | -4.04 | 3.70 | 0.57 |
| 2015-07 | -2.53 | 16.46 | 0.00 | -7.71 | 17.67 | 0.06 | 2017-07 | - | - | - | - | - | - | 2019-07 | 1.69 | 2.65 | 0.01 | -2.12 | 3.78 | 0.20 |
| 2015-08 | 1.70 | 2.43 | 0.41 | -2.88 | 4.21 | 0.25 | 2017-08 | - | - | - | - | - | - | 2019-08 | 1.17 | 4.47 | -0.03 | -1.75 | 4.59 | -0.12 |
| 2015-09 | 1.81 | 2.13 | 0.28 | -0.32 | 1.54 | 0.04 | 2017-09 | - | - | - | - | - | - | 2019-09 | 2.69 | 3.02 | 0.23 | 1.08 | 1.42 | 0.47 |
| 2015-10 | 2.19 | 2.44 | 0.15 | 3.24 | 3.84 | -0.03 | 2017-10 | - | - | - | - | - | - | 2019-10 | 2.31 | 3.25 | -0.30 | 3.51 | 4.28 | -0.01 |
| 2015-11 | -0.52 | 2.30 | -0.67 | 0.66 | 2.63 | -0.63 | 2017-11 | - | - | - | - | - | - | 2019-11 | -0.63 | 1.99 | -0.04 | 2.21 | 2.52 | 0.18 |
| 2015-12 | -2.69 | 3.34 | 0.38 | -4.03 | 4.45 | 0.36 | 2017-12 | - | - | - | - | - | - | 2019-12 | -1.36 | 2.11 | 0.15 | -0.42 | 3.96 | 0.03 |
| 2016-01 | -3.70 | 4.66 | 0.16 | -3.74 | 3.95 | 0.16 | 2018-01 | - | - | - | - | - | - | | | | | | | |
| 2016-02 | -3.40 | 4.71 | 0.33 | -5.19 | 6.22 | 0.36 | 2018-02 | - | - | - | - | - | - | | | | | | | |
| 2016-03 | -2.74 | 4.03 | -0.02 | -3.30 | 4.30 | 0.02 | 2018-03 | - | - | - | - | - | - | | | | | | | |
| 2016-04 | 1.21 | 3.14 | -0.38 | 1.92 | 3.12 | -0.03 | 2018-04 | - | - | - | - | - | - | | | | | | | |
| 2016-05 | -1.69 | 4.84 | -0.27 | -0.50 | 4.45 | 0.02 | 2018-05 | - | - | - | - | - | - | | | | | | | |
| 2016-06 | -2.91 | 3.12 | 0.68 | -4.28 | 4.02 | 0.79 | 2018-06 | - | - | - | - | - | - | | | | | | | |
| 2016-07 | - | - | - | - | - | - | 2018-07 | - | - | - | - | - | - | | | | | | | |
| 2016-08 | - | - | - | - | - | - | 2018-08 | 0.51 | 1.61 | 0.47 | -6.16 | 5.70 | -0.29 | | | | | | | |
| 2016-09 | - | - | - | - | - | - | 2018-09 | 0.83 | 1.37 | 0.15 | -1.95 | 1.65 | 0.01 | | | | | | | |
| 2016-10 | - | - | - | - | - | - | 2018-10 | 0.09 | 0.76 | 0.39 | 0.89 | 0.92 | 0.77 | | | | | | | |
| 2016-11 | - | - | - | - | - | - | 2018-11 | -4.24 | 4.63 | -0.11 | -4.08 | 5.45 | 0.05 | | | | | | | |
| 2016-12 | - | - | - | - | - | - | 2018-12 | -3.63 | 4.60 | 0.02 | -4.70 | 5.88 | 0.31 | | | | | | | |

**Table G3.** Analysis of the residual between CMAQ prior and posterior simulation and Iron bark site for 2015–2019. Averaged bias (Bias), Root-mean-square error (RMSE) and Pearson's coefficient (R).

| | | | | | | | Iron Bark | | | | | | | | | | | | | |
|---|---|---|---|---|---|---|---|---|---|---|---|---|---|---|---|---|---|---|---|---|
| months | Prior | | | Posterior | | | months | Prior | | | Posterior | | | months | Prior | | | Posterior | | |
| yyyy-mm | Bias | RMSE | R | Bias | RMSE | R | yyyy-mm | Bias | RMSE | R | Bias | RMSE | R | yyyy-mm | Bias | RMSE | R | Bias | RMSE | R |
| 2015-01 | -1.61 | 2.28 | 0.32 | 0.43 | 2.33 | 0.23 | 2017-01 | -1.02 | 1.09 | 0.77 | 0.82 | 0.90 | 0.01 | 2019-01 | - | - | - | - | - | - |
| 2015-02 | -1.07 | 1.30 | 0.44 | 0.71 | 1.14 | 0.06 | 2017-02 | - | - | - | - | - | - | 2019-02 | - | - | - | - | - | - |
| 2015-03 | -0.34 | 2.85 | 0.35 | -1.32 | 3.61 | 0.49 | 2017-03 | - | - | - | - | - | - | 2019-03 | - | - | - | - | - | - |
| 2015-04 | -1.11 | 2.13 | 0.50 | -1.48 | 2.52 | 0.00 | 2017-04 | - | - | - | - | - | - | 2019-04 | - | - | - | - | - | - |
| 2015-05 | -2.15 | 2.77 | 0.37 | -1.56 | 2.45 | 0.00 | 2017-05 | - | - | - | - | - | - | 2019-05 | - | - | - | - | - | - |
| 2015-06 | -2.12 | 2.63 | 0.46 | -2.29 | 3.26 | 0.83 | 2017-06 | - | - | - | - | - | - | 2019-06 | - | - | - | - | - | - |
| 2015-07 | -0.35 | 1.66 | 0.49 | -2.33 | 2.77 | 0.00 | 2017-07 | - | - | - | - | - | - | 2019-07 | - | - | - | - | - | - |
| 2015-08 | 1.44 | 2.55 | 0.26 | 0.92 | 2.84 | 0.87 | 2017-08 | - | - | - | - | - | - | 2019-08 | - | - | - | - | - | - |
| 2015-09 | 1.27 | 1.83 | 0.55 | 1.58 | 2.40 | 0.00 | 2017-09 | - | - | - | - | - | - | 2019-09 | - | - | - | - | - | - |
| 2015-10 | -0.81 | 2.04 | 0.28 | -0.90 | 2.04 | 0.00 | 2017-10 | - | - | - | - | - | - | 2019-10 | - | - | - | - | - | - |
| 2015-11 | -2.28 | 2.86 | 0.53 | 0.05 | 1.93 | 0.00 | 2017-11 | - | - | - | - | - | - | 2019-11 | - | - | - | - | - | - |
| 2015-12 | -1.50 | 2.77 | 0.50 | -3.33 | 4.34 | 0.00 | 2017-12 | - | - | - | - | - | - | 2019-12 | - | - | - | - | - | - |
| 2016-01 | -1.05 | 1.97 | 0.62 | -1.61 | 2.83 | 0.00 | 2018-01 | - | - | - | - | - | - | | | | | | | |
| 2016-02 | -1.60 | 2.99 | 0.24 | -1.04 | 3.49 | 0.04 | 2018-02 | -12.94 | 20.86 | 0.99 | -11.41 | 21.61 | 0.18 | | | | | | | |
| 2016-03 | -1.27 | 2.10 | 0.42 | -1.50 | 2.20 | 0.00 | 2018-03 | - | - | - | - | - | - | | | | | | | |
| 2016-04 | 0.37 | 1.58 | 0.53 | 0.91 | 2.21 | 0.00 | 2018-04 | -5.00 | 9.30 | 0.20 | -6.95 | 10.66 | 0.72 | | | | | | | |
| 2016-05 | -0.09 | 1.71 | 0.40 | -2.02 | 2.52 | 0.00 | 2018-05 | - | - | - | - | - | - | | | | | | | |
| 2016-06 | -2.12 | 2.87 | 0.16 | -4.22 | 4.99 | 0.64 | 2018-06 | - | - | - | - | - | - | | | | | | | |
| 2016-07 | -0.43 | 2.34 | 0.34 | -3.83 | 4.47 | 0.00 | 2018-07 | - | - | - | - | - | - | | | | | | | |
| 2016-08 | 1.10 | 2.44 | 0.21 | -2.25 | 3.59 | 0.02 | 2018-08 | - | - | - | - | - | - | | | | | | | |
| 2016-09 | 1.63 | 3.86 | 0.23 | 0.68 | 3.39 | 0.00 | 2018-09 | - | - | - | - | - | - | | | | | | | |
| 2016-10 | -0.04 | 1.53 | -0.51 | -0.26 | 2.00 | 0.00 | 2018-10 | - | - | - | - | - | - | | | | | | | |
| 2016-11 | -0.96 | 1.60 | 0.66 | 1.65 | 3.03 | 0.11 | 2018-11 | - | - | - | - | - | - | | | | | | | |
| 2016-12 | - | - | - | - | - | - | 2018-12 | - | - | - | - | - | - | | | | | | | |

**Table G4.** Analysis of the residual between CMAQ prior and posterior simulation and Burncluith site for 2015–2019. Averaged bias (Bias), Root-mean-square error (RMSE) and Pearson's coefficient (R).

| | | | | | | | Burncluith | | | | | | | | | | | | |
|---|---|---|---|---|---|---|---|---|---|---|---|---|---|---|---|---|---|---|---|
| months | Prior | | | Posterior | | | months | Prior | | | Posterior | | | months | Prior | | | Posterior | | |
| yyyy-mm | Bias | RMSE | R | Bias | RMSE | R | yyyy-mm | Bias | RMSE | R | Bias | RMSE | R | yyyy-mm | Bias | RMSE | R | Bias | RMSE | R |
| 2015-01 | - | - | - | - | - | - | 2017-01 | -0.44 | 2.74 | 0.34 | 0.21 | 2.68 | 0.28 | 2019-01 | - | - | - | - | - | - |
| 2015-02 | - | - | - | - | - | - | 2017-02 | 0.368 | 1.77 | 0.34 | 1.39 | 1.97 | 0.68 | 2019-02 | - | - | - | - | - | - |
| 2015-03 | - | - | - | - | - | - | 2017-03 | -1.06 | 2.24 | 0.21 | 0.58 | 2.61 | 0.12 | 2019-03 | - | - | - | - | - | - |
| 2015-04 | - | - | - | - | - | - | 2017-04 | -0.77 | 2.02 | 0.36 | 0.31 | 1.60 | 0.65 | 2019-04 | - | - | - | - | - | - |
| 2015-05 | - | - | - | - | - | - | 2017-05 | -1.77 | 2.55 | 0.33 | -1.28 | 2.02 | 0.56 | 2019-05 | - | - | - | - | - | - |
| 2015-06 | - | - | - | - | - | - | 2017-06 | -0.7 | 1.82 | 0.16 | -1.79 | 2.49 | 0.14 | 2019-06 | - | - | - | - | - | - |
| 2015-07 | 0.86 | 2.12 | 0.41 | -1.03 | 2.33 | 0.29 | 2017-07 | -0.75 | 2.46 | 0.23 | -2.58 | 3.60 | -0.07 | 2019-07 | - | - | - | - | - | - |
| 2015-08 | 2.20 | 3.06 | 0.38 | 1.57 | 3.10 | 0.09 | 2017-08 | 1.133 | 1.79 | 0.25 | 0.90 | 1.54 | 0.47 | 2019-08 | - | - | - | - | - | - |
| 2015-09 | 2.03 | 2.69 | 0.44 | 2.08 | 3.16 | 0.27 | 2017-09 | 1.226 | 1.72 | 0.50 | 0.83 | 1.07 | 0.84 | 2019-09 | - | - | - | - | - | - |
| 2015-10 | 0.21 | 1.84 | 0.26 | 0.01 | 1.87 | 0.20 | 2017-10 | -1.24 | 3.07 | 0.48 | 0.94 | 2.44 | 0.72 | 2019-10 | - | - | - | - | - | - |
| 2015-11 | -1.24 | 2.23 | 0.73 | 1.21 | 2.30 | 0.69 | 2017-11 | -0.37 | 1.98 | -0.10 | 2.80 | 3.28 | 0.20 | 2019-11 | - | - | - | - | - | - |
| 2015-12 | 0.33 | 2.52 | 0.45 | -1.32 | 3.23 | 0.21 | 2017-12 | -1 | 1.94 | 0.28 | 0.41 | 1.51 | 0.50 | 2019-12 | - | - | - | - | - | - |
| 2016-01 | 0.92 | 2.78 | 0.46 | 0.01 | 3.30 | -0.11 | 2018-01 | -0.16 | 1.99 | 0.60 | -0.93 | 2.17 | 0.63 | | | | | | | |
| 2016-02 | -0.35 | 2.88 | 0.14 | 0.16 | 3.50 | -0.22 | 2018-02 | -2.31 | 3.11 | 0.38 | -2.47 | 3.40 | 0.17 | | | | | | | |
| 2016-03 | -0.50 | 2.06 | 0.58 | -0.58 | 2.04 | 0.59 | 2018-03 | -0.27 | 2.77 | 0.37 | -0.23 | 3.08 | 0.09 | | | | | | | |
| 2016-04 | 1.78 | 2.90 | 0.30 | 2.13 | 3.20 | 0.27 | 2018-04 | -0.32 | 1.84 | 0.49 | -1.58 | 2.11 | 0.51 | | | | | | | |
| 2016-05 | 0.92 | 2.05 | 0.30 | -1.04 | 2.05 | 0.14 | 2018-05 | -0.46 | 3.01 | 0.04 | -1.47 | 3.35 | -0.08 | | | | | | | |
| 2016-06 | -1.46 | 2.59 | 0.12 | -3.57 | 4.68 | -0.13 | 2018-06 | - | - | - | - | - | - | | | | | | | |
| 2016-07 | -0.482 | 1.99 | 0.38 | -3.90 | 4.45 | 0.40 | 2018-07 | - | - | - | - | - | - | | | | | | | |
| 2016-08 | 0.5448 | 2.52 | 0.07 | -2.79 | 4.26 | -0.02 | 2018-08 | - | - | - | - | - | - | | | | | | | |
| 2016-09 | 1.1873 | 2.70 | 0.58 | 0.36 | 2.37 | 0.62 | 2018-09 | - | - | - | - | - | - | | | | | | | |
| 2016-10 | 0.8141 | 1.79 | 0.48 | 0.43 | 2.06 | 0.13 | 2018-10 | - | - | - | - | - | - | | | | | | | |
| 2016-11 | -0.308 | 1.96 | 0.55 | 1.63 | 3.75 | -0.08 | 2018-11 | - | - | - | - | - | - | | | | | | | |
| 2016-12 | -0.548 | 1.34 | 0.78 | 0.62 | 1.44 | 0.77 | 2018-12 | - | - | - | - | - | - | | | | | | | |

## Appendix H: Prior, posterior and GPP flux anomaly correlation analysis

**Table H1.** Pearson's R correlations between prior and posterior climatological seasonal fluxes, and GPP fluxes derived from CABLE BIOS3, MODIS and DIFFUSE model.

| Bioclimate regions | Climatological seasonal cycle (2015-2019) | | | | | | |
|---|---|---|---|---|---|---|---|
| | Prior and Posterior | Prior and CABLE BIOS3 GPP | Prior and DIFUSSE GPP | Prior and MODIS | Post and CABLE BIOS3 GPP | Post and DIFFUSE GPP | Post and MODIS |
| Tropics | 0.73 | -0.66 | -0.50 | -0.51 | -0.46 | -0.32 | -0.33 |
| Savanna | 0.67 | -0.58 | -0.40 | -0.40 | -0.40 | -0.25 | -0.32 |
| Warm Temperate | 0.57 | 0.19 | 0.35 | 0.28 | 0.26 | 0.42 | 0.30 |
| Cool Temperate | 0.76 | -0.28 | -0.17 | -0.27 | -0.11 | -0.03 | -0.15 |
| Meditarranean | 0.83 | -0.27 | -0.15 | -0.19 | -0.30 | -0.19 | -0.26 |
| Sparsely vegetated | 0.33 | -0.23 | 0.01 | 0.00 | -0.21 | -0.12 | -0.30 |

**Table H2.** Pearson's R correlations between prior and posterior flux anomalies, and GPP anomalies derived from CABLE BIOS3, MODIS and DIFFUSE model.

| Bioclimate regions | Anomalies correlations ( 2015-2019) | | | | | | |
|---|---|---|---|---|---|---|---|
| | Prior and Posterior | Prior and CABLE BIOS3 GPP | Prior and DIFUSSE GPP | Prior and MODIS | Post and CABLE BIOS3 GPP | Post and DIFFUSE GPP | Post and MODIS |
| Tropics | 0.59 | -0.63 | -0.20 | -0.38 | -0.34 | -0.02 | -0.15 |
| Savanna | 0.59 | -0.73 | -0.61 | -0.63 | -0.50 | -0.45 | -0.38 |
| Warm Temperate | 0.43 | -0.64 | -0.52 | -0.52 | -0.32 | -0.32 | -0.29 |
| Cool Temperate | 0.20 | -0.65 | -0.50 | -0.52 | 0.10 | -0.03 | -0.09 |
| Meditarranean | 0.35 | -0.71 | -0.50 | -0.45 | -0.18 | -0.16 | -0.02 |
| Sparsely vegetated | 0.49 | -0.46 | -0.31 | -0.34 | -0.61 | -0.49 | -0.48 |

*Data availability.*   The surface carbon gridded fluxes are available in Zenodo repository under the identifier https://doi.org/10.5281/zenodo.6649768.

605   *Code availability.*   The code of the inversion system is available at https://github.com/steven-thomas/py4dvar (Thomas, 2020).

*Author contributions.*   YV prepared all the input data required to run the inversion system and performed data analysis of the fluxes. YV was responsible for post-processing the TCCON and in-situ measurements, then developing the paper and figures. ST was the principal developer of the inversion system code. PJR and JDS also contributed to developing the inversion code, provided guidance for the manuscript's preparation and interpretation of the results. VH with help of JK ran CABLE BIOS3 and provided the biosphere fluxes required for the

610   inversion. ZML provided data from the ground-based *in-situ* measurements (Cape Grim, Ironbark, Burncluith and Gunn Point) and gave comments on the paper. DP reviewed and comments on the TCCON Lauder site. ND and DG reviewed the final manuscript.

*Competing interests.*   The authors declare that they have no conflict of interest.

*Acknowledgements.*   YV was funded by the National Agency for Research and Development (ANID) scholarship, Becas Chile (grant no. 72170210) and supported by the Education Infrastructure Fund of the Australian Government, and the Australian Research Council (ARC)

615   of the Centre of Excellence for Climate Extreme (CLEX, grant no. CE170100023). The authors would like to thank CSIRO and TCCON institutions for providing the dataset to validate the inversion. Darwin and Wollongong TCCON stations are supported by ARC grants DP160100598, LE0668470, DP140101552, DP110103118 and DP0879468, and Darwin through NASA grants NAG5-12247 and NNG05-GD07G. NMD is funded by an ARC Future Fellowship, FT180100327. This research was undertaken with the assistance of resources and services from the National Computational Infrastructure (NCI), which is supported by the Australian Government, and the resources of the

620   High-performance Computing Centre of the University of Melbourne, SPARTAN (Lafayette et al., 2016). We would like to thank all the OCO-2 MIP inverse modellers: Matthew Johnson, Frédéric Chevallier, Junjie Liu, Andrew Schuh, Andy Jacobson, Sean Crowell, David Baker, Sourish Basu and Feng Deng for contributing their OCO-2 (LNLG) global inversion products. We also acknowledge the efforts of FLUXCOM group and thank Ulrich Weber and Martin Jung for supplying the FLUXCOM dataset. We also recognise the effort of Randall Donohue from CSIRO for his assistance with DIFFUSE data and Vanessa Haverd for generating the CABLE BIOS3 dataset..

## 625 References

Annual climate statement, Bureau of Meteorology: Annual climate statement 2019, Bureau of Meteorology, http://www.bom.gov.au/climate/current/annual/aus/2019/, 2019.

Archibald, S. A., Kirton, A., van der Merwe, M. R., Scholes, R. J., Williams, C. A., and Hanan, N.: Drivers of inter-annual variability in Net Ecosystem Exchange in a semi-arid savanna ecosystem, South Africa, Biogeosciences, 6, 251–266, https://doi.org/10.5194/bg-6-251-2009, https://bg.copernicus.org/articles/6/251/2009/, 2009.

Basu, S., Guerlet, S., Butz, A., Houweling, S., Hasekamp, O., Aben, I., Krummel, P., Steele, P., Langenfelds, R., Torn, M., Biraud, S., Stephens, B., Andrews, A., and Worthy, D.: Global $CO_2$ fluxes estimated from GOSAT retrievals of total column $CO_2$, Atmospheric Chemistry and Physics, 13, 8695–8717, 2013.

Basu, S., Baker, D. F., Chevallier, F., Patra, P. K., Liu, J., and Miller, J. B.: The impact of transport model differences on $CO_2$ surface flux estimates from OCO-2 retrievals of column average $CO_2$, Atmospheric Chemistry and Physics, 18, 7189–7215, https://doi.org/10.5194/acp-18-7189-2018, 2018.

Byrd, R., Lu, P., Nocedal, J., and Zhu, C.: A Limited Memory Algorithm for Bound Constrained Optimization, SIAM Journal on Scientific Computing, 16, 1190–1208, https://doi.org/10.1137/0916069, 1995.

Chevallier, F.: personal communication, 2019.

Chevallier, F., Ciais, P., Conway, T. J., Aalto, T., Anderson, B. E., Bousquet, P., Brunke, E. G., Ciattaglia, L., Esaki, Y., Fröhlich, M., Gomez, A., Gomez-Pelaez, A. J., Haszpra, L., Krummel, P. B., Langenfelds, R. L., Leuenberger, M., Machida, T., Maignan, F., Matsueda, H., Morguí, J. A., Mukai, H., Nakazawa, T., Peylin, P., Ramonet, M., Rivier, L., Sawa, Y., Schmidt, M., Steele, L. P., Vay, S. A., Vermeulen, A. T., Wofsy, S., and Worthy, D.: $CO_2$ surface fluxes at grid point scale estimated from a global 21 year reanalysis of atmospheric measurements, Journal of Geophysical Research, 115, D21 307, https://doi.org/10.1029/2010JD013887, 2010.

Churkina, G. and Running, S. W.: Contrasting climatic controls on the estimated productivity of global terrestrial biomes, Ecosystems, 1, 206–215, 1998.

Connor, B. J., Boesch, H., Toon, G., Sen, B., Miller, C., and Crisp, D.: Orbiting Carbon Observatory: Inverse method and prospective error analysis, Journal of Geophysical Research Atmospheres, 113, 1–14, https://doi.org/10.1029/2006JD008336, 2008.

Crippa, M., Solazzo, E., Huang, G., Guizzardi, D., Koffi, E., Muntean, M., Schieberle, C., Friedrich, R., and Janssens-Maenhout, G.: High resolution temporal profiles in the Emissions Database for Global Atmospheric Research, Scientific Data, 7, 121, https://doi.org/10.1038/s41597-020-0462-2, 2020.

Crowell, S., Baker, D., Schuh, A., Basu, S., Jacobson, A. R., Chevallier, F., Liu, J., Deng, F., Feng, L., McKain, K., Chatterjee, A., Miller, J. B., Stephens, B. B., Eldering, A., Crisp, D., Schimel, D., Nassar, R., O'Dell, C. W., Oda, T., Sweeney, C., Palmer, P. I., and Jones, D. B. A.: The 2015–2016 carbon cycle as seen from OCO-2 and the global in situ network, Atmospheric Chemistry and Physics, 19, 9797–9831, https://doi.org/10.5194/acp-19-9797-2019, 2019.

Dee, D. P., Uppala, S. M., Simmons, A. J., Berrisford, P., Poli, P., Kobayashi, S., Andrae, U., Balmaseda, M. A., Balsamo, G., Bauer, P., Bechtold, P., Beljaars, A. C. M., van de Berg, L., Bidlot, J., Bormann, N., Delsol, C., Dragani, R., Fuentes, M., Geer, A. J., Haimberger, L., Healy, S. B., Hersbach, H., Hólm, E. V., Isaksen, L., Kållberg, P., Köhler, M., Matricardi, M., McNally, A. P., Monge-Sanz, B. M., Morcrette, J.-J., Park, B.-K., Peubey, C., de Rosnay, P., Tavolato, C., Thépaut, J.-N., and Vitart, F.: The ERA-Interim reanalysis: configuration and performance of the data assimilation system, Quarterly Journal of the Royal Meteorological Society, 137, 553–597, https://doi.org/10.1002/qj.828, 2011.

Detmers, R. G., Hasekamp, O., Aben, I., Houweling, S., van Leeuwen, T. T., Butz, A., Landgraf, J., Köhler, P., Guanter, L., and Poulter, B.: Anomalous carbon uptake in Australia as seen by GOSAT, Geophysical Research Letters, 42, 8177–8184, https://doi.org/10.1002/2015GL065161, 2015.

665 Deutscher, N. M., Griffith, D. W. T., Bryant, G. W., Wennberg, P. O., Toon, G. C., Washenfelder, R. A., Keppel-Aleks, G., Wunch, D., Yavin, Y., Allen, N. T., Blavier, J.-F., Jiménez, R., Daube, B. C., Bright, A. V., Matross, D. M., Wofsy, S. C., and Park, S.: Total column $CO_2$ measurements at Darwin, Australia − site description and calibration against in situ aircraft profiles, Atmospheric Measurement Techniques, 3, 947–958, https://doi.org/10.5194/amt-3-947-2010, 2010.

Deutscher, N. M., Sherlock, V., Mikaloff Fletcher, S. E., Griffith, D. W. T., Notholt, J., Macatangay, R., Connor, B. J., Robinson, J., Shiona,
670 H., Velazco, V. A., Wang, Y., Wennberg, P. O., and Wunch, D.: Drivers of column-average $CO_2$ variability at Southern Hemispheric Total Carbon Column Observing Network sites, Atmospheric Chemistry and Physics, 14, 9883–9901, https://doi.org/10.5194/acp-14-9883-2014, 2014.

Didan, K.: MOD13C1 MODIS/Terra Vegetation Indices 16-Day L3 Global 0.05 Deg CMG V006 [Data set], https://doi.org/10.5067/MODIS/MOD13C1.006, last accessed 2019-06-07, 2014.

675 Donohue, R. J., Hume, I. H., Roderick, M. L., McVicar, T. R., Beringer, J., Hutley, L. B., Gallant, J. C., Austin, J. M., van Gorsel, E., Cleverly, J. R., Meyer, W. S., and Arndt, S. K.: Evaluation of the remote-sensing-based DIFFUSE model for estimating photosynthesis of vegetation, Remote Sens. Environ., 155, 349–365, https://doi.org/https://doi.org/10.1016/j.rse.2014.09.007, 2014.

Eldering, A. .: OCO-2 Lite product V9r, https://oco2.gesdisc.eosdis.nasa.gov/data/s4pa/OCO2_DATA/OCO2_L2_Lite_FP.9r/2015, [accessed September 2018], 2018.

680 Eldering, A., Taylor, T. E., O'Dell, C. W., and Pavlick, R.: The OCO-3 mission: measurement objectives and expected performance based on 1 year of simulated data, Atmospheric Measurement Techniques, 12, 2341–2370, https://doi.org/10.5194/amt-12-2341-2019, 2019.

Etheridge, D., Loh, Z., Schroder, I., Berko, H., Kuske, T., Allison, C., Gregory, R., Spencer, D., Langenfelds, R., Zegelin, S., Hibberd, M., and Feitz, A.: Metadata report: Arcturus atmospheric greenhouse gas monitoring, Tech. rep., Geoscience Australia, Canberra, https://doi.org/http://dx.doi.org/10.11636/Record.2014.037, 2014.

685 Etheridge, D. M., Day, S., M. F. Hibberd, A. L., Spencer, D. A., Loh, Z. M., Zegelin, S., Krummel, P. B., van Gorsel, E., Thornton, D. P., Gregory, R. L., Ong, C., and Barrett, D.: Characterisation of Regional Fluxes of Methane in the Surat Basin, Queensland - Milestone 3.1 GISERA Greenhouse Gas Research – Phase 3, Tech. rep., CSIRO, Australia, 2016.

FIRM: The Fire Information for Resource Management System (FIRMS), https://firms.modaps.eosdis.nasa.gov/map/, last accessed 2020-07-18, 2020.

690 Friedlingstein, P., O'Sullivan, M., Jones, M. W., Andrew, R. M., Hauck, J., Olsen, A., Peters, G. P., Peters, W., Pongratz, J., Sitch, S., Le Quéré, C., Canadell, J. G., Ciais, P., Jackson, R. B., Alin, S., Aragão, L. E. O. C., Arneth, A., Arora, V., Bates, N. R., Becker, M., Benoit-Cattin, A., Bittig, H. C., Bopp, L., Bultan, S., Chandra, N., Chevallier, F., Chini, L. P., Evans, W., Florentie, L., Forster, P. M., Gasser, T., Gehlen, M., Gilfillan, D., Gkritzalis, T., Gregor, L., Gruber, N., Harris, I., Hartung, K., Haverd, V., Houghton, R. A., Ilyina, T., Jain, A. K., Joetzjer, E., Kadono, K., Kato, E., Kitidis, V., Korsbakken, J. I., Landschützer, P., Lefèvre, N., Lenton, A., Lienert, S.,
695 Liu, Z., Lombardozzi, D., Marland, G., Metzl, N., Munro, D. R., Nabel, J. E. M. S., Nakaoka, S.-I., Niwa, Y., O'Brien, K., Ono, T., Palmer, P. I., Pierrot, D., Poulter, B., Resplandy, L., Robertson, E., Rödenbeck, C., Schwinger, J., Séférian, R., Skjelvan, I., Smith, A. J. P., Sutton, A. J., Tanhua, T., Tans, P. P., Tian, H., Tilbrook, B., van der Werf, G., Vuichard, N., Walker, A. P., Wanninkhof, R., Watson, A. J., Willis, D., Wiltshire, A. J., Yuan, W., Yue, X., and Zaehle, S.: Global Carbon Budget 2020, Earth System Science Data, 12, 3269–3340, https://doi.org/10.5194/essd-12-3269-2020, 2020.

700 Gerbig, C., Körner, S., and Lin, J. C.: Vertical mixing in atmospheric tracer transport models: error characterization and propagation, Atmospheric Chemistry and Physics, 8, 591–602, https://doi.org/10.5194/acp-8-591-2008, https://acp.copernicus.org/articles/8/591/2008/, 2008.

Griffith, D., Deutscher, N., Velazco, V., Wennberg, P., Yavin, Y., Aleks, G. K., Washenfelder, R., Toon, G., Blavier, J., Murphy, C., et al.: TCCON data from Darwin, Australia, Release GGG2014R0, TCCON data archive, hosted by Caltech-DATA, California Institute of
705 Technology, Pasadena, CA, USA, https://doi.org/http://doi.org/10.14291/tccon.ggg2014.darwin01.R0/1149290, 2017a.

Griffith, D., Velazco, V., Deutscher, N., Murphy, C., Jones, N., Wilson, S., Macatangay, R., Kettlewell, G., Buchholz, R., and Riggenbach, M.: TCCON data from Wollongong, Australia, Release GGG2014R0. TCCON data archive, hosted by CaltechDATA, California Institute of Technology, Pasadena, CA, U.S.A, https://doi.org/https://doi.org/10.14291/tccon.ggg2014.wollongong01.R0/1149291, 2017b.

Hakami, A., Henze, D. K., Seinfeld, J. H., Singh, K., Sandu, A., Kim, S., Byun, and Li, Q.: The Adjoint of CMAQ, Environmental Science
710 & Technology, 41, 7807–7817, https://doi.org/10.1021/es070944p, pMID: 18075092, 2007.

Haverd, V., Raupach, M. R., Briggs, P. R., Canadell., J. G., Davis, S. J., Law, R. M., Meyer, C. P., Peters, G. P., Pickett-Heaps, C., and Sherman, B.: The Australian terrestrial carbon budget, Biogeosciences, 10, 851–869, https://doi.org/10.5194/bg-10-851-2013, 2013a.

Haverd, V., Smith, B., Cook, G. D., Briggs, P. R., Nieradzik, L., Roxburgh, S. H., Liedloff, A., Meyer, C. P., and Canadell, J. G.: A stand-alone tree demography and landscape structure module for Earth system models, Geophysical Research Letters, 40, 5234–5239,
715 https://doi.org/https://doi.org/10.1002/grl.50972, 2013b.

Haverd, V., Smith, B., and Trudinger, C.: Process contributions of Australian ecosystems to interannual variations in the carbon cycle, Environmental Research Letters, 11, 054 013, https://doi.org/10.1088/1748-9326/11/5/054013, 2016.

Haverd, V., Smith, B., Nieradzik, L., Briggs, P. R., Woodgate, W., Trudinger, C. M., Canadell, J. G., and Cuntz, M.: A new version of the CABLE land surface model (Subversion revision r4601) incorporating land use and land cover change, woody vegetation demography,
720 and a novel optimisation-based approach to plant coordination of photosynthesis, Geoscientific Model Development, 11, 2995–3026, https://doi.org/10.5194/gmd-11-2995-2018, 2018.

Jones, D. A., Wang, W., and Fawcett, R.: High-quality spatial climate data-sets for Australia, Australian Meteorological and Oceanographic Journal, 58, 233–248, 2009.

Jung, M., Schwalm, C., Migliavacca, M., Walther, S., Camps-Valls, G., Koirala, S., Anthoni, P., Besnard, S., Bodesheim, P., Carvalhais, N.,
725 Chevallier, F., Gans, F., Goll, D. S., Haverd, V., Köhler, P., Ichii, K., Jain, A. K., Liu, J., Lombardozzi, D., Nabel, J. E. M. S., Nelson, J. A., O'Sullivan, M., Pallandt, M., Papale, D., Peters, W., Pongratz, J., Rödenbeck, C., Sitch, S., Tramontana, G., Walker, A., Weber, U., and Reichstein, M.: Scaling carbon fluxes from eddy covariance sites to globe: synthesis and evaluation of the FLUXCOM approach, Biogeosciences, 17, 1343–1365, https://doi.org/10.5194/bg-17-1343-2020, 2020.

Kawasaki, M., Yoshioka, H., Jones, N. B., Macatangay, R., Griffith, D. W. T., Kawakami, S., Ohyama, H., Tanaka, T., Morino, I., Uchino,
730 O., and Ibuki, T.: Usability of optical spectrum analyzer in measuring atmospheric $CO_2$ and $CH_4$ column densities: inspection with FTS and aircraft profiles in situ, Atmospheric Measurement Techniques, 5, 2593–2600, https://doi.org/10.5194/amt-5-2593-2012, 2012.

Kiel, M., O'Dell, C. W., Fisher, B., Eldering, A., Nassar, R., MacDonald, C. G., and Wennberg, P. O.: How bias correction goes wrong: measurement of XCO2 affected by erroneous surface pressure estimates., Atmospheric Measurement Techniques, 12, 2019.

Lafayette, L., Sauter, G., Vu, L., and Meade, B.: "Spartan Performance and Flexibility: An HPC-Cloud Chimera", OpenStack Summit,
735 Barcelona, October, https://doi.org/https://doi.org/10.4225/49/58ead90dceaaa, 2016.

Lauvaux, T., Schuh, A. E., Uliasz, M., Richardson, S., Miles, N., Andrews, A. E., Sweeney, C., Diaz, L. I., Martins, D., Shepson, P. B., and Davis, K. J.: Constraining the $CO_2$ budget of the corn belt: exploring uncertainties from the assumptions in a mesoscale inverse system, Atmospheric Chemistry and Physics, 12, 337–354, https://doi.org/10.5194/acp-12-337-2012, 2012.

Law, R. M., Peters, W., Rödenbeck, C., Aulagnier, C., Baker, I., Bergmann, D. J., Bousquet, P., Brandt, J., Bruhwiler, L., Cameron-Smith, P. J., Christensen, J. H., Delage, F., Denning, A. S., Fan, S., Geels, C., Houweling, S., Imasu, R., Karstens, U., Kawa, S. R., Kleist, J., Krol, M. C., Lin, S.-J., Lokupitiya, R., Maki, T., Maksyutov, S., Niwa, Y., Onishi, R., Parazoo, N., Patra, P. K., Pieterse, G., Rivier, L., Satoh, M., Serrar, S., Taguchi, S., Takigawa, M., Vautard, R., Vermeulen, A. T., and Zhu, Z.: TransCom model simulations of hourly atmospheric $CO_2$ : Experimental overview and diurnal cycle results for 2002, Global Biogeochemical Cycles, 22, https://doi.org/10.1029/2007GB003050, 2008.

Ma, X., Huete, A., Cleverly, J., Eamus, D., Chevallier, F., Joiner, J., Poulter, B., Zhang, Y., Guanter, L., Meyer, W., Xie, Z., and Ponce-Campos, G.: Drought rapidly diminishes the large net $CO_2$ uptake in 2011 over semi-arid Australia, Scientific Reports, 6, 37 747, https://doi.org/10.1038/srep37747, 2016.

Merbold, L., Ardö, J., Arneth, A., Scholes, R. J., Nouvellon, Y., de Grandcourt, A., Archibald, S., Bonnefond, J. M., Boulain, N., Brueggemann, N., Bruemmer, C., Cappelaere, B., Ceschia, E., El-Khidir, H. A. M., El-Tahir, B. A., Falk, U., Lloyd, J., Kergoat, L., Le Dantec, V., Mougin, E., Muchinda, M., Mukelabai, M. M., Ramier, D., Roupsard, O., Timouk, F., Veenendaal, E. M., and Kutsch, W. L.: Precipitation as driver of carbon fluxes in 11 African ecosystems, Biogeosciences, 6, 1027–1041, https://doi.org/10.5194/bg-6-1027-2009, https://bg.copernicus.org/articles/6/1027/2009/, 2009.

Miller, S. M. and Michalak, A. M.: The impact of improved satellite retrievals on estimates of biospheric carbon balance, Atmospheric Chemistry and Physics, 20, 323–331, https://doi.org/10.5194/acp-20-323-2020, 2020.

Monteil, G., Broquet, G., Scholze, M., Lang, M., Karstens, U., Gerbig, C., Koch, F.-T., Smith, N. E., Thompson, R. L., Luijkx, I. T., White, E., Meesters, A., Ciais, P., Ganesan, A. L., Manning, A., Mischurow, M., Peters, W., Peylin, P., Tarniewicz, J., Rigby, M., Rödenbeck, C., Vermeulen, A., and Walton, E. M.: The regional European atmospheric transport inversion comparison, EUROCOM: first results on European-wide terrestrial carbon fluxes for the period 2006–2015, Atmospheric Chemistry and Physics, 20, 12 063–12 091, https://doi.org/10.5194/acp-20-12063-2020, 2020.

Nassar, R., Napier-Linton, L., Gurney, K. R., Andres, R. J., Oda, T., Vogel, F. R., and Deng, F.: Improving the temporal and spatial distribution of $CO_2$ emissions from global fossil fuel emission data sets, Journal of Geophysical Research: Atmospheres, 118, 917–933, https://doi.org/10.1029/2012JD018196, 2013.

OCO-2 Data Quality Statement: Orbiting Carbon Observatory-2 (OCO-2) Data Quality Statement: Level 2 Forward Processing Data Release 10 (V10), https://docserver.gesdisc.eosdis.nasa.gov/public/project/OCO/OCO2_DQ_Statement.V10.pdf, 2020.

Oda, T., Maksyutov, S., and Andres, R. J.: The Open-source Data Inventory for Anthropogenic $CO_2$, version 2016 (ODIAC2016): a global monthly fossil fuel $CO_2$ gridded emissions data product for tracer transport simulations and surface flux inversions, Earth System Science Data, 10, 87–107, https://doi.org/10.5194/essd-10-87-2018, 2018.

O'Dell, C. W., Eldering, A., Wennberg, P. O., Crisp, D., Gunson, M. R., Fisher, B., Frankenberg, C., Kiel, M., Lindqvist, H., Mandrake, L., Merrelli, A., Natraj, V., Nelson, R. R., Osterman, G. B., Payne, V. H., Taylor, T. E., Wunch, D., Drouin, B. J., Oyafuso, F., Chang, A., McDuffie, J., Smyth, M., Baker, D. F., Basu, S., Chevallier, F., Crowell, S. M. R., Feng, L., Palmer, P. I., Dubey, M., García, O. E., Griffith, D. W. T., Hase, F., Iraci, L. T., Kivi, R., Morino, I., Notholt, J., Ohyama, H., Petri, C., Roehl, C. M., Sha, M. K., Strong, K., Sussmann, R., Te, Y., Uchino, O., and Velazco, V. A.: Improved retrievals of carbon dioxide from Orbiting Carbon Observatory-2 with the version 8 ACOS algorithm, Atmospheric Measurement Techniques, 11, 6539–6576, https://doi.org/10.5194/amt-11-6539-2018, 2018.

Peiro, H., Crowell, S., Schuh, A., Baker, D. F., O'Dell, C., Jacobson, A. R., Chevallier, F., Liu, J., Eldering, A., Crisp, D., Deng, F., Weir, B.,
Basu, S., Johnson, M. S., Philip, S., and Baker, I.: Four years of global carbon cycle observed from OCO-2 version 9 and *in situ* data, and
comparison to OCO-2 v7, Atmospheric Chemistry and Physics Discussions, 2021, 1–50, https://doi.org/10.5194/acp-2021-373, 2021.

Peylin, P., Law, R. M., Gurney, K. R., Chevallier, F., Jacobson, A. R., Maki, T., Niwa, Y., Patra, P. K., Peters, W., Rayner, P. J., Rödenbeck, C.,
Van Der Laan-Luijkx, I. T., and Zhang, X.: Global atmospheric carbon budget: Results from an ensemble of atmospheric $CO_2$ inversions,
Biogeosciences, 10, 6699–6720, https://doi.org/10.5194/bg-10-6699-2013, 2013.

Pollard, D. F., Sherlock, V., Robinson, J., Deutscher, N. M., Connor, B., and Shiona, H.: The Total Carbon Column Observing Network site
description for Lauder, New Zealand, Earth Syst. Sci. Data, 9, 977–992, https://doi.org/10.5194/essd-9-977-2017, 2017.

Pollard, D. F., Robinson, J., and Shiona, H.: TCCON data from Lauder, New Zealand, 125HR, Release
GGG2014R0.TCCON data archive, hosted by CaltechDATA, California Institute of Technology, Pasadena, CA, U.S.A.,
https://doi.org/https://doi.org/10.14291/tccon.ggg2014.lauder03.R0, 2019.

Poulter, B., Frank, D., Ciais, P., Myneni, R. B., Andela, N., Bi, J., Broquet, G., Canadell, J. G., Chevallier, F., Liu, Y. Y., Running, S. W.,
Sitch, S., and van der Werf, G. R.: Contribution of semi-arid ecosystems to interannual variability of the global carbon cycle, Nature, 509,
600–603, https://doi.org/10.1038/nature13376, 2014.

Rayner, P. J., Michalak, A. M., and Chevallier, F.: Fundamentals of data assimilation applied to biogeochemistry, Atmospheric Chemistry
and Physics, 19, 13 911–13 932, https://doi.org/10.5194/acp-19-13911-2019, 2019.

Running, S., Mu, Q., and Zhao, M.: MOD17A2H MODIS/terra gross primary productivity 8-day L4 global 500m SIN grid V006, https:
//lpdaac.usgs.gov/products/mod17a2hv006,lastaccessed2019-09-10, 2015.

Schuh, A. E., Jacobson, A. R., Basu, S., Weir, B., Baker, D., Bowman, K., Chevallier, F., Crowell, S., Davis, K. J., Deng, F., Denning,
S., Feng, L., Jones, D., Liu, J., and Palmer, P. I.: Quantifying the Impact of Atmospheric Transport Uncertainty on $CO_2$ Surface Flux
Estimates, Global Biogeochemical Cycles, 33, 484–500, https://doi.org/https://doi.org/10.1029/2018GB006086, 2019.

Sherlock, V., Connor, B., Robinson, J., Shiona, H., Smale, D., and Pollard, D.: TCCON data from Lauder, New Zealand, 125HR,
Release GGG2014R0. TCCON data archive, hosted by CaltechDATA, California Institute of Technology, Pasadena, CA, U.S.A.,
https://doi.org/https://doi.org/10.14291/tccon.ggg2014.lauder02.R0/1149298, 2017.

Sitch, S., Friedlingstein, P., Gruber, N., Jones, S. D., Murray-Tortarolo, G., Ahlström, A., Doney, S. C., Graven, H., Heinze, C., Hunting-
ford, C., Levis, S., Levy, P. E., Lomas, M., Poulter, B., Viovy, N., Zaehle, S., Zeng, N., Arneth, A., Bonan, G., Bopp, L., Canadell,
J. G., Chevallier, F., Ciais, P., Ellis, R., Gloor, M., Peylin, P., Piao, S., Le Quéré, C., Smith, B., Zhu, Z., and Myneni, R.: Trends and
drivers of regional sources and sinks of carbon dioxide over the past two decades, Biogeosciences Discussions, 10, 20 113–20 177,
https://doi.org/10.5194/bgd-10-20113-2013, 2013.

Sitch, S., Friedlingstein, P., Gruber, N., Jones, S. D., Murray-Tortarolo, G., Ahlström, A., Doney, S. C., Graven, H., Heinze, C., Huntingford,
C., Levis, S., Levy, P. E., Lomas, M., Poulter, B., Viovy, N., Zaehle, S., Zeng, N., Arneth, A., Bonan, G., Bopp, L., Canadell, J. G.,
Chevallier, F., Ciais, P., Ellis, R., Gloor, M., Peylin, P., Piao, S. L., Le Quéré, C., Smith, B., Zhu, Z., and Myneni, R.: Recent trends and
drivers of regional sources and sinks of carbon dioxide, Biogeosciences, 12, 653–679, https://doi.org/10.5194/bg-12-653-2015, 2015.

Skamarock, W., Klemp, J., Dudhi, J., Gill, D., Barker, D., Duda, M., Huang, X.-Y., Wang, W., and Powers, J.: A Description of the Advanced
Research WRF Version 3, Technical Report, p. 113, https://doi.org/10.5065/D6DZ069T, 2008.

Tarantola, A.: Inverse Problem Theory: methods for data fitting and model parameter estimation, Elsevier, 1987.

Taylor, T. E., O'Dell, C. W., Frankenberg, C., Partain, P. T., Cronk, H. Q., Savtchenko, A., Nelson, R. R., Rosenthal, E. J., Chang, A. Y.,
Fisher, B., Osterman, G. B., Pollock, R. H., Crisp, D., Eldering, A., and Gunson, M. R.: Orbiting Carbon Observatory-2 (OCO-2)

cloud screening algorithms: validation against collocated MODIS and CALIOP data, Atmospheric Measurement Techniques, 9, 973–989, https://doi.org/10.5194/amt-9-973-2016, 2016.

Thomas, S.: Python 4-dimensional variational data assimilation tool, https://github.com/steven-thomas/py4dvar, Apalache Licence 2.0.
815      (Copyright 2016 University of Melbourne), last accessed: 12-07-2020, 2020.

Tramontana, G., Jung, M., Schwalm, C. R., Ichii, K., Camps-Valls, G., Ráduly, B., Reichstein, M., Arain, M. A., Cescatti, A., Kiely, G., Merbold, L., Serrano-Ortiz, P., Sickert, S., Wolf, S., and Papale, D.: Predicting carbon dioxide and energy fluxes across global FLUXNET sites with regression algorithms, Biogeosciences, 13, 4291–4313, https://doi.org/10.5194/bg-13-4291-2016, https://bg.copernicus.org/articles/13/4291/2016/, 2016.

820 Trudinger, C. M., Haverd, V., Briggs, P. R., and Canadell, J. G.: Interannual variability in Australia's terrestrial carbon cycle constrained by multiple observation types, Biogeosciences, 13, 6363–6383, https://doi.org/10.5194/bg-13-6363-2016, 2016.

Villalobos, Y., Rayner, P., Thomas, S., and Silver, J.: The potential of Orbiting Carbon Observatory-2 data to reduce the uncertainties in $CO_2$ surface fluxes over Australia using a variational assimilation scheme, Atmospheric Chemistry and Physics, 20, 8473–8500, https://doi.org/10.5194/acp-20-8473-2020, 2020.

825 Villalobos, Y., Rayner, P. J., Silver, J. D., Thomas, S., Haverd, V., Knauer, J., Loh, Z. M., Deutscher, N. M., Griffith, D. W. T., and Pollard, D. F.: Was Australia a sink or source of $CO_2$ in 2015? Data assimilation using OCO-2 satellite measurements, Atmospheric Chemistry and Physics, 21, 17 453–17 494, https://doi.org/10.5194/acp-21-17453-2021, 2021.

Wang, Y. P., Law, R. M., and Pak, B.: A global model of carbon, nitrogen and phosphorus cycles for the terrestrial biosphere, Biogeosciences, 7, 2261–2282, https://doi.org/10.5194/bg-7-2261-2010, 2010.

830 Williams, C. A., Hanan, N. P., Baker, I., Collatz, G. J., Berry, J., and Denning, A. S.: Interannual variability of photosynthesis across Africa and its attribution, Journal of Geophysical Research: Biogeosciences, 113, 2008.

Wunch, D., Toon, G. C., Blavier, J.-F. L., Washenfelder, R. A., Notholt, J., Connor, B. J., Griffith, D. W. T., Sherlock, V., and Wennberg, P. O.: The Total Carbon Column Observing Network, Philosophical Transactions of the Royal Society A: Mathematical, Physical and Engineering Sciences, 369, 2087–2112, https://doi.org/10.1098/rsta.2010.0240, 2011.

835 Zhao, C. L. and Tans, P. P.: Estimating uncertainty of the WMO mole fraction scale for carbon dioxide in air, Journal of Geophysical Research: Atmospheres, 111, https://doi.org/https://doi.org/10.1029/2005JD006003, 2006.